Tectonics®

RESEARCH ARTICLE
10.1029/2021TC007097

Key Points:

- A magma-rich and a magma-starved shear zone show the different ways in which upper crustal deformation connects to deep-crustal deformation
- The primary driver of strain localization at all depths was the reactivation of steep, inherited crustal boundaries
- Magmatism governed how a large shear zone initiated, grew, and interacted with crustal boundaries, resulting in architectural complexity

Supporting Information:

Supporting Information may be found in the online version of this article.

Correspondence to:

K. A. Klepeis,
kklepeis@uvm.edu

Citation:

Klepeis, K. A., Schwartz, J. J., Miranda, E., Lindquist, P., Jongens, R., Turnbull, R., & Stowell, H. (2022). The initiation and growth of transpressional shear zones through continental arc lithosphere, southwest New Zealand. *Tectonics*, *41*, e2021TC007097. https://doi.org/10.1029/2021TC007097

Received 2 OCT 2021
Accepted 27 MAY 2022

Author Contributions:

Conceptualization: Keith A. Klepeis, Joshua J. Schwartz, Elena Miranda, Richard Jongens, Rose Turnbull
Data curation: Keith A. Klepeis
Formal analysis: Keith A. Klepeis, Joshua J. Schwartz, Elena Miranda, Peter Lindquist
Funding acquisition: Keith A. Klepeis, Elena Miranda
Investigation: Keith A. Klepeis, Joshua J. Schwartz, Elena Miranda, Peter Lindquist, Richard Jongens, Rose Turnbull, Harold Stowell

The Initiation and Growth of Transpressional Shear Zones Through Continental Arc Lithosphere, Southwest New Zealand

Keith A. Klepeis[1], Joshua J. Schwartz[2], Elena Miranda[2], Peter Lindquist[1,3], Richard Jongens[4], Rose Turnbull[5], and Harold Stowell[6]

[1]Department of Geology, University of Vermont, Burlington, VT, USA, [2]Department of Geology, California State University Northridge, Northridge, CA, USA, [3]Now at Department of Earth and Space Sciences, University of Washington, Seattle, WA, USA, [4]Anatoki Geoscience Ltd, Dunedin, New Zealand, [5]Dunedin Research Centre, GNS Science, Dunedin, New Zealand, [6]Department of Geological Sciences, University of Alabama, Tuscaloosa, AL, USA

Abstract Structural analyses combined with new U-Pb zircon and titanite geochronology show how two Early Cretaceous transpressional shear zones initiated and grew through a nearly complete section of continental arc crust during oblique convergence. Both shear zones reactivated Carboniferous faults that penetrated the upper mantle below Zealandia's Median Batholith but show opposite growth patterns and dissimilar relationships with respect to arc magmatism. The Grebe-Indecision Creek shear zone was magma-starved and first reactivated at ~136 Ma as an oblique-reverse fault, along which an outboard batholith partially subducted beneath Gondwana. This system nucleated at or above ~20 km depth and propagated downward at 2–3 mm yr^{-1}, accumulating at least 35–45 km of horizontal (arc-normal) shortening by ~124 Ma. In contrast, the magma-rich George Sound shear zone first reactivated in the lower crust (~55 km depth) at ~124 Ma and grew upward at ~3 mm yr^{-1}, reaching the upper crust by ~110 Ma. In this latter system, magmatism influenced shear zone architecture and drove its growth while subduction and oblique convergence ended. As magma entered the roots of the system and began to solidify, deformation was driven out of the lower crust and into the middle crust where the system widened by a factor of three when fold-thrust belts formed on either side of a steep, central transpressional shear zone. This study illustrates how the reactivation of structural weaknesses localizes deformation at all depths in the lithosphere and shows how magma-deformation feedbacks influence shear zone connectivity and built a batholith from the bottom up.

Plain Language Summary Faults and ductile shear zones are regions of concentrated deformation, across which significant displacements have accumulated. These structures exhibit a broad range of behaviors and styles, and they regulate the transfer of mass and heat in the subsurface. Their links to natural hazards and natural resources make them important to human societies. A key problem in our understanding of these systems is how near-surface deformation physically connects to deformation at depth. Here, we combine structural data with U-Pb zircon and titanite geochronology in one of Earth's largest and deepest known exposures of an ancient, Cordilleran-style magmatic arc to investigate how two transpressional shear zones initiated and grew through continental lithosphere. An eastern, magma-starved shear zone nucleated in the middle crust as an oblique-reverse fault and propagated downward at 2–3 mm yr^{-1} as an outboard batholith subducted beneath Gondwana. A western, magma-rich shear zone initiated at the base of the crust and propagated upwards at ~3 mm yr^{-1}, reaching the upper crust after a few million years. Both systems show that the reactivation of inherited weaknesses localizes deformation at all depths. The western system shows how magma-deformation interactions influenced vertical connections and built a continental magmatic arc from the bottom up.

1. Introduction

Large faults and shear zones that accommodate lithospheric displacements govern the evolution of virtually every tectonic system on Earth. These structures also are important to societies because of their links to both natural hazards and natural resources, the latter due to their influence on fluid flow and the transfer of mass, heat, and elements through the lithosphere (Caine et al., 1996; Gale et al., 2014). Consequently, one of the

Methodology: Joshua J. Schwartz, Peter Lindquist
Project Administration: Keith A. Klepeis
Resources: Keith A. Klepeis, Joshua J. Schwartz, Rose Turnbull
Supervision: Keith A. Klepeis
Visualization: Elena Miranda, Richard Jongens, Rose Turnbull
Writing – original draft: Keith A. Klepeis
Writing – review & editing: Joshua J. Schwartz, Elena Miranda, Peter Lindquist, Richard Jongens, Rose Turnbull, Harold Stowell

long-term goals of the tectonics community is to determine how these systems form and evolve over time (Fossen & Cavalcante, 2017; Huntington & Klepeis, 2018; Tikoff et al., 2013).

Two of the most challenging aspects of achieving this goal have been (a) determining how near-surface deformation in fault zones physically connects to deformation in the deep crust and upper mantle and (b) determining how these connections, and the many properties that influence them, change over time. These problems have been difficult to solve because of the wide variety of styles and behaviors that operate on different time and length scales within these systems (Montési, 2013; Montési & Hirth, 2003; Platt & Behr, 2011; Rowe & Griffith, 2015). Understanding how deformation links across different layers in the crust and lithospheric mantle is especially problematic in regions where composition, strain rates, fluid flow, metamorphism, magmatism, partial melting, and other processes that affect rock rheology are heterogeneously distributed (Bürgmann & Dresen, 2008; Condit & Mahan, 2018; Gardner et al., 2017; Hacker et al., 2015; Kruckenberg et al., 2008; Orlandini & Mahan, 2020; Regan et al., 2014; Rey et al., 2017; Thatcher & Pollitz, 2008).

Despite these challenges, investigators have made significant progress in determining how flow in the deep lithosphere is linked to frictional processes in the shallow crust within different settings. In the San Andreas fault system, for example, field and geophysical studies suggest that the different layers of the lithosphere, and possibly the asthenosphere, can deform together rather than independently during the seismic cycle (Ford et al., 2014; Titus et al., 2007). In this same system, studies that combine experimental results with measurements on mantle xenoliths have suggested new ways in which transient flow in the upper mantle links to frictional processes in the seismogenic zone (Chatzaras et al., 2015). In New Zealand, zones of high fluid flow and seismic activity in the lower crust have been identified between the Alpine Fault and a 200 km-wide zone of distributed shear in the mantle (Houlié & Stern, 2012; Savage et al., 2007). Elsewhere, innovative approaches to studying fault zones use high-precision geochronology to determine deformation histories across a wide range of scales (Ault et al., 2015; Buriticá et al., 2019; Calzolari et al., 2018; Haines et al., 2016; Klepeis, Webb, Blatchford, Jongens, et al., 2019; McDermott et al., 2021; Oriolo et al., 2018; Sassier et al., 2009; Williams et al., 2017). These studies highlight the importance of integrating field-based investigations with other geological and geophysical approaches. They also show a need for more interdisciplinary work in natural systems where the connectivity of faults and shear zones can be examined directly. Key areas of uncertainty include: (a) the role of horizontal detachments in linking deformation within the lithosphere, (b) where and why anastomosing, mesh-like shear zones form, (c) the controls on shear zone width and how wide zones of shearing transition upward into discrete faults, (d) how partitioned and non-partitioned shear zone systems link with depth, (e) how the lower crust deforms beneath the seismogenic upper crust, and (f) whether magmatism and fluids drive shear zone growth and, if so, how?

Here, we combine structural data with 91 new U-Pb zircon and titanite dates to show how two lithospheric-scale transpressional shear zones formed and grew through an exhumed continental magmatic arc called the Median Batholith over a ~25 Ma period. This batholith represents Earth's largest (~4,500 km^2) and deepest (to 65 km depth) known exposure of a Cordilleran style magmatic arc, which originally was part of Gondwana (Figure 1) and is now located in SW New Zealand (Figure 2; Allibone, Jongens, Scott, et al., 2009; Allibone, Jongens,Turnbull, et al., 2009; Klepeis, Webb, Blatchford, Schwartz, et al., 2019; Mortimer, Gans, et al., 1999; Mortimer, Tulloch, et al., 1999; Tulloch & Kimbrough, 2003; I. M. Turnbull et al., 2010; R. Turnbull et al., 2010). Inside the batholith, two Cretaceous shear zone systems can be traced from upper to lower crustal depths using rock outcrops exposed at the Earth's surface (Figure 3). An eastern system, named here the Grebe-Indecision Creek shear zone, was magma-poor after ~137 Ma and formed a boundary between Mesozoic oceanic terranes to the east and the late Carboniferous edge of Gondwana to the west. A western system, which is centered on the George Sound shear zone (GSSZ), was magma-rich during the Early Cretaceous and was active during a terminal flare-up in arc magmatism. A comparison of these systems allows us, for the first time, to document when, where, how, and why each initiated and grew through the full thickness of continental lithosphere. Here, we reconstruct the structure of the Fiordland crustal section (Figures 3–7) and then use it to document the temporal evolution of deformation in the two shear zone systems, including the vertical connectivity of deformation throughout the lithosphere and its relationship to arc magmatism (Figures 5–13).

2. Geologic Setting and Previous Work

New Zealand lies within the mostly submerged continent of Zealandia, which formed along the SW margin of East Gondwana prior to the Late Cretaceous (Mortimer et al., 2017; Tulloch et al., 2019). Gondwana assemblages (Figures 1 and 2, green part of Figure 3b) are exposed within New Zealand's Western Province (Figures 1 and 2)

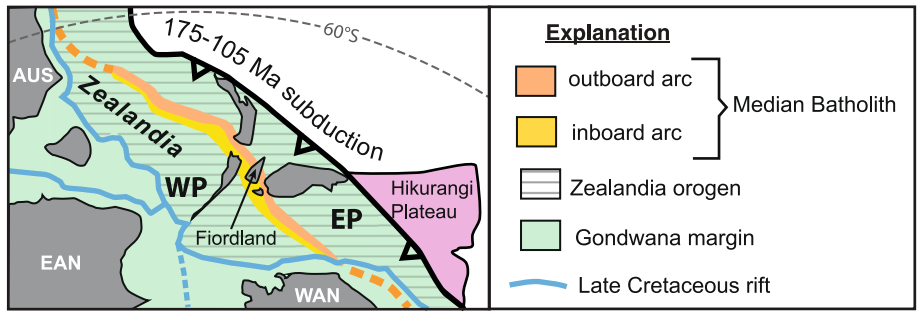

Figure 1. Reconstruction at ca. 90 Ma showing the inboard and outboard arcs of the Median Batholith within Gondwana (after Tulloch et al., 2019). The Hikurangi oceanic plateau is shown partially subducted beneath the Triassic-Early Cretaceous margin. Blue lines are sites of Late Cretaceous rifting and Gondwana breakup. EP, Eastern Province; WP, Western Province; AUS, Australia; EAN, East Antarctica; WAN, West Antarctica.

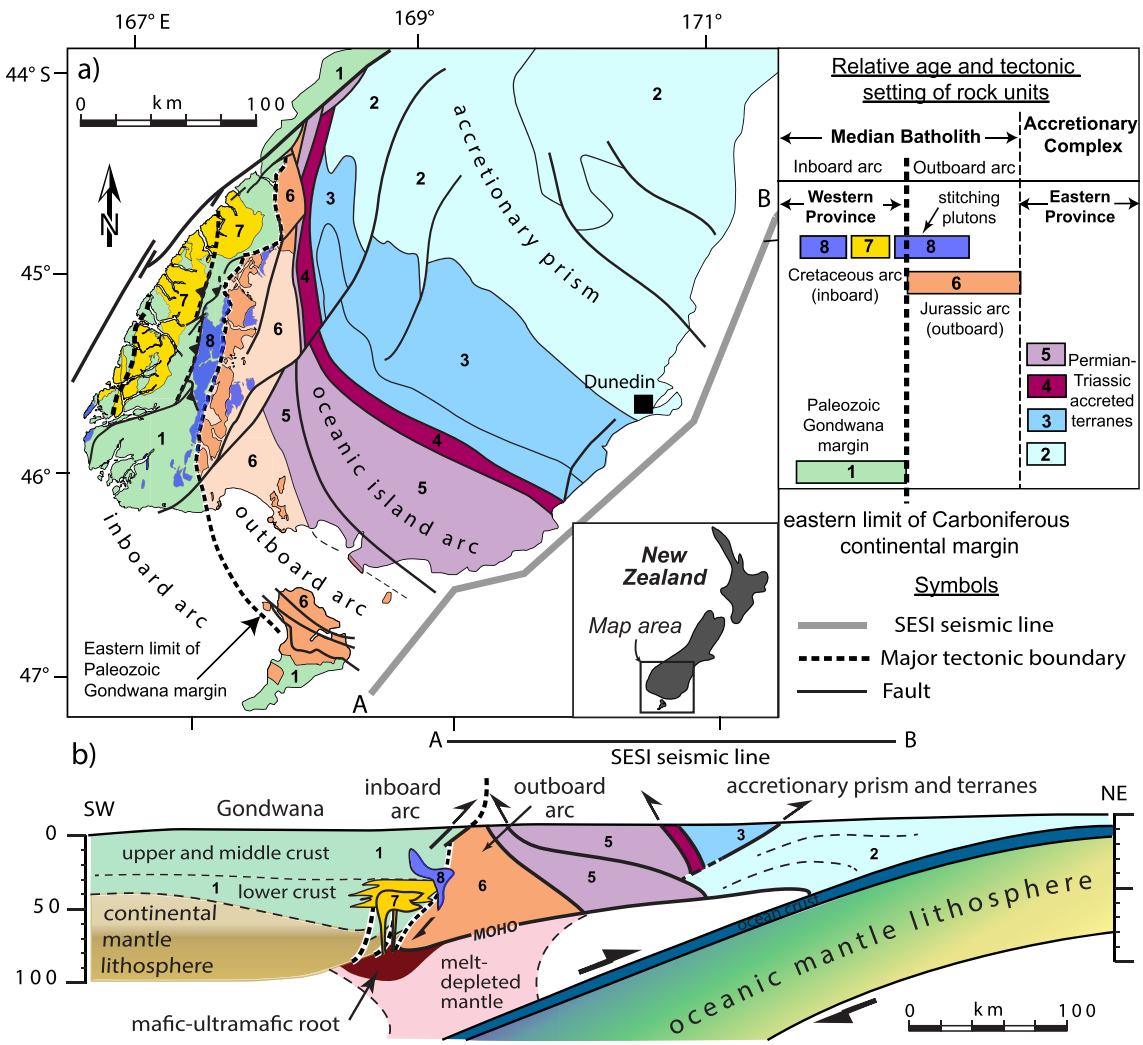

Figure 2. (a) Geologic map of the South Island, New Zealand showing components of Gondwana (Figure 1), including the Median Batholith and accreted terranes (modified from Mortimer et al. (2002)). Table summarizes the relative age of units (youngest at top) and tectonic setting (after Allibone, Jongens, Turnbull, et al., 2009). (b) Reconstructed profile based on surface geology, paleodepths of rock assemblages, and the South East South Island deep seismic reflection profile of Mortimer et al. (2002). Geometry of the inferred oceanic slab mimics that beneath the central Andes (Oncken et al., 2003), which shows a similar style and scale.

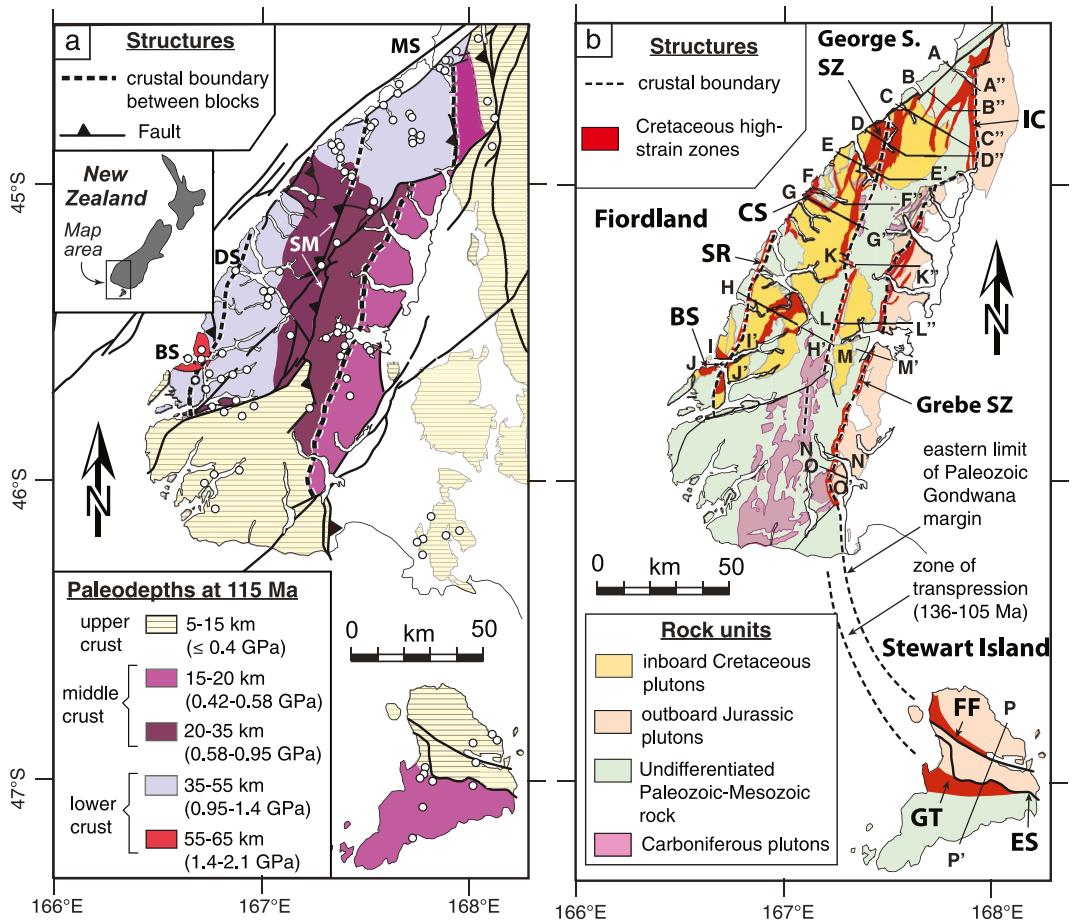

Figure 3. (a) Map showing Cretaceous paleodepths and crustal divisions in Fiordland and Stewart Island (modified from Klepeis, Webb, Blatchford, Schwartz, et al., 2019). White circles are sites where pressures calculated from mineral assemblages record the peak of Cretaceous metamorphism and pluton emplacement depth at 120–110 Ma (0.1 GPa = 3.7 km, uncertainties are ±0.1 GPa) (after compilation in Klepeis et al., 2022). Extrapolations between sites are based on the age and history of Cretaceous metamorphism. SM is Spey-Mica Burn fault system. (b) Map showing Early Cretaceous high-strain zones at ~115 Ma. Cross sections A-A′–P-P′ are shown in Figure 5 and Figures S3 and S4 in Supporting Information S1. BS, Breaksea domes; CS, Caswell thrust belt; DS, Doubtful Sound; ES, Escarpment fault; FF, Freshwater fauLt system; Grebe SZ, Grebe shear zone; George S. SZ, George Sound shear zone; GT, Gutter shear zone; IC, Indecision Creek shear zone; MS, Milford Sound; SR, Straight River shear zone. Correlation of Cretaceous transpression between Fiordland and Stewart Is. After Allibone and Tulloch (2008).

where Paleozoic-Mesozoic, subduction-related plutons intruded Cambrian-Early Devonian metasedimentary and metavolcanic rock (Mortimer, 2004; Mortimer, Gans, et al., 1999; Tulloch, Ramezani, Kimbrough, et al., 2009). In the Eastern Province, Triassic-Early Cretaceous plutons intruded Permian-Cretaceous terranes that accreted onto Gondwana during subduction (Mortimer, 2004; Mortimer, Gans, et al., 1999). Separating these two provinces is the Median Batholith (Figures 1–3), which Mortimer, Gans, et al. (1999) defined as a 10,200 km^2 region where variably deformed Carboniferous to Early Cretaceous plutons intruded rocks of both the Eastern and Western provinces. Tulloch et al. (2019) showed that correlative rocks occur offshore and south of New Zealand for >2,600 km along the Gondwana margin (Figure 1).

Inside the Median Batholith, a major structural and isotopic boundary separates outboard (eastern) and inboard (western) belts, marking the eastern limit of the late Paleozoic Gondwana margin (Allibone, Jongens, Scott, et al., 2009; Milan et al., 2017; Mortimer, Gans, et al., 1999; Scott et al., 2011; Tulloch & Kimbrough, 2003; Figures 2 and 3). Turnbull et al. (2021) and Schwartz et al. (2021) showed that this boundary likely extends into the mantle lithosphere where it separates distinctive isotopic domains. Minor Devonian plutons only occur west of the boundary. Carboniferous plutons are abundant in the west and are concentrated along the shear zones that

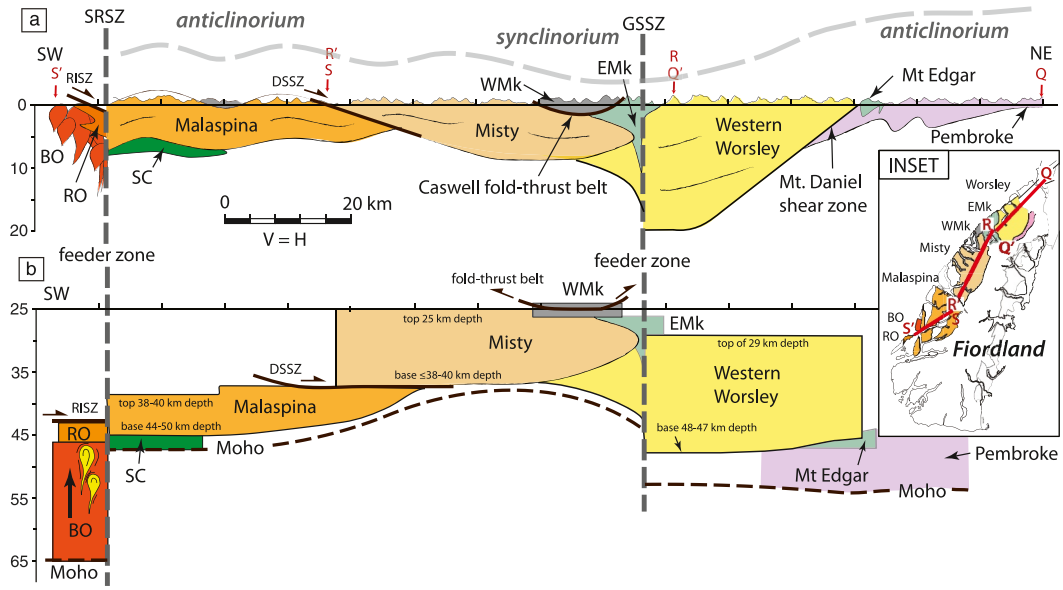

Figure 4. (a) NNE-SSW composite profile showing the anatomy of layered intrusions in western Fiordland. Inset shows locations of profiles Q to S′ and plutons of the inboard batholith. Pre-batholithic host rock has been removed for clarity. Plutons are folded into a broad synclinorium and two anticlinoriums (gray dashed line), exposing two titled sections of lower crust. (b) Unfolded profile showing inferred Early Cretaceous Moho (black dashed lines). EMk, Eastern McKerr pluton; WMk, Western McKerr pluton; GSSZ, George Sound shear zone; SRSZ, Straight River shear zone; DSSZ, Doubtful Sound shear zone; RISZ, Resolution Island shear zone.

are the primary focus of this paper (Figure 3b). These latter plutons have distinctive A-type geochemistries and appear to have been emplaced along translithospheric structures (Allibone & Craw, 2016; Allibone, MacKenzie, Turnbull, Tulloch, & Craw, 2016, Allibone, MacKenzie, Turnbull, Tulloch, Craw, & Palin, 2016).

From Permian to Early Cretaceous times, arc magmatism was focused within a ~20 km-wide zone centered on and east of the boundary between inboard and outboard belts of the Median Batholith (Ringwood et al., 2021; Schwartz et al., 2021; Tulloch and Kimbrough, 2003). After a flare-up of magmatism in the eastern outboard belt between c. 147 and 136 Ma, which produced Darran Suite plutons in Fiordland (Kimbrough et al., 1994; Mortimer, Tulloch, et al., 1999; Muir et al., 1998; Schwartz et al., 2017), Southland (McCoy-West et al., 2014), and Stewart Island (Allibone & Tulloch, 2004; R. Turnbull et al., 2010), magmatism migrated into the Gondwana interior (Schwartz et al., 2017). The inboard belt (Figure 3b) includes 129–110 Ma plutons of the Western Fiordland Orthogneiss (WFO), which intruded the lower and middle crust of the Cretaceous arc (Allibone, Jongens, Turnbull, et al., 2009; Bradshaw, 1989, 1990; Chapman et al., 2016; Muir et al., 1998; Schwartz et al., 2017; this study). This inboard batholith consists of the mostly dioritic to monzodioritic Worsley, Misty, and Malaspina plutons (Figure 4; Allibone, Jongens, Turnbull, et al., 2009). The emplacement of these plutons, and other bodies that intruded the middle and upper crust west of the boundary (making up most of the Separation Point Suite), constitute a second flare-up in arc magmatism that peaked at 118–115 Ma and was sourced primarily from the mantle (Carty et al., 2021; Decker et al., 2017; Schwartz et al., 2017, 2021).

As the WFO and other Early Cretaceous plutons were emplaced, the middle and lower crust of the arc experienced high-grade metamorphism and partial melting (Allibone, Jongens, Turnbull, et al., 2009, Allibone, Milan, et al., 2009; Bradshaw, 1989, 1990; Clarke et al., 2000, 2005; N. Daczko et al., 2001; Daczko et al., 2009; Hollis et al., 2003; Oliver and Coggon, 1979; Stowell et al., 2010; Stuart et al., 2016; Tulloch et al., 2011). High-pressure metamorphic mineral assemblages of the garnet granulite, omphacite granulite, and, locally, eclogite facies occur within the western belt (Chapman et al., 2015; Clarke et al., 2013; De Paoli et al., 2009; Stowell et al., 2014, 2017; R. Turnbull et al., 2010).

Transpressional and contractional deformation accompanied Early Cretaceous magmatism and metamorphism at all crustal depths. In northern Fiordland, it produced the Indecision Creek shear zone (Buriticá et al., 2019; Klepeis & King, 2009; Klepeis et al., 2004; Marcotte et al., 2005), the Mt Daniel shear zone (Bhattacharya et al., 2018;

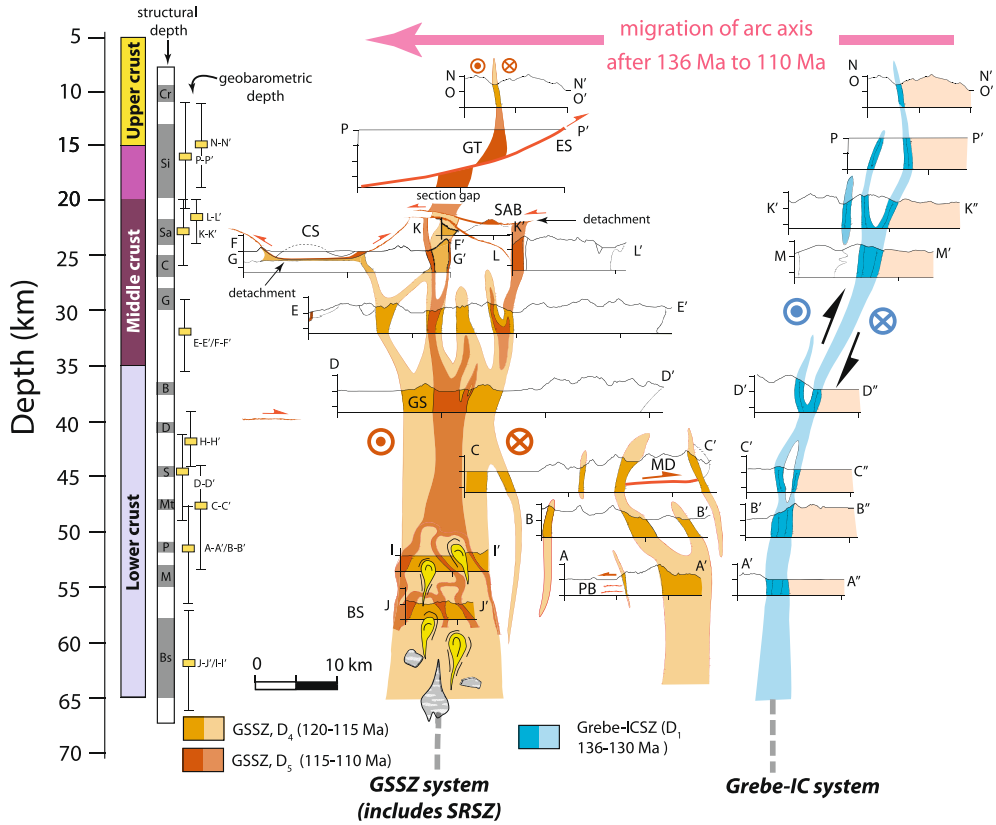

Figure 5. Reconstructed profiles through the Median Batholith showing high-strain zones by depth. A western shear zone system includes the George Sound (GSSZ) and Straight River shear zones (SRSZ), Breaksea domes (BS), the Caswell (CS) and South Adams Burn (SAB) thrust belts, the Mt Daniel shear zone (MD), Pembroke thrust (PB), and Escarpment fault (ES). An eastern system includes the Grebe and Indecision Creek shear zones (Grebe-IC), and the Freshwater fault. The Gutter shear zone (GT, Stewart Island) can be considered part of either system. We place it with the GSSZ on the basis of similarities in style, depth range, and age with the Caswell and South Adams Burn thrusts. Paleodepths of each profile were determined using both structural and geobarometric data. Dark colors correspond to profiles A-A′′–P-P′′ (locations in Figure 3b), light colors show correlations between profiles. Profiles are simplified to show only high-strain zones, complete profiles are in Figures S2–S4 in Supporting Information S1. Geographic locations (structural depth column): Bs, Breaksea entrance; M, Milford Sound; P, Poison Bay; Mt, Mt. Daniel; S, Sutherland Sound; D, Doubtful Sound; B, Bligh Sound; G, George Sound; C, Caswell Sound; Sa, S. Adams Burn; Si, Stewart Island; Cr, Caroline peak. Migration of arc axis is from Schwartz et al. (2021).

Klepeis et al., 2004), and the Pembroke Thrust (N. R. Daczko et al., 2001; Klepeis & King, 2009). In central and southern Fiordland, it produced the Grebe (Buriticá et al., 2019; McGinn et al., 2020; Negrini et al., 2018; Scott et al., 2011, 2014), George Sound (Allibone, Jongens, Turnbull, et al., 2009; Klepeis et al., 2004), Straight River (King et al., 2008), and Misty (Blatchford et al., 2020) shear zones. Mid-crustal deformation also formed the South Adams Burn (SAB) (Blatchford et al., 2020) and Caswell (Daczko et al., 2002b) thrust belts, and, in the lower crust, the Breaksea and Malaspina Domes (Betka & Klepeis, 2013; Klepeis et al., 2016; Miranda and Klepeis, 2016). On Stewart Island, the Gutter shear zone, the Freshwater Fault System and the Escarpment fault (Allibone & Tulloch, 2008) form part of the Early Cretaceous system. Klepeis, Webb, Blatchford, Schwartz, et al. (2019) and Klepeis, Webb, Blatchford, Jongens, et al. (2019) showed that many of these Cretaceous shear zones were reactivated by Cenozoic faulting.

During the Late Cretaceous, the Median Batholith underwent a transition from contraction and crustal thickening to extension and crustal thinning (Klepeis et al., 2007, 2016; Schwartz et al., 2016; Stowell et al., 2014; Tulloch, Ramezani, Mortimer, et al., 2009; Tulloch et al., 2019). Amphibolite-facies metamorphism and high lower-crustal temperatures persisted during this transition (Gibson & Ireland, 1995; Schwartz et al., 2016). Although its exact timing is still debated, extension was well underway by ~100 Ma and possibly earlier in some places. In Fiordland, the Doubtful Sound (Figure 4) (Gibson et al., 1988; Klepeis et al., 2007; Oliver, 1990),

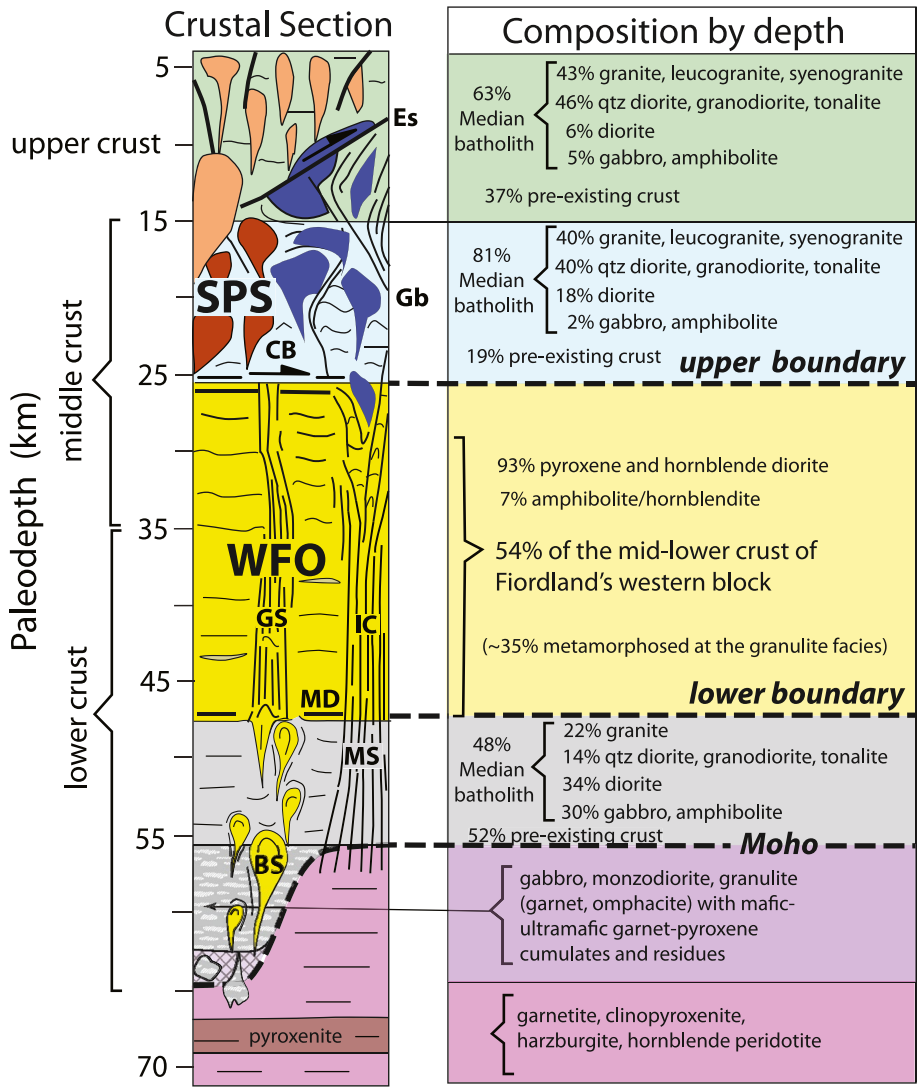

Figure 6. Vertical section through the Median Batholith showing variations in average rock composition by depth. Compositions were calculated using volume-integrated compositions of mapped units (after I. M. Turnbull et al., 2010, R. Turnbull et al., 2010) in each crustal block in Figure 3a (see Text S1 in Supporting Information S1 for methods). Diagram highlights major compositional boundaries, including at the top and base of the Western Fiordland Orthogneiss (WFO). The Separation point Suite (SPS) represents the mid-upper crustal portion of the Median Batholith. Pre-existing crust is composed of Paleozoic Gondwana margin assemblages. MS, Milford Sound; BS, Breaksea Sound; MD, Mt Daniel shear zone; GS, George Sound shear zone; IC, Indecision Creek shear zone; Gb, Grebe shear zone; CB, Caswell fold-thrust belt; ES, Escarpment fault.

Resolution Island (Allibone, Jongens, Turnbull, et al., 2009; Betka & Klepeis, 2013; De Paoli et al., 2009; Klepeis et al., 2007, 2016), and Mt Irene shear zones (Scott & Cooper, 2006) accommodated the extension. On Stewart Island, the Sisters shear zone accommodated extension (Kula et al., 2007; Ring et al., 2015). By ~83 Ma, Gondwana had fragmented (rifts shown in Figure 1) and Zealandia had separated from Australia and Antarctica (Gaina et al., 1998).

During the late Cenozoic, dextral strike-slip motion along the Alpine Fault system offset the Median Batholith in New Zealand's South Island by ~460 km (Sutherland, 1999) and uplifted basement rock. In Fiordland, two steep, downward-curving reverse faults in the Spey-Mica Burn fault system (Figure 3a) uplifted and imbricated large slices of crust in the Late Miocene (Klepeis, Webb, Blatchford, Schwartz, et al., 2019, Klepeis, Webb, Blatchford, Jongens, et al., 2019). These slices juxtapose crust from different Early Cretaceous paleodepths (Figure 3a). Southwest Fiordland and regions east of Fiordland preserve Cretaceous upper crust. Another crus-

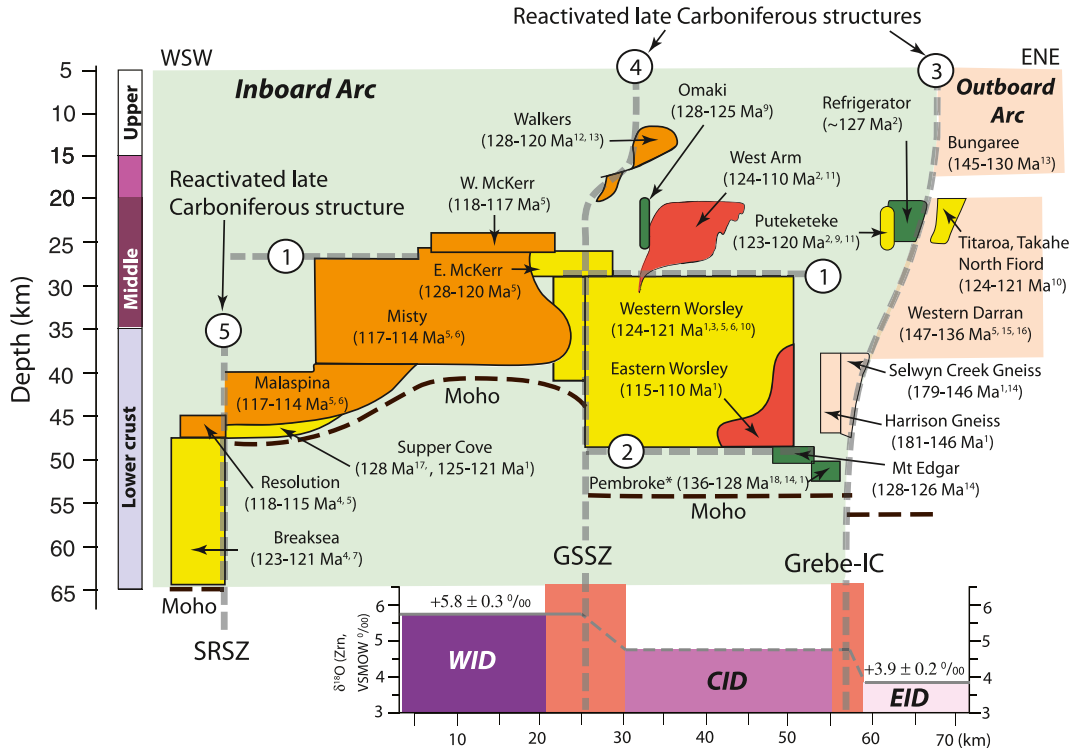

Figure 7. Profile sketch of the Median Batholith showing pluton emplacement depths and the locations of the five major compositional and rheological boundaries discussed. Pluton colors indicate in which of five age-ranges each pluton was emplaced. These age-ranges correspond to the D_1-D_5 tectonic events discussed in the text (see also Figures 9 and 10): tan (≥130 Ma), dark green (129–124 Ma), yellow (124–121 Ma), orange (120–115 Ma), red (115–110 Ma). Green background is undifferentiated rock of Gondwana margin. Boundaries include tops of the Misty and Western Worsley plutons (a), bottom of the Western Worsley pluton (b), and the Early Cretaceous Moho. Three subvertical boundaries (3, 4, and 5) coincide with the Grebe-IC, George Sound (GSSZ), and Straight River (SRSZ) shear zones, respectively. Graph at the bottom shows that two of the vertical boundaries coincide with isotopic zones in the lithospheric mantle (after Schwartz et al., 2021; Turnbull et al., 2021): WID; western isotopic domain, CID; central isotopic domain, EID; Eastern isotopic domain. References: 1. this study, 2. Buriticá et al. (2019), 3. Bhattacharya et al. (2018), 4. Stowell et al. (2017), 5. Schwartz et al. (2017), 6. Milan et al. (2016), 7. Klepeis et al. (2016), 8. Scott et al. (2009), 9. Ramezani and Tulloch (2009), 10. Bolhar et al. (2008), 11. Scott and Palin (2008), 12. Allibone and Tulloch (2008), 13. Allibone and Tulloch (2004), 14. Hollis et al. (2003), 15. Muir et al. (1998), 16. Kimbrough et al. (1994), 17. Tulloch and Kimbrough (2003), 18. Stowell et al. (2010). *Pembroke records a Paleozoic protolith with Cretaceous granulite-facies metamorphism at 136–128 Ma (Stowell et al., 2010; Tulloch et al., 2011; this study).

tal slice centered on the Grebe shear zone exposes Jurassic and older plutons that represent Cretaceous middle crust (Figures 3a and 3b). This mid-crustal segment preserves upper and lower blocks, with deeper middle crust occurring west of the Grebe-IC shear zone (Figure 3a). A western slice exposes the deepest parts of the batholith. Motion on these steep reverse faults was mainly vertical (Klepeis, Webb, Blatchford, Schwartz, et al., 2019, Klepeis, Webb, Blatchford, Jongens, et al., 2019). This configuration allows us to trace structures from upper to lower crustal depths and to evaluate processes within a nearly complete section of continental arc crust (Figure 5).

3. Methods

3.1. Reconstructing the Depth Section

To reconstruct the Cretaceous section, we used structural data (Figure S1 in Supporting Information S1), published thermobarometric data from metamorphic mineral assemblages and estimates of pluton emplacement depths where the ages of these features are well-known (data set in Table S1, Klepeis et al., 2022). The results (Figures 3a and 5, Table 1) provides a snapshot of crustal depths at ~115 Ma when the inboard part of the Median Batholith was still under construction. Five crustal subdivisions (Figure 3a) show a general increase in the depth of exposure from east to west across Fiordland and from north to south on Stewart Island. The bound-

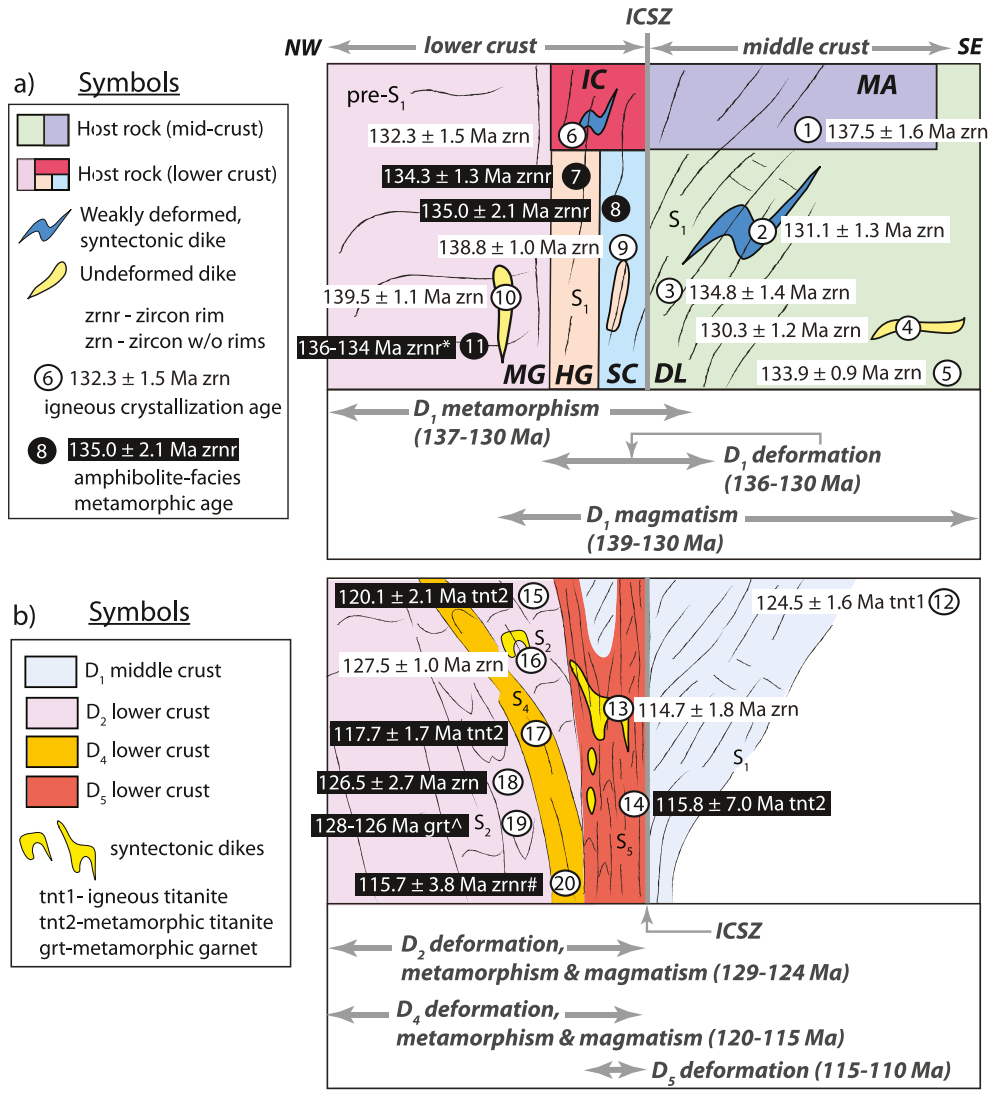

Figure 8. Profile sketches illustrating sampling strategy and approach to combining structural data with geochronology. Photos of field relationships are shown in Figures S5 and S6 in Supporting Information S1. (a) Summary of U-Pb zircon geochronology that reveals the evolution of D_1 magmatism, amphibolite-facies metamorphism and deformation across the Indecision Creek shear zone. (b) Sketch illustrating the use of multiple mineral chronometers to determine the spatial and temporal evolution of D_2-D_5 events in the Indecision Creek shear zone (same region as Figure 8a). Rock units: DL, Darran Leucogabbro; HG, Harrison Gneiss; IC, Indecision Creek Complex; MA, Mt Anau Complex; MG, Milford Gneiss; SC, Selwyn Creek Gneiss; ICSZ, Indecision Creek shear zone. All ages are from this study except: *Tulloch et al. (2011), #Marcotte et al. (2005), ^Stowell et al. (2010). Samples (circled numbers) are: 1. 18WA568, 2. 18MS01 A, 3. 18MS01D, 4. 18MS03 B, 5. 18MS03 A, 6. 18WA560 B, 7. 15NZ58, 8. 15NZ60, 9. 18MS06, 10. 15NZ66, 12. 18WA165 A, 13. 18MS22 A, 14. 18MS01 B, 15. 18WA153, 16. 18WA554 A, 17. 18WA151, 18. 05NZ12P. Errors are 2SD. Dates summarized in Tables 2 and 3.

aries between the layers are the same as those defined by Klepeis et al. (2007) and were chosen to highlight a section of middle crust within west-central Fiordland that transitions downwards into two lower crustal sections: one in northern Fiordland near Milford Sound and the other between Doubtful and Breaksea sounds (Figure 3a).

Next, to further calibrate the paleodepths of structures and to calculate layer thicknesses, we constructed 19 profiles across Fiordland (Figures 3b, 4, and 5) and used thousands of structural measurements to trace features between them (data points shown in Figure S1 in Supporting Information S1) (complete profiles and data in Figures S3 and S4 in Supporting Information S1). One of the profiles is a ~125 km-long, NE-SW cross section that spans the entire western block (Figure 4). This profile is oriented perpendicular to the regional strike of both

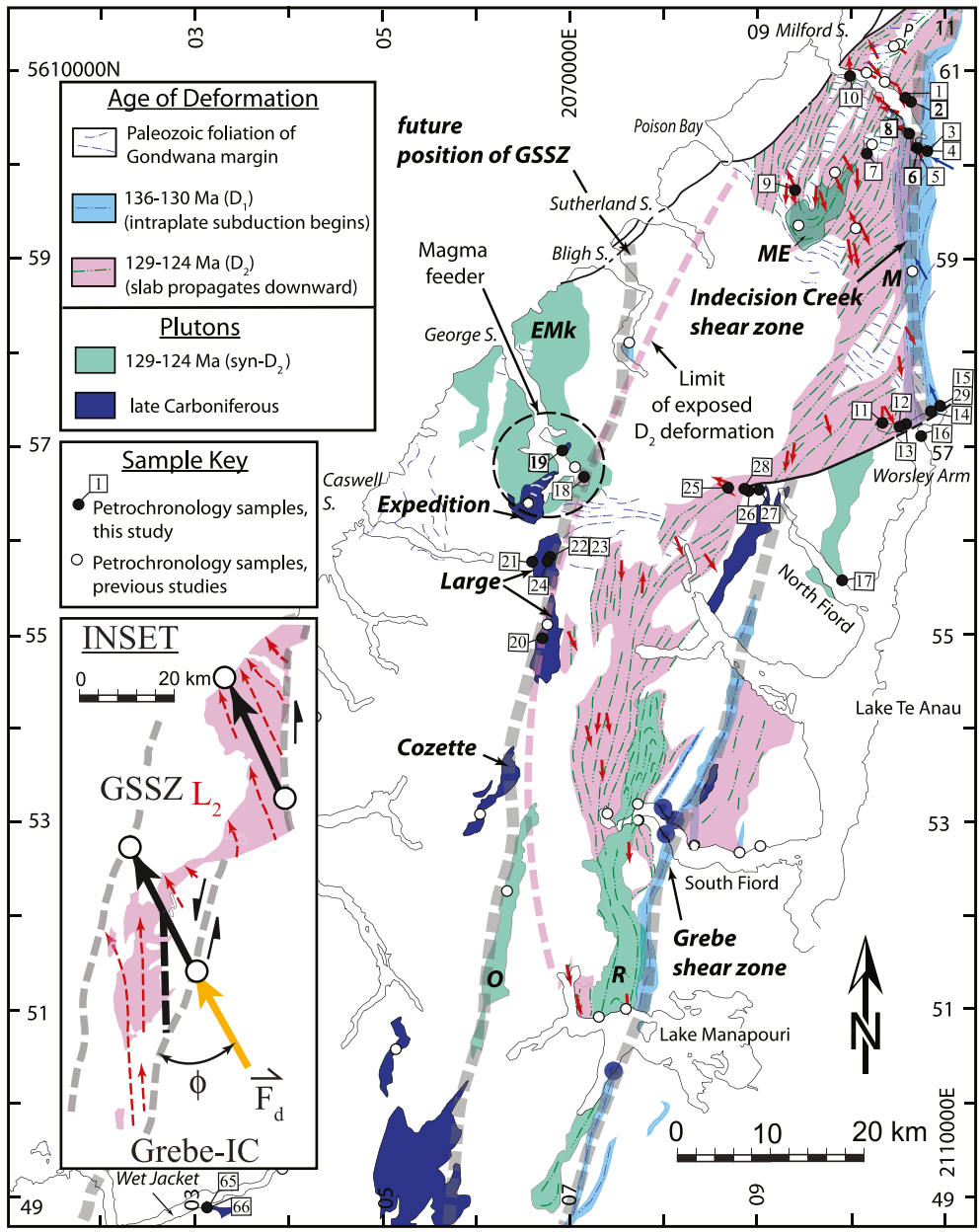

Figure 9. Map of N. Fiordland showing trends of inherited Paleozoic foliations, D_1 and D_2 fabric trajectories, and the western limit of exposed D_2 deformation in the vicinity of the Grebe-IC shear zone. Red arrows show trends of L_2 mineral stretching lineations. Dashed black circle shows magmatic feeder centered on the future George Sound shear zone. Dark blue dots showing Carboniferous intrusions along the southern part of the Grebe shear zone are from Ringwood et al. (2021). Inset shows interpreted displacement history: dashed red lines with arrows are L_2 lineation trajectories showing the bulk displacement direction of the underthrust outboard arc. Black arrows show shear directions and minimum (solid) and maximum (dashed) displacements. Orange arrow shows inferred orientation of the displacement vector ($\vec{F}_d$) at angle ϕ from the shear zone boundary (boundary defined by the trace of the Grebe-IC). Plutons: ME, Mt Edgar pluton; EMk, Eastern McKerr pluton; R, Refrigerator pluton; O, Omaki orthogneiss. Geographic locations: M, Mt Mitchelson; P, Pembroke Valley. Petrochronology samples from this study (numbers in boxes) are keyed to zircon and titanite ages in Tables 2 and 3.

Paleozoic layering and the upper and lower boundaries of the Western Worsley and Eastern McKerr plutons, which exploited this layering. This orientation, thus, is ideal for calculating the pluton thicknesses, and for determining how far above and below them the other profiles project (see also Figure S2 in Supporting Information S1). The NE-SW profile also shows two broad anticlinoriums and one synclinorium centered on the Western

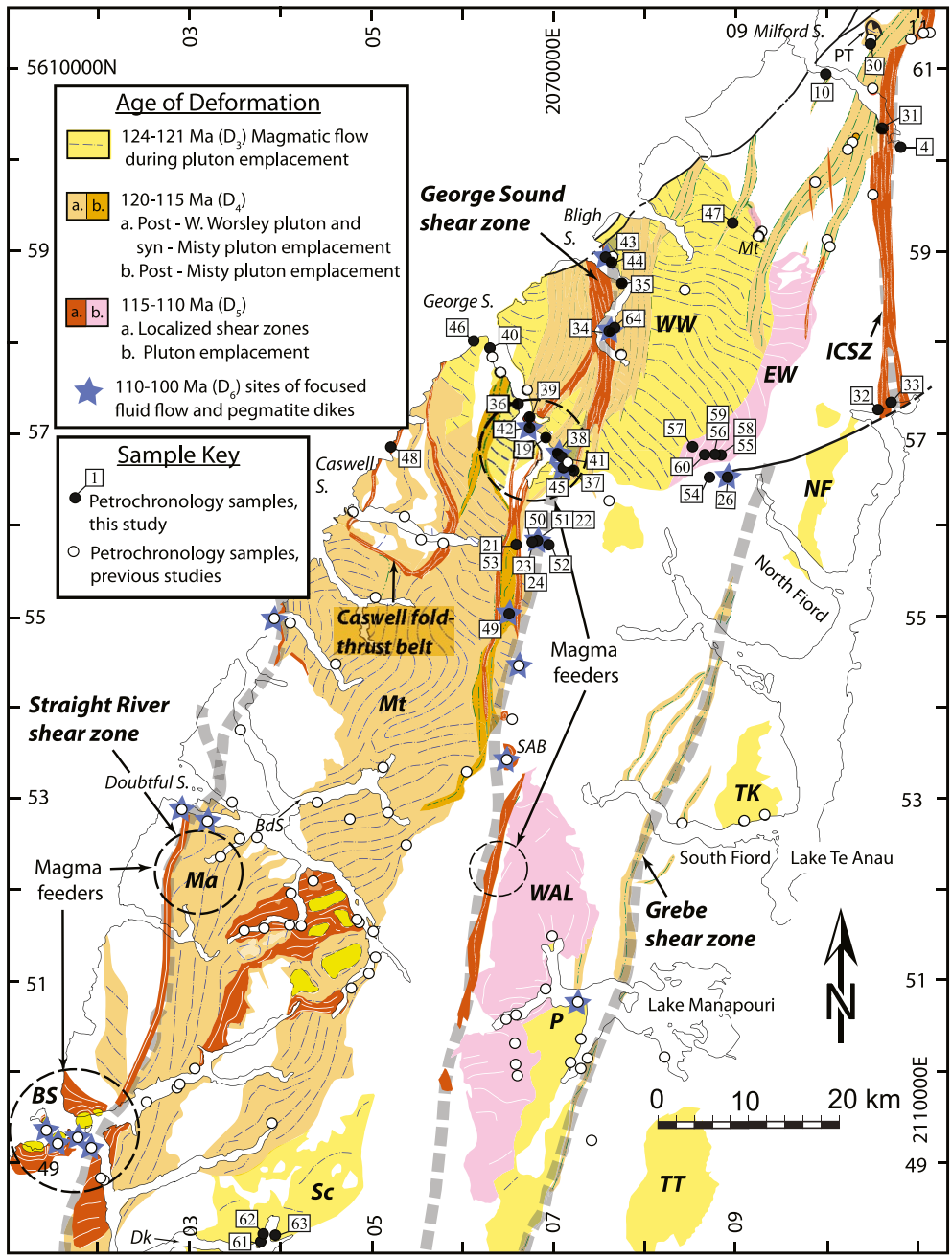

Figure 10. Map showing the extent of D_3 magmatism and subsequent (D_4-D_6) deformation stages. Thin dashed lines are fabric trajectories in the vicinity of the George Sound and Grebe-IC shear zones. Petrochronology samples from this study (numbers in boxes) are shown (ages in Tables 2 and 3). Dashed black circle shows magmatic feeders centered on the George Sound and Straight River shear zones. Plutons: BS, Breaksea domes; EM, Eastern Worsley pluton; Mt, Misty pluton; Ma, Malaspina pluton; P, Puteketeke pluton; Sc, Supper Cove pluton; WW, Western Worsley pluton; WAL, West Arm leucogranite; NF, North Fjord pluton; TK, Takahe pluton; TT, Titiroa pluton. Other abbreviations: BdS, Bradshaw sound; Dk, Dusky sound; DS, Doubtful sound; Mt, Mt. Daniel (and Mt Daniel shear zone); SAB, South Adams Burn; PT, Pembroke thrust; ICSZ, Indecision Creek shear zone.

McKerr pluton (Figure 4a). The hinges of the gentle folds are horizontal and trend 290°, nearly perpendicular to the strike of the GSSZ. They lack an axial planar foliation and are restricted to the hanging wall of late Miocene reverse faults (Klepeis, Webb, Blatchford, Schwartz, et al., 2019, Klepeis, Webb, Blatchford, Jongens, et al., 2019), suggesting that they formed during the Miocene-Pliocene. The reverse faults are steep and the

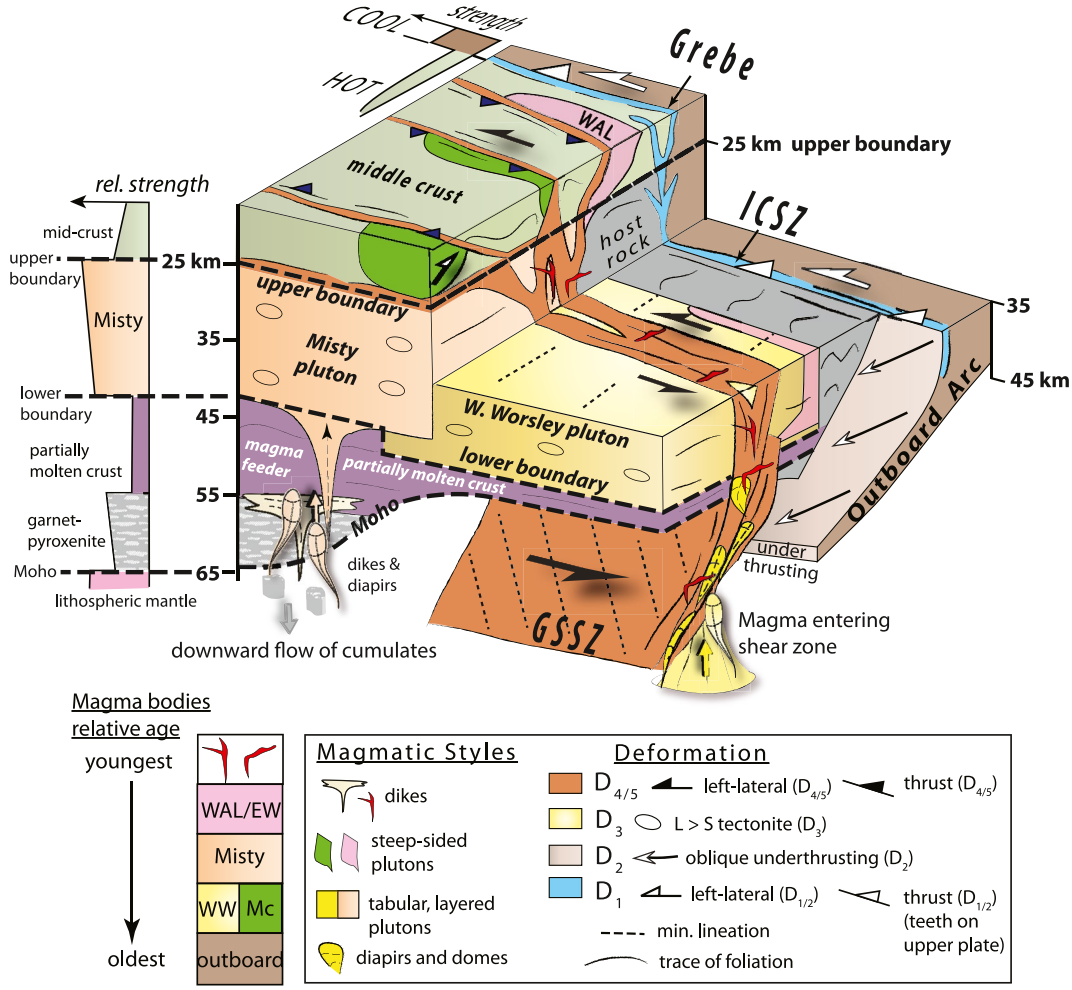

Figure 11. Block sketch summarizing the 3-D architecture of the Median Batholith's middle and lower crust. Oblique underthrusting of the outboard arc beneath Gondwana occurred along the Grebe-Indecision Creek shear zone (Grebe-ICSZ). Vertical variations in the age and style of plutons in the George Sound shear zone (GSSZ), which cuts across three compositional boundaries, also are shown. Colors correspond to age intervals D_1-D_5 defined in the text (D_4 and D_5 have been combined for simplicity). D_6 is represented by red, cross-cutting dikes. Schematic strength envelope at top right shows a contrast between cool, strong crust of the outboard arc and hot, weak crust of the Gondwana margin at ~130 Ma. By ~110 Ma, the Misty pluton formed a strong layer between weak mid-crustal assemblages and hot, weak lower crust (vertical envelope on left). See text for discussion. WAL, West Arm leucogranite; WW, Western Worsley; EW, Eastern Worsley; Mc, Eastern McKerr pluton.

displacements on them nearly vertical (Blatchford et al., 2020; Klepeis, Webb, Blatchford, Schwartz, et al., 2019, Klepeis, Webb, Blatchford, Jongens, et al., 2019), resulting in little tilting in an E-W direction. The unfolded profile (Figure 4b), combined with layer thicknesses and the thermobarometric data, allowed us to reconstruct the relative depths of structures more precisely than with the geobarometric data alone (Figure 5; Table 1). Unfolding does not affect the orientation of structures near Caswell Sound and reduces the dip of the GSSZ at Bligh Sound by ≤5° (Figure 4).

Once the relative and absolute paleodepths of structures were calibrated using combinations of structural data and published thermobarometry, we examined other characteristics of the crustal section by depth. One of these is average rock composition (Figure 6). This analysis (methods and sources described in Text S1 in Supporting Information S1) highlights the location of three compositional boundaries that vertically stratify the crust (Section 4.1). Figure 7 breaks up the Median Batholith into its constituent plutons and highlights their location relative to three vertical structural boundaries, across which estimates of crustal thickness vary (Section 4.1).

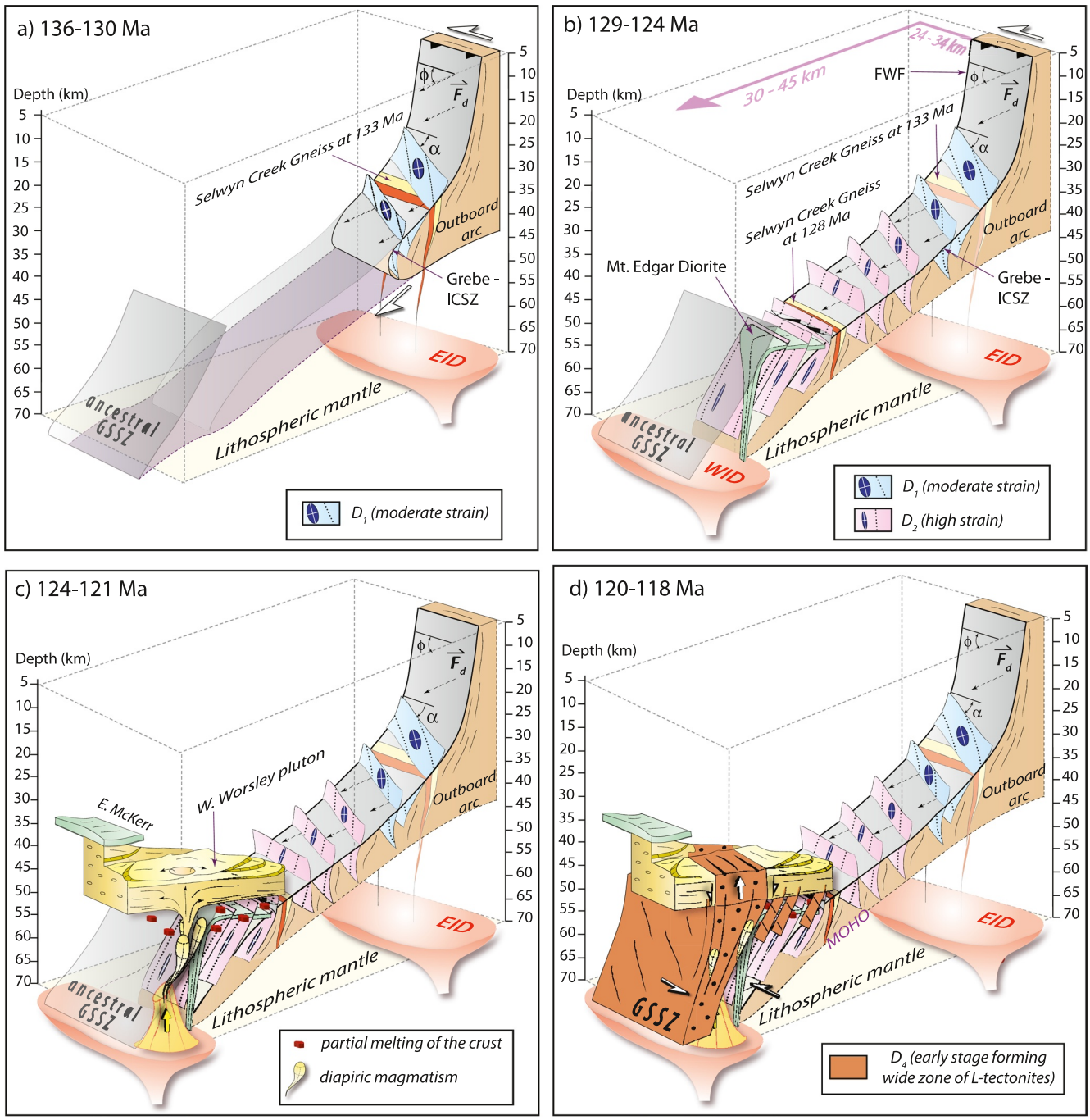

Figure 12. Model of transpressional shear zone growth within the Median Batholith from 136 to 118 Ma. Oblique underthrusting of the outboard arc beneath Gondwana along the Grebe-IC shear zone (Grebe-ICSZ) following a period of Darran Suite magmatism in the Eastern Isotopic Domain (EID). Foliations steepen to vertical and rotate counterclockwise during transition from (a) D_1 (136–130 Ma) to (b) D_2 (129–124 Ma). $\vec{F}_d$ and ϕ are same as inset in Figure 9. Angle between foliation strike and shear zone boundary (α) shown. (c) Underthrusting of the outboard arc slows or stops as high addition rate magmatism (D_3) initiates along the ancestral George Sound shear zone (GSSZ) boundary, tapping the Western Isotopic Domain (WID). (d) Transpressional deformation in the GSSZ (early D_4) initiates during emplacement of the Western Worsley pluton prior to emplacement of the Misty pluton.

The final stage of the reconstruction involved correlating structures and events between profiles. To accomplish this, we determined the relative sequence of magmatism, metamorphism, and deformation within each region using cross cutting relationships among rock fabrics, mineral assemblages, and intrusions. Next, we determined the absolute ages of these features using 74 new U-Pb zircon dates (Table 2) and 17 new titanite U-Pb dates

Table 1
Summary of Cretaceous Paleodepths for Each Crustal Profile at ~115 Ma (Full Data Set and Ages in Table S1)

Profile[a]	Location	Crustal block[b]	Geological feature	Structural depth[c] (km)	Geobarometry (GPa)[d]	Geobarometric depth[e] (km)	Interpreted depth (km)
N-N′/O-O′	Caroline Peak	Upper	Grebe shear zone	11–10	5.4–3[7]	19–11	11–7
P-P′	Stewart Is.	Upper	Escarpment fault	21–9	5.6–2.5[8]	21–9	20–13
L-L′/M-M′	L. Manapouri	Middle	Putekeke/Refigerator pluton	24–20	6.1[7]	24–20	24–20
K-K′	South Adams	Middle	Thrust/Misty pluton top	24–22	7.1–5.5[7]	26–20	24–22
F-F′/G-G′	Caswell S.	Middle	Thrust/Misty pluton top	27–25	7.9[6]	~29	27–25
E-E′	George S.	Middle	Worsley top/E. McKerr base	30–28	9.6–8[5]	35.5–29	30–29
D-D′	Bligh S.	Lower	Inside Worsley pluton	37.6–36.6	13.3–11[3]	49–41	37–36
H-H′	Doubtful/Bradshaw	Lower	Inside Misty pluton	41–40	12-10.5[9, 10]	44–39	41–40
C-C′	Sutherland S.	Lower	Inside Worsley pluton	45–44	13.3–11[3]	48–41	45–44
C-C′	Mt Daniel	Lower	Worsley pluton base	48–47	14.5–12[3]	53.6–44	48–47
B-B′	Poison Bay	Lower	Below Worsley pluton	52–51	15–11[4]	55.5–41	52–51
A-A′	Milford/Pembroke	Lower	Below Worsley pluton	55–53	14.1 ± 1.2[2]	56.6–47.7	55–53
J-J′/I-I′	Breaksea Entrance	Lower	Decompressing mafic root	65–50	1.8–1.2[1]	66.6–44.4	65 to 55-45

Note. References for geobarometry: 1. Stowell et al. (2017), 2. N. Daczko et al. (2001), 3. Daczko et al. (2009), 4. Bradshaw (1989), 5. Anderson et al. (2019), 6. Daczko et al. (2002a, 2002b, 2002c), 7. Scott et al. (2009), 8. Allibone and Tulloch (2008), 9. H. Stowell, personal communication (2013), 10. Stowell et al. (2014).

[a]Selected profiles used in Figure 5 and Figures S3–S4 in Supporting Information S1 from shallowest (top) to deepest (bottom). Profile locations in Figure 3b. [b]Crustal divisions shown in Figure 3a. [c]Structural geometry and depth calibration shown in Table S1 and Figures S2, S3, and S4 in Supporting Information S1. Depths based on structural data are anchored at the base and top of the Worsley pluton at Mt Daniel and George Sound, respectively, and Pembroke Valley near Milford Sound. The combined data sets allowed us to calibrate mid-crustal depths better than using geobarometry alone because the latter involves more uncertainty. [d]Selected geobarometric data summarized from compilation of Klepeis, Webb, Blatchford, Schwartz et al. (2019). Tabulated data are closest to profile locations. Full data set and ages shown in Table S1. Errors on pressures are ±0.1 GPa unless otherwise indicated. [e]Depths based on 0.1 GPa = 3.7 km after Allibone and Tulloch (2008) and Allibone, Jongens, Turnbull, et al. (2009).

(Table 3), and published geochronology cited throughout the text. Sample localities and the results of these correlations are shown in Figures 8–10 (site numbers are keyed to samples in Tables 2 and 3). Section 3.2 describes how we constructed a structural and temporal framework for the tectonic events.

3.2. Zircon and Titanite Geochronology

3.2.1. Sampling Strategy and Approach

To establish a regional framework of tectonic events, we sampled 74 variably deformed intrusions and their host rock, and divided them into pre-, syn-, and post-kinematic categories with respect to specific rock fabrics (Figure 8). Figures S5 and S6 in Supporting Information S1 show examples of field relationships for the Indecision Creek and GSSZs, respectively. The pre-kinematic variety is represented by dikes and plutons that were emplaced prior to deformation and metamorphism, and thus provide a lower (older) limit on subsequent events. Syn-kinematic intrusions, where dikes both cut foliation planes and are tightly folded within them, were especially useful for dating deformation events. Undeformed, post-kinematic dikes were emplaced after deformation and metamorphism, thus placing a upper (younger) age limit on events. This approach allowed us to bracket the ages of rock fabrics and trace their evolution between fjords. Once this framework was established, we compared the new U-Pb dates with published ages to determine the spatial extent and duration of six Early Cretaceous tectonic events (Figures 9 and 10).

Figure 8a shows an example of how U-Pb zircon data collected using this approach allowed us to define an early period (139–130 Ma) of magmatism, deformation, and metamorphism across the Indecision Creek shear zone and distinguish its components spatially. The data show that deformation localized within the shear zone shortly after pluton emplacement began in the mid-crust of the outboard arc (Figure 8a). Dike emplacement continued during this period and was synchronous with shear zone deformation (Figure 8a, locations 2 and 6), with the magmatism affecting a larger area than the deformation. Amphibolite-facies metamorphism accompanied the

Tectonics
10.1029/2021TC007097

Table 2
Summary of U-Pb Zircon Dates and Associated Temperatures From This Study.

Sample	Unit[a]	Map No[b]	Strain zone	Description	Event	Date (Ma)	Error (2SD, Ma)	MSWD	# of zircons[c]	Temp[d] (°C)	SD (1s)	Instrument	Interpretation of Ages	Plot (Figure S7 in Supporting Information S1)
Northern Fiordland (Indecision Creek Shear Zone in Milford Sound region)														
18MS01 A	Dike in Darran Leucogabbro	3	High	Late syn-D1 pegmatite dike	D1	131.1	1.3	0.9	7	694	34	SHRIMP-RG	Age of dike	S7-2
18MS01D	Darran Leucogabbro	3	High	Deformed hb-pl gneiss	D1	134.8	1.4	1.3	4	805	56	SHRIMP-RG	Igneous crystallization age	S7-1
18MS03 A	Darran Leucogabbro	4	Low	Undeformed host rock	D1	133.9	0.9	2.5	5	811	28	SHRIMP-RG	Igneous crystallization age	S7-3
18MS03 B	Dike in Darran Leucogabbro	4	Low	Undeformed dike	D1	130.3	1.2	1.6	9	680	28	SHRIMP-RG	Igneous crystallization age	S7-4
18MS05A-cores	Selwyn Gneiss	5	High	Sheared dike	D1	146.5	0.8	2.0	8	702	23	SHRIMP-RG	Igneous crystallization age	S7-5
18MS05A-rims	Selwyn Gneiss	5	High	Sheared dike	D2	128.0	1.0	1.2	5	664	40	SHRIMP-RG	Syn-D_2 metamorphic age	S7-5
18MS06	Selwyn Gneiss	6	High	Sheared dike	D1	138.8	1.0	2.2	5	665	16	SHRIMP-RG	Syn-D_1 metamorphic age	S57-6
15NZ60-cores	Selwyn Gneiss	2	High	Sheared dike	D1	179.2	1.2	2.2	10	722	56	SHRIMP-RG	Igneous crystallization age	S7-10
15NZ60-rims	Selwyn Gneiss	2	High	Sheared dike	D1	135.0	2.1	1.7	4	732	92	SHRIMP-RG	Syn-D_1 metamorphic age	S7-10
18MS505 A	Harrison Gneiss	8	High	Sheared host	D1	180.5	1.5	0.5	5	780	53	SHRIMP-RG	Igneous crystallization age	S7-7
15NZ58-cores	Harrison Gneiss	1	High	Sheared dike	D1	146.5	1.4	0.7	5	775	26	SHRIMP-RG	Igneous crystallization age	S7-9
15NZ58-rims	Harrison Gneiss	1	High	Sheared dike	D1	131.3	1.3	7.8	3	723	67	SHRIMP-RG	Syn-D_1 metamorphic age	S7-9
05NZ12P	Pembroke Granulite	30	Low	Dioritic granulite gneiss	D2/D3	126.5	2.7	0.9	5	667	13	SHRIMP-RG	Syn-D_2 granulite metamorphism	S7-11
15NZ66	Devil's Arm Chair	7	Low	Undeformed felsic dike	D1	139.5	1.1	2.5	12	725	22	SHRIMP-RG	Intruded outside D_1 shear zone	S7-12
15NZ69	Mt. Edgar Diorite	9	High	Deformed dike	Pre-D1	232.1	4.5	2.3	5	702	22	SHRIMP-RG	Igneous protolith in D_2 shear zone	S7-13
18MS22 A	Dike in Harrison Gneiss	31	High	Late syn-D_5 dike	D5	114.7	1.8	0.9	4	694	50	SHRIMP-RG	Syn-D_5 igneous age	S7-29
18MS25 A	Milford Gneiss	10	High	Host rock	Pre-D1	234.1	3.6	0.7	6	761	28	SHRIMP-RG	Igneous protolith in D_2 shear zone	S7-8
18MS25 B	Dike in Milford Gneiss	10	High	Undeformed dike	D6	80.7	0.9	1.1	4	792	34	SHRIMP-RG	Post-tectonic dike in D_2 shear zone	S7-14
Northern Fiordland (George Sound Shear Zone in George Sound and Bligh Sound)														

Tectonics
10.1029/2021TC007097

Table 2
Continued

Sample	Unit[a]	Map No[b]	Strain zone	Description	Event	Date (Ma)	Error (2SD, Ma)	MSWD	# of zircons[c]	Temp[d] (°C)	SD (1s)	Instrument	Interpretation of Ages	Plot (Figure S7 in Supporting Information S1)
18BS46 C	Western Worsley Pluton	34	High	Two pyroxene orthogneiss	D3	122.1	0.6	2.2	32	n.d.	n.d.	LA-SF-ICPMS	Igneous crystallization age	S7-37
18BS520 G	Western Worsley Pluton	35	High	Two pyroxene orthogneiss	D3	122.4	0.6	1.0	26	n.d.	n.d.	LA-SF-ICPMS	Igneous crystallization age	S7-41
18BS46D	Dike in Worsley Pluton	34	High	Undeformed dike	D6	103.8	3.8	1.3	5	667	62	SHRIMP-RG	Igneous crystallization age	S7-15
18GS538	Eastern McKerr Intrusives	18	Low	Weakly foliated granite	D3	125.0	1.1	1.1	4	790	51	SHRIMP-RG	Igneous crystallization age	S7-19
18BS523c	Metasedimentary gneiss	64	High	Raft inside Worsley pluton	D4	119.4	1.8	2.6	9	n.d.	n.d.	LA-SF-ICPMS	Age of peak metamorphism	S11
18GS545	Eastern McKerr Intrusives	36	Low	Weakly foliated granite	D3	121.3	0.9	1.4	6	819	86	SHRIMP-RG	Igneous crystallization age	S7-20
18GS120 B	Eastern McKerr Intrusives	37	High	Weakly foliated pluton	D4	119.0	0.7	1.5	23	n.d.	n.d.	LA-SF-ICPMS	Igneous crystallization age	S7-38
18GS122A	Dike in E. McKerr Intrusives	38	High	Undeformed dike	D6	107.5	0.6	1.7	23	n.d.	n.d.	LA-SF-ICPMS	Igneous crystallization age	S7-39
18GS129B	Dike in E. McKerr Intrusives	39	High	Late syn-D_4 dike	D4	119.5	2.3	1.2	7	696	69	SHRIMP-RG	Igneous crystallization age	S7-16
18GS129D	Dike in E. McKerr Intrusives	39	High	Folded syn-D_5 dike	D5	115.6	1.9	2.7	8	762	78	SHRIMP-RG	Igneous crystallization age	S7-17
18GS129E	Dike in E. McKerr Intrusives	39	High	Undeformed dike	D6	107.7	1.5	1.7	5	759	18	SHRIMP-RG	Igneous crystallization age	S7-18
18GS127A-cores	Expedition pluton	19	Low	Variably deformed pluton	Pre-D1	310.9	2.2	1.8	12	n.d.	n.d.	LA-SF-ICPMS	Igneous protolith age	S7-40
18GS127A-rims	Expedition pluton	19	Low	Variably deformed pluton	D3	122.7	1.2	1.9	8	n.d.	n.d.	LA-SF-ICPMS	Age of metamorphism	S7-40
15NZ07C	George Sound Paragneiss	40	High	Metasedimentary screen	D3	120.6	2.3	2.4	2	~782	50	SHRIMP-RG	Age of metamorphism	S7-30
15NZ11	George Sound Paragneiss	41	High	Metasedimentary screen	D3	121.3	1.2	1.4	4	734	16	SHRIMP-RG	Age of metamorphism	S7-31
15NZ13	George Sound Paragneiss	41	High	Metasedimentary screen	D4	116.2	2.0	0.8	8	661	9	SHRIMP-RG	Age of metamorphism	S7-34

Tectonics
10.1029/2021TC007097

Table 2
Continued

Sample	Unit[a]	Map No[b]	Strain zone	Description	Event	Date (Ma)	Error (2SD, Ma)	MSWD	# of zircons[c]	Temp[d] (°C)	SD (1s)	Instrument	Interpretation of Ages	Plot (Figure S7 in Supporting Information S1)
15NZ15	George Sound Paragneiss	42	High	Metasedimentary screen	D5	113.7	2.1	0.2	5	784	10	SHRIMP-RG	Age of metamorphism	S7-33
15NZ22	Bligh Sound paragneiss	43	High	Metasedimentary screen	D4	120.1	1.0	1.9	6	790	27	SHRIMP-RG	Age of metamorphism	S7-35
15NZ24B	Bligh Sound paragneiss	44	High	Metasedimentary screen	D4	120.1	2.0	0.7	5	712	77	SHRIMP-RG	Age of metamorphism	S7-36
Central Fiordland (Indecision Creek Shear Zone in Lake Te Anau region)														
18WA554A	Indecision Creek Complex	11	High	Deformed syn-D_2 dike	D2	127.5	1.0	0.9	6	784	52	SHRIMP-RG		S7-21
18WA559A	Indecision Creek Complex	12	High	Deformed dike	D2	124.4	1.2	1.8	8	638	12	SHRIMP-RG		S7-22
18WA560A	Indecision Creek Complex	13	High	Deformed dike	D2	126.7	1.7	2.4	9	659	41	SHRIMP-RG		S7-23
18WA560B	Indecision Creek Complex	13	High	Deformed syn-D_1 dike	D1	132.3	1.5	1.2	8	700	38	SHRIMP-RG	Igneous crystallization age	S7-24
18WA560C	Indecision Creek Complex	13	High	Cross-cutting dike	D2	126.4	1.7	2.2	7	639	39	SHRIMP-RG		S7-25
18WA568	Mt. Anau Complex	14	Low	Weakly foliated dike	D1	137.5	1.6	1.4	8	823	29	SHRIMP-RG	Igneous crystallization age	S7-26
18WA570	Mt. Anau Complex	15	Low	Weakly foliated dike	D1	138.4	1.4	2.1	7	744	26	SHRIMP-RG	Igneous crystallization age	S7-27
18WA573	Darran Leucogabbro	16	Low	Weakly foliation pluton		n.d.	n.d.	n.d.	n.d.	727	91	SHRIMP-RG		n.d.
18NF585	North Fiord pluton	17	Low	Undeformed pluton	D3	124.8	1.6	1.0	6	661	19	SHRIMP-RG	Igneous crystallization age	S7-28
Central Fiordland (Myth Tarn and Mary Peaks)														
19MT5	Misty Pluton	49	High	Foliated hornblende diorite		93.0	1.1	2.4	4	n.d.	n.d.	LA-SF-ICPMS	Age of fluid infiltration	S7-42
19MT10B	Large Pluton	20	High	Deformed (L-tectonite) pluton	Pre-D1	316.0	3.2	1.5	17	n.d.	n.d.	LA-SF-ICPMS	Pluton crystallization age	S7-43
19MP19B[e]	Large Pluton	21	High	Mylonite within the pluton	Pre-D1	307.5	3.2	3.6	4	n.d.	n.d.	LA-SF-ICPMS	Age of protolith	S7-44
19MP19B[f]	Large Pluton	21	High	Mylonite within the pluton	D4	117.6	0.8	3.7	11	n.d.	n.d.	LA-SF-ICPMS	Age of deformation	S7-44

Tectonics
10.1029/2021TC007097

Table 2
Continued

Sample	Unit[a]	Map No[b]	Strain zone	Description	Event	Date (Ma)	Error (2SD, Ma)	MSWD	# of zircons[c]	Temp[d] (°C)	SD (1s)	Instrument	Interpretation of Ages	Plot (Figure S7 in Supporting Information S1)
19MP20A	undeformed dike in Large Pluton	50	High	Dike cuts foliated pluton	D4	117.1	0.9	3.9	8	n.d.	n.d.	LA-SF-ICPMS	Age of metamorphism	S7-45
19MP26	undeformed dike in Large Pluton	51	High	Dike cuts foliated pluton	D6	100.7	0.5	3.7	18	n.d.	n.d.	LA-SF-ICPMS	Age of metamorphism	S7-46
19MP30[e]	undeformed dike in Large Pluton	22	High	Dike cuts foliated pluton	Pre-D1	318.8	2.1	3.4	10	n.d.	n.d.	LA-SF-ICPMS	Igneous crystallization age	S7-47
19MP30[f]	undeformed dike in Large Pluton	22	High	Dike cuts foliated pluton	D5	115.9	1.2	2.3	5	n.d.	n.d.	LA-SF-ICPMS	Age of metamorphism	S7-47
19MP31C[e]	undeformed dike in Large Pluton	23	High	Dike cuts foliated pluton	Pre-D1	319.4	3.6	1.2	12	n.d.	n.d.	LA-SF-ICPMS	Igneous crystallization age	S7-48
19MP31C[f]	undeformed dike in Large Pluton	23	High	Dike cuts foliated pluton	D5	113.6	2.2	1.2	4	n.d.	n.d.	LA-SF-ICPMS	Age of metamorphism	S7-48
19MP34[e]	undeformed dike in Large Pluton	24	High	Dike cuts foliated pluton	Pre-D1	317.7	4.4	1.1	8	n.d.	n.d.	LA-SF-ICPMS	Igneous crystallization age	S7-49
19MP34[f]	undeformed dike in Large Pluton	24	High	Dike cuts foliated pluton	D6	100.9	2.2	1.5	4	n.d.	n.d.	LA-SF-ICPMS	Age of metamorphism	S7-49
19MP37C	Lake Hankinson Complex	52	Low	Migmatitic orthogneiss	D4	117.0	0.9	1.4	25	n.d.	n.d.	LA-SF-ICPMS	Age of partial melting	S7-50
Central Fiordland (Lake Roxburgh)														
19LR52C	Lake Hankinson Complex	25	High	Granitic migmatitic gneiss	Pre-D1	363.0	1.8	2.3	14	n.d.	n.d.	LA-SF-ICPMS	Age of metamorphism	S7-51
19LR70B	Indecision Creek Complex	54	High	Faulted hornblende diorite	Fault	39.8	0.4	1.3	8	n.d.	n.d.	LA-SF-ICPMS	Fluid infiltration during faulting	S7-52
19LR72[e]	Lake Roxburgh tonalite	26	Low	Undeformed biotite granite	Pre-D1	290.1	1.6	5.3	18	n.d.	n.d.	LA-SF-ICPMS	Age of fluid infiltration	S7-53
19LR72[f]	Lake Roxburgh tonalite	26	Low	Undeformed biotite granite	D6	95.8	1.0	2.2	3	n.d.	n.d.	LA-SF-ICPMS	Age of fluid infiltration	S7-53
19LR73	Lake Roxburgh tonalite	27	Low	Undeformed biotite granite	Pre-D1	276.3	1.6	3.0	44	n.d.	n.d.	LA-SF-ICPMS	Age of fluid infiltration	S7-54

Tectonics

10.1029/2021TC007097

Table 2
Continued

Sample	Unit[a]	Map No[b]	Strain zone	Description	Event	Date (Ma)	Error (2SD, Ma)	MSWD	# of zircons[c]	Temp[d] (°C)	SD (1s)	Instrument	Interpretation of Ages	Plot (Figure S7 in Supporting Information S1)
19LR75	Lake Roxburgh tonalite	28	Low	Weakly foliated granite	Pre-D1	272.4	2.0	3.8	32	n.d.	n.d.	LA-SF-ICPMS	Age of fluid infiltration	S7-55
Central Fiordland (Henderson Burn)														
19HB80	Eastern Worsley Pluton	55	Low	Undeformed host	D5	111.8	0.6	1.8	41	n.d.	n.d.	LA-SF-ICPMS	Pluton crystallization age	S7-56
19HB84	Eastern Worsley Pluton	56	Low	Undeformed host	D5	115.1	0.6	2.4	49	n.d.	n.d.	LA-SF-ICPMS	Pluton crystallization age	S7-57
19HB89A	Eastern Worsley Pluton	57	Low	Undeformed host	D5	115.6	0.6	1.7	47	n.d.	n.d.	LA-SF-ICPMS	Pluton crystallization age	S7-58
18DS39	Supper Cove Pluton	61	Low	Undeformed host	D3	124.8	0.6	2.1	36	n.d.	n.d.	LA-SF-ICPMS	Pluton crystallization age	S7-59
18DS40	Supper Cove Pluton	62	Low	Undeformed host	D3	124.2	0.8	2.3	19	n.d.	n.d.	LA-SF-ICPMS	Pluton crystallization age	S7-60
18DS41A	Supper Cove Pluton	63	Low	Undeformed host	D3	121.5	0.6	2.5	39	n.d.	n.d.	LA-SF-ICPMS	Pluton crystallization age	S7-61
18WJ20-cores	Deep Cove Gneiss	65	Low	Foliated pluton	Pre-D1	359.7	3.7	3.6	9	n.d.	n.d.	LA-SF-ICPMS	Pluton crystallization age	S7-62
18WJ20-rims	Deep Cove Gneiss	65	Low	Foliated pluton	D5 or D6	111.5	1.8	3.4	5	n.d.	n.d.	LA-SF-ICPMS	Age of metamorphism	S7-62
18WJ21	Deep Cove Gneiss	66	Low	Foliated pluton	Pre-D1	344.6	1.8	2.4	29	n.d.	n.d.	LA-SF-ICPMS	Pluton crystallization age	S7-63

Note. Complete isotopic data and individual spot dates are in Tables S2 and S3. Please see Tables S2 and S3 for information on sample location coordinates, archive information, and IGSN and Petlab databases. Location coordinates reported in New Zealand Transverse Mercator 2000 projection, horizontal datum NZGD2000. Location of sample 05NZ12P is from Stowell et al. (2010). SHRIMP-RG, Sensitive High Resolution Ion Microprobe—Reverse Geometry; LA-SF-ICPMS, Laser Ablation—Sector Field—Inductively Coupled Plasma Mass Spectrometry.

[a]Unit name following I. M. Turnbull et al. (2010). [b]Numbers refer to sample locations plotted on maps in Figures 9 and 10. [c]Zircons used in age calculations. [d]Zircon temperatures calculated from Ti concentrations following Ferry and Watson (2007) thermometer. [e]Older population. [f]Younger population.

Tectonics

10.1029/2021TC007097

Table 3

Summary of U-Pb Laser Ablation Split Stream Titanite Dates and Associated Temperatures.

Sample	Unit[a]	Map number[b]	Strain zone	Description	Event	Date (Ma)	Error (2SD; Ma)	MSWD	# of titanites[c]	Temperature[d] (°C)	SD (1s)	Instrument	Plot (Figure S8 in Supporting Information S1)
Northern Fiordland (Indecision Creek Shear Zone and George Sound shear zones)													
15NZ15	George Sound metasediment	42	High	Metasedimentary screen	D6	95.0	1.3	1.6	89	717	45	UCSB LASS	S8-A
P77080	Eastern McKerr Intrusives	46	Low	Weakly foliated hb diorite	D5	112.4	1.8	1.7	49	762	50	UCSB LASS	S8-N
15NZ22	Bligh Sound metasediment	43	High	Metasedimentary screen	D6	108.2	15.2	0.4	32	753	50	UCSB LASS	S8-B
15NZ24b	Bligh Sound metasediment	44	High	Metasedimentary screen	D6	105.7	0.9	5.4	96	908	46	UCSB LASS	S8-C
P76610	Western Worsely Pluton	47	High	Garnet-bearing diorite	D3	125.8	1.8	1.3	49	764	50	UCSB LASS	S8-O
18GS117c	George Sound metasediment	45	High	Mica-rich shear zone	D6	106.9	2.2	1.1	47	746	23	UCSB LASS	S8-D
18GS129c	George Sound metasediment	39	High	Amphibolite	D6	103.6	6.9	0.6	49	734	11	UCSB LASS	S8-E
18MS01 B	Darren Leucogabbro	4	High	Mylonite	D5	115.8	7.0	1.4	30	741	34	UCSB LASS	S8-P
18TT140 A	Two Thumbs metasediment	48	High	Calcareous gneiss	D5	111.8	0.9	6.9	49	711	44	UCSB LASS	S8-J
Central Fiordland (Indecision Creek Shear Zone in Lake Te Anau region)													
18WA151	Indecision Creek Complex	32	High	Foliated granite	D4	117.7	1.7	1.1	33	686	24	UCSB LASS	S8-K
18WA153	Indecision Creek Complex	33	High	Biotite granite gneiss	D4	120.1	2.1	1.4	50	731	9	UCSB LASS	S8-L
18WA165 A	Mt. Anau Complex	29	Low	Weakly foliated host	D3	124.5	1.6	0.9	47	679	41	UCSB LASS	S8-M
Central Fiordland (Henderson Burn and Mary Peaks)													
19HB77 A	Eastern Worsley Pluton	58	Low	Undeformed host	D5	111.8	1.3	2.1	50	707	9	UCSB LASS	S8-F
19HB80	Eastern Worsley Pluton	55	Low	Undeformed host	D5	113.4	0.7	3.8	50	706	22	UCSB LASS	S8-G
19HB85 t	Eastern Worsley Pluton	59	Low	Undeformed host	D5	117.5	0.5	1.6	49	729	3	UCSB LASS	S8-H
19HB87	Eastern Worsley Pluton	60	Low	Undeformed host	D5	114.0	0.6	1.3	50	746	5	UCSB LASS	S8-I
19MP15	Misty Pluton	53	Low	Foliated host	D4	n.d.	n.d.	n.d.	n.d.	691	45	UCSB LASS	n.d.

Note. Complete isotopic data and individual spot dates are in Table S5. Please see Table S5 for information on sample location coordinates, archive information, and IGSN and Petlab databases. Location coordinates reported in New Zealand Transverse Mercator 2000 projection, horizontal datum NZGD2000.

[a]Unit name following I. M. Turnbull et al. (2010) and R. Turnbull et al. (2010). [b]Number used to identify samples plotted in Figures 9 and 10. [c]Titanite used in age calculations. [d]Titanite temperatures calculated from Zr concentrations following Hayden et al. (2008) thermometer.

magmatism but penetrated much farther west into the lower crustal block than the zone of deformation, forming a large thermal aureole (see Section 4.2.1 for further discussion). The stitching dikes and shared history of metamorphism on both sides of the shear zone show that the outboard arc must have been in contact with the Gondwana margin before the onset of D_1 deformation (see also Schwartz et al. (2021)). Figure 8b shows how superposed deformations in the same shear zone were distinguished using a variety of ages obtained from variably deformed dikes (see Sections 4.2.1 and 4.2.5 for further discussion).

Rare earth element data (Table S4) and mineral textures that distinguish magmatic zircon from those that (re) crystallized during deformation and/or metamorphism are now well documented in Fiordland (Hollis et al., 2003, 2004; Klepeis et al., 2016; Schwartz et al., 2016, 2017; Scott et al., 2009; Stowell et al., 2010, 2014, 2017; Tulloch et al., 2011). For example, zircons from the WFO (e.g., sample 18WJ20, Table 2, Figure S9 in Supporting Information S1) typically show weak oscillatory or sector zoning with irregular external appearances, consistent with late-stage igneous growth and/or very slow crystallization during prolonged residence in the lower crust (Schwartz et al., 2016). Metamorphic zircons commonly display embayment and truncation of growth zoning suggesting resorption during high-grade metamorphism and/or rims around weak oscillatory zoning textures (Figure S9 in Supporting Information S1). An examination of chondrite-normalized rare earth elements in zircon from samples of garnet-bearing orthogneiss also typically show a flattening of HREEs, which is consistent with growth in equilibrium with metamorphic garnet (e.g., compare samples 1241 and 1304b in Klepeis et al., 2016). High U/Th ratios (>10) helped us distinguish zircon that either grew in the presence of water during amphibolite-facies metamorphism or crystallized in a fluid-rich magma system (e.g., samples 19MP31C, 19MP34; Figure S10 in Supporting Information S1). The dating of metamorphic mineral assemblages using Sm-Nd garnet geochronology and their comparison with zircon ages (Stowell et al., 2010, 2014, 2017, 2021) also assisted interpretations. For example, some Sm-Nd garnet dates appear to record cooling after peak metamorphism due to differences in the diffusion rates of Nd in garnet compared to Pb in zircon (Stowell et al., 2021). Last, a comparison of zircon ages from metamorphic aureoles with igneous crystallization ages from the adjacent plutons also helped us distinguish igneous and metamorphic ages (Figure 8a).

For titanite, we used the criteria described by Schwartz et al. (2016), Buriticá et al. (2019), and Blatchford et al. (2020) to interpret magmatic and metamorphic dates. This work shows that titanites from Fiordland's high-grade metamorphic rocks record the timing and conditions of metamorphism rather than cooling (see Schwartz et al. (2016) for discussion of titanite closure temperatures and Pb mobility). In most cases, titanites from the high-grade metamorphic rocks we sampled lack metamorphic rims (Figure S12 in Supporting Information S1) and most analyses lie along a single isochron array that defines the timing of their formation (Figure S6 in Supporting Information S1). Only in rare cases do metamorphic titanites show evidence of multiple metamorphic growth events (Figure S14 in Supporting Information S1). Titanites were linked to specific igneous and metamorphic fabrics using both cathodoluminescence (Figure S12 in Supporting Information S1) and thin section (Figure S13 in Supporting Information S1) textures, and by comparisons with igneous and metamorphic zircon ages from the same samples (additional details in Text S2 in Supporting Information S1). Figure 8b, and other examples discussed in Text S2 in Supporting Information S1, illustrate how a comparison of new magmatic and metamorphic titanite and zircon ages with published zircon and garnet (Sm-Nd) dates helped us distinguish the ages of superposed fabrics, including tectonic events that were difficult to identify using U-Pb zircon geochronology alone. For example, the igneous crystallization ages of swarms of zircon-poor pegmatite dikes that were emplaced into the Grebe-IC and GSSZs after deformation had ceased (blue stars, Figure 10) were determined mainly using titanite geochronology (Table 3). This result shows that both shear zones continued to act as conduits for magma after subduction and regional contraction had stopped.

3.2.2. Analytical Methods

U-Pb isotopes (Tables S2 and S3) and trace element data (Ti, Fe, Y, nine rare earth elements, U, Th) (Table S4) in zircon were collected by secondary ion mass spectrometry using the Stanford–U.S. Geological Survey sensitive high-resolution ion microprobe–reverse geometry (SHRIMP-RG) facility and by laser-ablation–sector field–inductively coupled plasma–mass spectrometry (LA-SF-ICPMS) at California State University-Northridge following methods described by Schwartz et al. (2017), Coble et al. (2018), and Buriticá et al. (2019). Rims and cores imaged by cathodoluminescence (Figure S9 in Supporting Information S1) were targeted for analysis. Textural complexities were evaluated using rim-core-rim traverses (Figure S11 in Supporting Information S1). Spots with high common Pb were excluded. In cases where one or two grains of a zircon population were older than the majority, the older

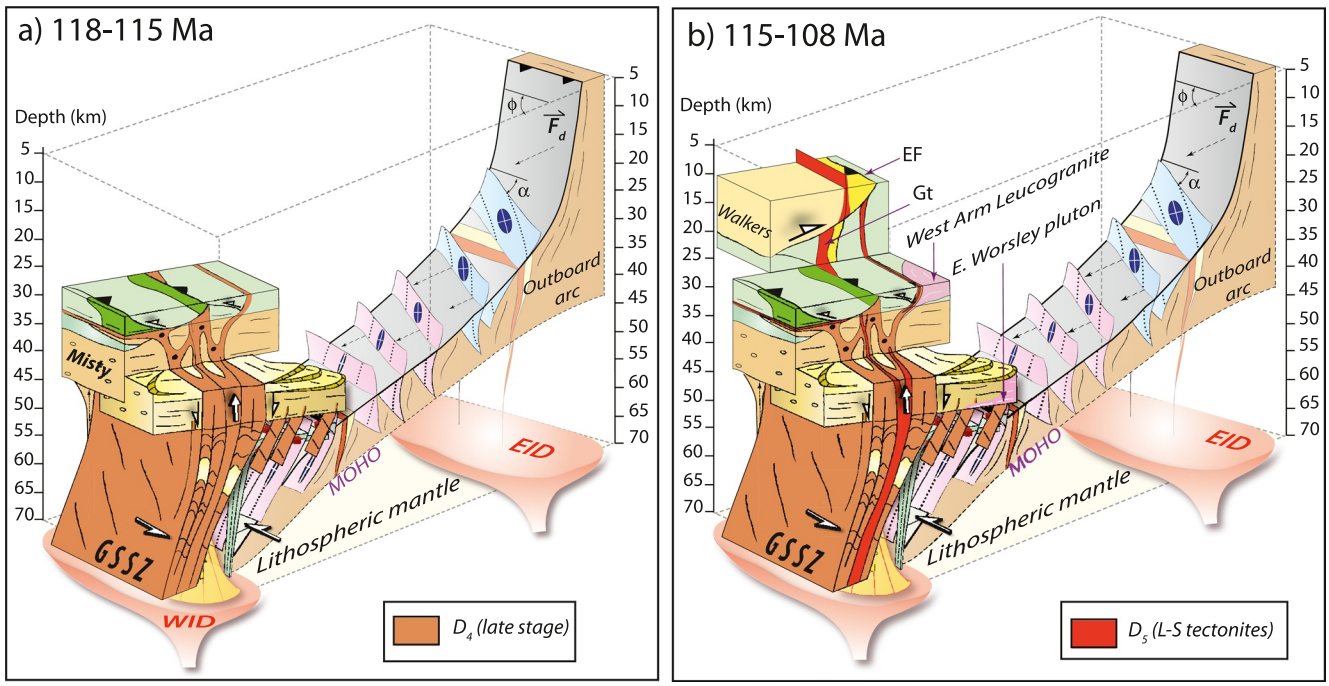

Figure 13. Model of transpressional shear zone growth within the Median Batholith from 118 to 108 Ma. (a) D_4 deformation (late stage) propagates upwards across Misty pluton after its emplacement. (b) High-strain zones (D_5) spread laterally and upward into middle and upper crust as Misty pluton solidifies and the West Arm Leucogranite and Eastern Worsley pluton are emplaced. Gt, Gutter shear zone; EF, Escarpment fault; Walkers, Walkers pluton on Stewart Is., EID, Eastern Isotopic Domain. D_4 and D_5 reactivations of the Grebe-ICSZ have been omitted for clarity.

ages were interpreted to represent inheritance (e.g., sample 19MP37C, Figure S7-50 in Supporting Information S1). Spots with large uncertainties and statistically young ages were excluded from analyses because they likely represent Pb loss (e.g., sample 19MT10B, Figure S7-43 in Supporting Information S1; Sample 18BS523c, Figure S11 in Supporting Information S1). Differences in Th and U concentrations among grains (Figure S10 in Supporting Information S1) support this interpretation. Results are presented as error-weighted average ages calculated from the common Pb–corrected $^{207}Pb/^{206}Pb$ and $^{238}U/^{206}Pb$ data. Total uncertainties of 2σ are in Table 2. Zircon data plots (Figures S7 and S11 in Supporting Information S1), data tables (Tables S2, S3 and S4), and additional details (Text S2 in Supporting Information S1) of methods (Black et al., 2004; Mattinson, 2010; Stacey and Kramers, 1975; Tera and Wasserburg, 1972; Vermeesch, 2018) are in Supporting Information S1.

For titanite, $^{206}Pb/^{238}U$ isotopes, geochemistry (La, Sm, Yb, U, Th), and Zr-in-titanite temperatures (Table 3) were collected using laser-ablation–split-stream–inductively coupled plasma–mass spectrometry at the University of California Santa Barbara following methods outlined in Kylander-Clark et al. (2013), Schwartz et al. (2016), and Buriticá et al. (2019). Between 30 and 96 grains per sample were picked and analyzed. The data were corrected for common Pb using a regression on the Tera-Wasserburg Pb/U isochron following methods discussed in Buriticá et al. (2019). Titanite data plots (Figure S8 in Supporting Information S1), data tables (Tables S5 and S6) and additional details (Fiugres S12, S13 and S14 in Supporting Information S1) are provided. All dates are assigned 2% uncertainties based on reproducibility of standards during analyses (after Buriticá et al., 2019).

3.3. Kinematics

Sense of shear indicators in the Grebe-IC and GSSZs are abundant and described elsewhere (Allibone & Tulloch, 2008; Blatchford et al., 2020; N. R. Daczko et al., 2001; Daczko et al., 2002c; Daczko et al., 2002b; Klepeis & King, 2009; Klepeis et al., 2004; Marcotte et al., 2005; McGinn et al., 2020; Scott et al., 2011, 2014). We used the results of kinematic analyses cited in these publications, which follow excepted methods of shear zone analysis (e.g., Díaz-Azpiroz et al. (2019).

4. Crustal Structure

4.1. Compositional Boundaries and Crustal Thickness

An examination of rock composition by depth (Figure 6) shows that three boundaries vertically stratified the crust during the Early Cretaceous. These include the Moho and the top and base of the WFO, which makes up ∼54% of all assemblages in the western block and is dominated by pyroxene and hornblende diorite. The top of the batholith corresponds to paleodepths of 24–29 km, its base occurs at 45–47 km (Figures 4 and 7). Above, the crust is mainly felsic, below it is mainly mafic (Figure 6), similar to other continental arcs (Klein & Jagoutz, 2021). Beneath ∼55 km, the crust transitions downward into plagioclase-poor, mafic-ultramafic rocks rich in clinopyroxene and garnet (Chapman et al., 2015; Clarke et al., 2013; Cyprych et al., 2017; De Paoli et al., 2009, 2012; Stowell et al., 2017). Layers of eclogite, clinopyroxenite, harzburgite and hornblende peridotite in the Breaksea Orthogneiss (Figures 4 and 7) record Early Cretaceous metamorphism at 1.8 GPa (De Paoli et al., 2009; Stowell et al., 2017), suggesting the crust there was ∼65 km thick (Figures 6 and 7). However, by ∼118 Ma, crustal decompressed to 1.2 GPa (Table 1), suggests that much of Fiordland was closer to 45–50 km thick at that time (Figure 4) (see also Brackman & Schwartz, 2022).

Fiordland also exhibits three vertical boundaries (Figure 7) of Carboniferous origin. The eastern boundary coincides with the Grebe-IC shear zone and marks the late Paleozoic edge of Gondwana (Figure 3b; Allibone & Craw, 2016; Allibone, Jongens, Turnbull, et al., 2009; Marcotte et al., 2005; McCoy-West et al., 2014; Scott et al., 2011; Turnbull et al., 2021). To the west, linear belts of late Carboniferous plutons and high-strain zones define two other boundaries (Ramezani & Tulloch, 2009; Klepeis, Webb, Blatchford, Schwartz, et al., 2019, Klepeis, Webb, Blatchford, Jongens, et al., 2019): the George Sound (GSSZ) and Straight River (SRSZ) shear zones (Figures 4 and 7). The great depth of exposure and the alignment of Cretaceous magma centers along these structures (Figures 9 and 10) suggest that all three transect the crust and penetrate the lithospheric mantle. Turnbull et al. (2021) and Schwartz et al. (2021) showed that two separate isotope domains in the lithospheric mantle (Figure 7) that pre-date Early Cretaceous transpression.

New U-Pb zircon ages help define the pre-Mesozoic histories of these regions. The Large and Expedition plutons (Figure 9), both of which intruded the central boundary, yielded 319–307 Ma dates (Table 2). Cretaceous thermal disturbance and Pb loss complicate the crystallization ages. However, the Carboniferous dates match published protolith ages for both plutons (Allibone, Jongens, Scott, et al., 2009; Ramezani & Tulloch, 2009). The Large pluton also appears to record both Carboniferous and Cretaceous deformation. At its west end, a band of Cretaceous mylonite cuts an older L-tectonite fabric. Undeformed dikes that cut the older fabric produced a dominant late Carboniferous zircon population and a smaller Cretaceous one (Table 2). High U/Th ratios and metamorphic rims on zircon from the Large pluton suggest that the oldest population represents igneous crystallization at 319–317 Ma and the youngest reflects Cretaceous metamorphism and Pb loss (U/Th plot in Figure S10 in Supporting Information S1) during emplacement of the 117–114 Ma Misty pluton. A shared foliation between the Large and Misty plutons suggests that Cretaceous deformation accompanied the metamorphism, a conclusion also reached by Blatchford et al. (2020) for the Misty and Cozette plutons (Figure 9).

The reactivation of an originally Carboniferous structure also characterizes the eastern shear zone system. The upper crustal Freshwater Fault first formed as a Paleozoic extensional fault and later reactivated during Cretaceous transpression (Allibone & Craw, 2016). A late Carboniferous mylonite in the mid-crust of the Grebe-IC shear zone (Buriticá et al., 2019) is similar in age and style to that we found in the central boundary. In addition, Devonian (∼363 Ma) and Permian (290–274 Ma) ages (e.g., Lake Roxburgh tonalite, Table 2) suggest that magma and/or fluid infiltrated the boundary occurred as plutons were emplaced in the outboard arc (Allibone, Milan, et al., 2009; Mortimer, Gans, et al., 1999). These events illustrate how these late Paleozoic boundaries became sites of repeated deformation and magma/fluid transfer after they formed.

4.2. Grebe-Indecision Creek Shear Zone System

The Grebe-IC shear zone system extends ∼330 km through Fiordland to Stewart Island (Figure 3b) and records six stages of Cretaceous tectonic activity (Figures 9 and 10). Only a small volume of magma was emplaced into it during the 136–106 Ma interval, making the system magma-poor for this period. Still, most areas record the emplacement of small dikes, which aided our ability to date features (Figure 8, Figure S5 in Supporting Information S1). For example, the ∼127 Ma Refrigerator (Buriticá et al., 2019) and the 123–120 Ma Puteketeke (Buriticá

et al., 2019; Ramezani & Tulloch, 2009; Scott & Palin, 2008) plutons (Figures 9 and 10) partially intruded the shear zone but are small relative to those in the western system.

4.2.1. D_1 Deformation

The oldest stage of Mesozoic deformation (D_1) formed a 4 km-wide high-strain zone between a mid-crustal block to the east (the outboard arc) and a lower crustal block to the west (Gondwana) in northern Fiordland (Figures 5 and 9). At Milford Sound, the mid-crustal block preserves a series of upper amphibolite-facies, mylonitic shear zones up to 5 m thick (Figures S5a and S5b in Supporting Information S1). Most of these dip to the NW (75–85°) and record NW-over-SE reverse motion with minor sinistral shear, recording an oblique underthrusting of the outboard arc below Gondwana (Figure 11).

In the lower crustal block, D_1 formed a subvertical zone of L_1-S_1 fabric focused entirely within the Harrison, Selwyn Creek, and Indecision Creek gneisses (Figure 8a). Although L_1-S_1 is overprinted by younger deformations (Figure 8b), it remains visible in pods wrapped by the younger foliations. Inside these pods, S_1-L_1 is distinguished from older foliations on the basis of its north-striking orientation (Figure 9) and its absolute age.

The age of D_1 in the lower crust is given by U-Pb zircon dates from variably deformed dikes. Zircon dates from sheared host rock and late syn-kinematic dikes (Figure 8a, Figures S5a and S5b in Supporting Information S1) (Table 2) give a 136–130 Ma interval. Similar intrusive relationships and ages from lake Te Anau (Table 2) allowed us to trace this high-strain zone into the middle crustal block (Figure 9).

Zircon dates from the lower crust show that amphibolite-facies metamorphism accompanied D_1 (Figure 8a). Dates from zircon cores expand the published protolith ages of the Harrison (181–146 Ma) and Selwyn Creek gneisses (179–146 Ma) (*cf.* Schwartz et al., 2017) and provide a lower limit for D_1 in the lower crust. Zircon rim dates (137–130 Ma) closely match the ages of 139–130 Ma dikes from inside, west of, and east of the high-strain zone. These relationships show that amphibolite-facies metamorphism accompanied the emplacement of small magma batches into the lower crust during D_1.

West of the D_1 high-strain zone, metamorphism affected most of the lower crustal block near Milford Sound but without the accompanying deformation (Figure 8a). Tulloch et al. (2011), Stowell et al. (2010), and Hollis et al. (2003) showed that high-grade metamorphism and the in-situ partial melting of Paleozoic and Mesozoic host rocks at 136–134 Ma define a region of hot lower crust that was larger than the narrow zone of D_1 deformation (e.g., Figure S11b in Supporting Information S1, grain 5). This metamorphism represents the last in a series of events that accompanied magma emplacement in the outboard arc at 147–136 Ma (Darran suite) (Kimbrough et al., 1994; Muir et al., 1998; Schwartz et al., 2017) and 139–136 Ma (Mt Anau complex) (this study).

In the mid-crust, the oldest part of the Grebe-IC shear zone occurs near South Fiord where bands of amphibolite-facies mylonite up to 3 km wide are spaced a few kilometers apart within a 10 km-wide zone of transpression (Figure 9). Buriticá et al. (2019) inferred a 147–131 Ma age for this deformation using U-Pb titanite dates. This interval matches the one we found for D_1 in the lower crust. Near Lake Manapouri (Figure 9), the shear zone forms a 200–300 m-wide region of north-striking mylonite (Scott et al., 2011), which narrows southward into a 100–200 m band that dips variably to the west (70°–90°) and east (50°–85°).

The upper crustal part of the D_1 system is represented by the Freshwater Fault System (Stewart Is.) where moderately dipping (50°–70°), low to mid greenschist facies brittle-ductile faults record <10 km of south over north reverse motion (Allibone & Tulloch, 2008). This shear sense indicates that shallow parts of the system also initiated as an oblique-reverse fault.

4.2.2. D_2 Deformation

The second stage (D_2) formed a wide zone of NE-striking gneissic foliations (S_2) with NW- and SE-plunging mineral stretching lineations (L_2) that dominates the lower crust near Milford Sound (Figure 9). In low-strain zones, elongate pods preserve older Paleozoic-Mesozoic fabrics and mineral assemblages. In high- to moderate-strain zones, the older fabrics are tightly folded, truncated, and transposed into parallelism with S_2 (Figures S5c and S5d in Supporting Information S1). The L_2-S_2 mineral assemblages (hornblende, garnet, pyroxene, plagioclase) record both amphibolite- and granulite-facies metamorphism accompanied by partial melting (Clarke et al., 2000; N. Daczko et al., 2001; Stowell et al., 2010). Asymmetric shear bands record NW-over-SE reverse displacements

(Figure S5e in Supporting Information S1), indicating continued oblique underthrusting of the outboard arc beneath Gondwana (Figure 11).

A lower limit of ~130 Ma for D_2 in the lower crust is given by the age of deformed syn-D_1 metamorphic mineral assemblages (Figure 8a). Zircon dates from granulite in a low-strain zone at Pembroke Valley (location 18 in Figure 8b) also show that L_2-S_2 developed through ~126 Ma. This latter result is compatible with other zircon and Sm-Nd garnet ages from the same place (Figure 8b), which record granulite-facies metamorphism at 128–126 Ma (Stowell et al., 2010). In addition, D_2 granulite metamorphism records high pressures (1.1–1.4 GPa), which further distinguishes it from lower pressure (>0.6 GPa) metamorphism at 136–134 Ma (Stowell et al., 2010). Last, L_2-S_2 is cut by the 124–121 Ma Western Worsley pluton (Schwartz et al., 2017), indicating a 129–124 Ma age for D_2 (Figure 9).

To track the spatial evolution of D_2, we used plutons and dikes that were emplaced at different depths at 129–124 Ma (Figures 7 and 9). Zircon dates from syn-kinematic dikes (Figures 8a, Figures S5c and S5d in Supporting Information S1) show that D_2 began to develop west of the D_1 zone after ~130 Ma. The ages of these dikes (128–124 Ma) are similar to those obtained by Hollis et al. (2003) and Marcotte et al. (2005), including from the 128.8 ± 2.4 Ma Mt Edgar pluton (Figures 7 and 9). This latter pluton is deformed by D_2 and shows that the deformation front had propagated west of this locality by ~126 Ma. In contrast, the 128–120 Ma Eastern McKerr pluton (Figures 7 and 9) is unaffected by D_2. Because these two plutons are located approximately along the strike of S_2 from one another (Figure 9), but were emplaced at different depths (Figure 7), they show where the deformation front was at ~124 Ma. The lack of D_2 in the Eastern McKerr indicates that the deformation was confined to the lower crust near the Mt Edgar pluton at this time.

The mid-crustal block (lake Te Anau) shows a similar result where D_2 migrated west to George Sound (Figure 9). Plutons located east of the D_1 shear zone are either undeformed (e.g., the ~125 Ma North Fiord pluton) or lack D_2 deformation (an undeformed 126–124 Ma pluton in eastern Worsley Arm) (Tables 2 and 3). In contrast, the deformed Refrigerator pluton records the passage of D_2 west of Lake Manapouri by ~125 Ma (Buriticá et al., 2019). These results show that the western limit of D_2 in the mid-crust forms a broad arc between the southern end of George Sound to Lake Manapouri (Figure 9) where D_2 ended before ~122 Ma (Buriticá et al., 2019). These relationships indicate that the outboard arc continued to be underthrust beneath Gondwana at 129–124 Ma (Figure 11).

4.2.3. D_3 Magmatism

The third stage (D_3) involved minor magmatism without significant deformation at 124–121 Ma (Figure 10). Zircon dates (~124 Ma) from undeformed dikes at Mt. Mitchelson (Figure 9) (Marcotte et al., 2005) and titanite dates from the Mt Anau Complex (Table 3) show that small magma batches were emplaced into the Grebe-IC shear zone after the D_2 front had migrated west. High-grade metamorphism in the lower crustal block also persisted during D_3 magmatism, indicating it remained hot and weak during D_2 (Hollis et al., 2003; Stowell et al., 2010; Tulloch et al., 2011). In the mid-crust, the 123–120 Ma Puteketeke (Figure 10; Buriticá et al., 2019; Ramezani & Tulloch, 2009; Scott & Palin, 2008), Takahe (Buriticá et al., 2019), Titaroa, and North Fiord (Bolhar et al., 2008) plutons (Figure 10) were emplaced. In the upper crust, the Walkers pluton on Stewart Island (Figure 7) was emplaced at 128–120 Ma (Allibone & Tulloch, 2008).

4.2.4. D_4 Deformation

In the mid-crust (15–20 km depth), zones of D_4 deformation remained centered on the late Carboniferous boundary at Gondwana's eastern edge (Figure 10) where they reactivated D_1 shear zones (Figures 9 and 10). These D_4 shear zones record inclined transpression (McGinn et al., 2020) until ~116 Ma (Buriticá et al., 2019). Mineral lineations are down-dip to moderately plunging on steep foliation planes (Buriticá et al., 2019; Scott et al., 2011). Shear sense is dominantly sinistral with a component of west-side-down motion, although dextral motion also is reported (Buriticá et al., 2019; Scott et al., 2011). On Stewart Island, the Gutter shear zone (15–20 km depth) records mostly reverse (south-side-up) displacements with local dextral motion at 120–112 Ma (Allibone & Tulloch, 2008). These variations in shear sense may reflect different contributions of pure and simple shear as well as differences in shear zone orientation.

In the lower crust, D_4 formed tight, upright folds of S_2 and steep, NNE-striking upper amphibolite facies foliations (S_4) (Figures S5f and S5g in Supporting Information S1). At least four of these high-strain zones occur west of the

Grebe-IC (Figure 10). In one of them, the Pembroke thrust deforms 126–120 Ma granulites (Stowell et al., 2010; this study) and records NW-SE shortening at ~55 km depth (Figure 5) (*cf.* N. Daczko et al., 2001; Klepeis & King, 2009). Other zones record NW-SE shortening with sinistral strike-slip motion (Marcotte et al., 2005). U-Pb dates from syn-kinematic titanite (Figures 8b and 10; Table 3), combined with the crystallization ages of deformed protoliths (Table 2), show that D_4 in both the lower and mid-crust occurred at 120–115 Ma.

4.2.5. D_5 Deformation

The fifth stage of deformation (D_5) affected only the lower crustal segment of the Grebe-IC shear zone at 115–110 Ma (Figure 10). No mid-crustal segments in Fiordland were active during this interval (Buriticá et al., 2019), although deformation in the Gutter shear zone (20–15 km depth) may have continued until ~112 Ma (Allibone & Tulloch, 2008). Near Milford Sound, D_5 structures are defined by vertical, N-striking, upper amphibolite-facies fabrics (L_5-S_5) that cut D_4 structures (Figure S5h in Supporting Information S1). Kinematic studies (Klepeis & King, 2009; Marcotte et al., 2005) show that these zones record sinistral, pure-shear-dominated, inclined transpression. U-Pb zircon dates from a syn-kinematic dike that both cuts L_5-S_5 and is folded within it suggest the deformation occurred through 114.7 ± 1.8 Ma (location 13, Figure 8b), which matches published interpretations (Hollis et al., 2003; Klepeis et al., 2004; Marcotte et al., 2005).

4.3. George Sound Shear Zone System

The GSSZ system extends ~125 km from the lower crust at Bligh Sound through the mid-crust west and south of Lake Manapouri (Figure 10). The SRSZ, which lies entirely within the lower crustal block (Figures 3b and 10), forms part of this system. The system is defined as magma-rich because large intrusions (Western Worsley, Misty, Malaspina, Resolution, Breaksea, and West Arm Leucogranite plutons) were emplaced into it during the 124–110 Ma interval (Figure 10). Five stages of Cretaceous tectonic activity occurred, two of which produced high-strain zones (Figures 10 and 11).

4.3.1. D_1 and D_2 Deformation

The 136–130 Ma stage of deformation (D_1), which occurred in the Grebe-IC system, is absent in the GSSZ and SRSZ. By ~124 Ma, the D_2 deformation front had reached the lower crust below George Sound (Figures 9 and 11) (Section 4.3.2) when two magma feeder zones (Figures 9 and 10) moved magma vertically into the lower crust (Figure 11) (Betka & Klepeis, 2013; Klepeis et al., 2016; Schwartz et al., 2017, this study), marking the beginning of D_3 magmatism.

4.3.2. D_3 Magmatism

D_3 began at ~124 Ma (Schwartz et al., 2016) when the Worsley pluton was emplaced into the root of the GSSZ system (Figure 11). New U-Pb zircon (Table 2) and titanite dates (Table 3) define older (124–121 Ma) and younger (115–110 Ma) lobes, which we designate the Western and Eastern Worsley plutons, respectively (Figure 10). Other intrusions include the 125–121 Ma Supper Cove and 128–120 Ma Eastern McKerr plutons (Table 2; Figures 7 and 10). The upper and lower contacts of the Western Worsley body are well-exposed and roughly coplanar, allowing us to measure its 19.5 km thickness (Figures 4a and 7, Figure S2 in Supporting Information S1). Above a magma-enhanced shear zone at its base, linear ($L_3 > S_3$) igneous fabrics record the lateral (WNE-ESE) flow of magma (Figures 10 and 11).

The shapes of the plutons that make up the WFO suggest they were fed by vertical feeders centered on inherited Carboniferous boundaries. The Western Worsley pluton, for example, resembles a mushroom where tabular lobes on the west and east steepen into a steep central zone (Figure 11) that aligns with the location of the Carboniferous boundary outside the pluton. One magma feeder exposed at George Sound (Figure 10) preserves subvertical magmatic flow fabrics (Figure S6a in Supporting Information S1). High-grade metamorphism at 750–800°C accompanied the magmatism (Tables 2 and 3; N. Daczko et al., 2001; Hollis et al., 2003; Stowell et al., 2010; Tulloch et al., 2011). Other episodes of Early Cretaceous metamorphism pre-date its emplacement (Figure S9 in Supporting Information S1).

Two other magma feeders are exposed in the SRSZ (Figure 10). The Breaksea domes represent the deep root of one of these where diapirs moved magma vertically into the crust from ≥65 km depth (Klepeis et al., 2016; Figures 6 and 11). The other is located in the NW Malaspina pluton (Figure 10) where subvertical fabrics record

the magmatic flow after ~120 Ma (Carty et al., 2021; Klepeis et al., 2016). A similar steepening of linear fabrics at Bligh Sound suggests that a fourth feeder lies below the Western Worsley pluton.

4.3.3. D_4 Deformation and Magmatism

The fourth stage (D_4) records an interplay between magmatism and deformation as the GSSZ and SRSZ grew during the 120–115 Ma interval. At Bligh Sound, a steep, 12-km-wide shear zone formed first inside the Western Worsley pluton along the same inherited boundary as the magma center that fed the pluton during D_3 (Figures 10 and 11). This shear zone crosses the pluton from its base at ~47 km depth to its top at ~37 km depth. Where it exits the upper (southern) contact, it splits into curved strands that follow the contacts between the Eastern McKerr and Expedition plutons and their metasedimentary hosts (Figures 10 and 11). South of George Sound, the strands branch upward and laterally inside the Misty pluton. One of these strands follows the late Carboniferous boundary near the eastern edge of the pluton (Figure 10), another merges with a detachment that underlies the mid-crustal Caswell fold-thrust belt (Daczko et al., 2002b; Figures 5, 10, and 11). The central high-strain zone crosses the Misty pluton where it connects with another detachment underlying a small mid-crustal fold-thrust belt at (SAB, Figure 5). Steep D_4 shear zones also cut across the base of the Western Worsley pluton (Figures 5 and 11).

U-Pb zircon dates and cross cutting relationships between high-strain zones and intrusions both show that D_4 deformation propagated from north to south and upward from the lower to the middle crust. North of and below the Misty pluton, part of the Eastern McKerr granite that is cut by a D_4 high-strain zone (Table 2) yielded an igneous crystallization age of ~120 Ma, placing a lower limit on D_4 at George Sound (see also Figure S6b in Supporting Information S1) A late syn-tectonic dike that cuts a D_4 high-strain zone but also is weakly folded within it (Figure S6c in Supporting Information S1) yielded a 119.5 ± 2.5 Ma U-Pb zircon crystallization age at the same locality. These dates indicate that the George Sound segment of the GSSZ had formed by ~120 Ma as emplacement of the 124–121 Ma Western Worsley pluton finalized. Farther south, the Misty and Western McKerr plutons provide maximum age limits of 118–114 Ma and ~118 Ma, respectively for the segments of the GSSZ inside them (Schwartz et al., 2017). Above the Misty pluton in the middle crust, Schwartz et al. (2016) showed that the Caswell fold-thrust belt formed after ~117 Ma and Blatchford et al. (2020) showed that the GSSZ did not extend farther up into the mid-crust until after ~115 Ma (Section 4.3.4). Together these results indicate that the GSSZ is oldest and deepest in the north (lower crust) and is younger to the south inside and above the Misty pluton (mid-crust) (Figure 11).

In addition to age differences, the conditions of deformation recorded by mineral fabrics in the GSSZ change from recording mostly solid-state deformation in the lower crustal Western Worsley pluton to recording mostly magmatic flow in the mid-crustal Misty pluton. Inside the latter, D_4 shear zones are composed of coarse, gneissic, linear fabrics that preserve igneous mineral textures and lack mylonite. Along the central high-strain zone, for example, coarse plagioclase displays straight grain boundaries, growth twins, and no evidence of dynamic recrystallization, and biotite occurs as laths rather than pressure shadows (*cf.* Blatchford et al., 2020). In contrast, $L_4 > S_4$ inside the Western Worsley pluton shows mineral textures indicative of synchronous deformation and high-T metamorphism in a mostly crystallized intrusion. In its lower crustal segment (Bligh Sound), pyroxene clusters are rimmed by asymmetric strain shadows composed of metamorphic clinopyroxene and hornblende, and plagioclase shows grain size reduction in mylonitic shear zones. U-Pb dates and zircon temperatures from paragneiss at Bligh and George sounds suggest that amphibolite-facies metamorphism and crustal melting occurred at 660–790°C during this interval. These observations are similar to the textural criteria described by others (Huber et al., 2011; Webber et al., 2015; Yoshinobu et al., 2009) where crystal-plastic deformation occurs at high temperatures near the solidus and enough solid material is present for mylonitic shear zones to form. They indicate that the lower crustal part of the GSSZ was deforming in a relatively strong, crystallized pluton while its mid-crustal portion was deforming a partially solidified magma mush during D_4.

4.3.4. D_5 Deformation and Magmatism

The fifth stage (D_5) (115–110 Ma) represents a period of strain localization in the lower crust and an expansion of high-strain zones vertically and laterally into the middle crust. Cross-cutting relationships with S_4 (Figure S6f in Supporting Information S1) and U-Pb zircon dates from syn- and post-kinematic dikes (Figures S6d and S6e in Supporting Information S1) indicate that D_5 in the lower crust occurred through 115.6 ± 1.9 Ma and was over by 107.7 ± 1.5 Ma (Figure 10, Table 2). In the middle crust, the Caswell fold-thrust belt continued to develop

until ~113 Ma (Schwartz et al., 2016) and the SAB thrust developed during the 114–111 Ma interval (Blatchford et al., 2020). Along the Fiordland coast, titanite dates (Two Thumbs Bay, Figure 10, Table 3) suggest that D_5 in the mid-crustal block between Caswell and George sounds occurred at ~112 Ma, which matches the age of the Caswell fold-thrust belt. Geochronology from Stewart Island suggests that reverse faults, including the Escarpment fault, formed in the upper crust after ~110 Ma until ~105 Ma (D_6) (Allibone & Tulloch, 2008).

During D_5, the 115–110 Ma Eastern Worsley pluton intruded the lower crust (Figure 10). Reactivation of the Mt Daniel shear zone (Figures 5 and 10) at the same time (Buriticá et al., 2019) suggests that this eastern lobe was sourced from below the western lobe. In the mid-crust, the West Arm Leucogranite was emplaced into the GSSZ system at 124–110 Ma (Buriticá et al., 2019; Scott & Palin, 2008). Metamorphic zircon ages from the George Sound Paragneiss (Table 2) and either igneous or metamorphic ages from intrusions east of the Misty pluton (Figures 7 and 10, Table 2) show that the middle and lower crust remained hot (660–785°C) throughout this period.

As the GSSZ system moved into the middle crust, D_5 in the lower crust narrowed into a ≤3 km-wide zone of mylonite inside the Western Worsley pluton (Figure 10). This zone records a progressive steepening of plagioclase, pyroxene, and hornblende mineral lineations to subvertical with increasing strain (Figure S6f in Supporting Information S1; Moyer et al., 2018). Biotite shear bands, hornblende fish and oblique plagioclase foliations record sinistral shear across the steep lineations, indicating triclinic strain symmetry. These elements show that the deepest part of the GSSZ records a non-partitioned style of inclined transpression where both the shortening and the strike-slip components were accommodated together in the same high-strain zone.

South of the Western Worsley pluton, narrow high-strain zones (D_5) cut across the Eastern McKerr and Misty plutons (Figure 10). From there the high-strain zones form detachments that underlie two mid-crustal fold-thrust belts on either side of the steep central shear zone (Figures 5 and 11) and record shortening at high angles to the GSSZ (Blatchford et al., 2020; Daczko et al., 2002b). In contrast, the steep central shear zone records mainly sinistral strike-slip motion in planes orientated at low angles to gently-plunging mineral stretching lineations. These patterns show increases in both the spacing of high-strain zones and the degree of displacement partitioning upwards from the lower crust into the middle crust.

South of the two thrust belts, and farther up into the mid-crustal block, the steep central high-strain zone follows the trace of the late Carboniferous fault into SE Fiordland (Figures 3b and 10). On Stewart Island, the Gutter shear zone records mid-crustal transpression at 15–20 km depth during this interval (Allibone & Tulloch, 2008). Displacements were mostly reverse with minor strike-slip motion.

4.3.5. D_6 Deformation and Magmatism

The sixth stage (D_6) marks the expansion of faults into the upper crust. On Stewart Island, the Escarpment fault cuts the 120–112 Ma Gutter shear zone and the 128–120 Ma Walkers pluton (Allibone & Tulloch, 2008). Lineation orientations, ^{40}Ar-^{39}Ar thermochronology, and Al-in-hornblende geobarometry indicate that relatively hot rocks were thrust on top of cooler rocks between c. 105 and 100 Ma (Allibone & Tulloch, 2008).

At deeper levels, felsic dikes were emplaced into the roots of the GSSZ and SRSZ (blue stars, Figure 10) and below the Western Worsley pluton. Most of these dikes are undeformed and range in age (U-Pb zircon) from ~108 to ~95 Ma (Tables 2 and 3). Their ages and abundance in the lower crust suggests that some may be linked to the final stage of subduction-related magmatism. However, they continued to be emplaced after the transition to extension at 108–106 Ma (Klepeis et al., 2007, 2016; Schwartz et al., 2016; van der Meer et al., 2018). Schwartz et al. (2016) found that many are A-type granites whose emplacement was accompanied by the growth of metamorphic zircon (see also samples 19MP26 and 19MP34, Table 2). Titanite temperatures from metasedimentary rock and amphibolite (Table 3) indicate that the lower crust remained hot (734–900°C) until at least ~100 Ma, suggesting that some dikes may reflect heating and lithospheric thinning during Gondwana breakup (Schwartz et al., 2016; Tulloch, Ramezani, Mortimer, et al., 2009).

5. Discussion

5.1. Structural Inheritance and Crustal Thickness

Our investigation of Fiordland's three steep crustal boundaries, which formed during the late Paleozoic (Figures 3–10), highlights the important role of structural inheritance as a mechanism for localizing deformation at all depths in the crust and for moving magma, fluid, and heat through continental lithosphere. Following an initial period of late Carboniferous transpression and magmatism, major reactivations of these boundaries occurred during Permian (290–274 Ma), Early Cretaceous (at least six events between 139 and 108 Ma), Late Cretaceous (96–93 Ma), and Eocene (~40 Ma) times. These events add to those identified in previous work, including late Carboniferous transpression in the mid-crustal portion of the Grebe-IC shear zone (Buriticá et al., 2019) and multiple Eocene and Mio-Pliocene fault reactivations of all three boundaries (Klepeis, Webb, Blatchford, Schwartz, et al., 2019, Klepeis, Webb, Blatchford, Jongens, et al., 2019). Together they illustrate how long-lived zones of weakness in the crust and lithospheric mantle influence batholith-scale magmatism as well as the initiation and growth of large continental faults and shear zones.

Our reconstruction also highlights potential crustal thickness variations across large shear zones (Figures 4 and 7). Published geochemical data from the WFO batholith support this interpretation. Major and trace element work (Carty et al., 2021; Schwartz et al., 2021) and zircon $\delta^{18}O$ and Lu-Hf isotopic analyses (Decker et al., 2017; Schwartz et al., 2021; Turnbull et al., 2021) suggest that the WFO plutons were sourced within the upper mantle and most likely were emplaced close to their source regions. Brackman and Schwartz (2022) confirmed this finding through a comparison of pluton emplacement depths, determined from contact aureole studies, Al-in-hornblende crystallization pressures, and modeled clinopyroxene crystallization pressures, with Moho-depth calculations based on bulk-rock geochemistry. The data suggest that the Moho in northern Fiordland was at or below 55 km (see also Mantle and Collins. (2008)) and decreases in south-central Fiordland (Figures 4 and 7). The Malaspina pluton and Resolution Orthogneiss show maximum emplacement depths of 44–50 km. The Misty pluton lies above the Malaspina pluton (above 40 km depth) and has an exposed top at ~25–27 km depth. Thus, these relationships suggest that the Moho beneath west-central Fiordland was shallower than in other areas (Figures 4 and 7). The thickest section is recorded by the Breaksea Orthogneiss, which suggests the crust may have reached ~65 km thick in this region by ~124 Ma (Figures 4 and 7). However, subsequent decompression (De Paoli et al., 2009; Klepeis et al., 2016; Stowell et al., 2017) suggests that crustal thicknesses in this area also was close to 45–50 km by the time the Malaspina, Resolution Orthogneiss and Misty plutons were emplaced at ~118 Ma.

The location of these inferred changes in Moho depth suggests that the offsets could have resulted from vertical motion along the Grebe-IC and GSSZs. Klepeis, Webb, Blatchford, Schwartz, et al. (2019), Klepeis, Webb, Blatchford, Schwartz, et al. (2019) attributed some offset to Miocene-Pliocene faulting within these shear zones. We suggest that some offset also could have occurred during late Carboniferous transpression when the boundaries first formed. This latter interpretation explains why Cretaceous pluton emplacement depths, which appear to mimic crustal thickness, were variable. Vertical offset across the GSSZ also agrees with both changes in mantle isotopic domains across this boundary (Schwartz et al., 2021) and differences in Moho-depth calculations based on geochemistry (Brackman & Schwartz, 2022). The magnitude of the offset is in the 5–10 km range, which is similar to relationships observed in the Coast shear zone of SE Alaska and British Columbia (Morozov et al., 2001) and the Bangong Suture in the NW Himalaya (Rai et al., 2006). Norris and Toy (2014) also show a 9 km deepening of Moho across the Alpine fault from west to east. These features highlight the importance of steep, crustal-scale faults, which can continue to influence tectonic deformation in intraplate settings long after their formation.

5.2. Grebe-Indecision Creek Shear Zone System

5.2.1. Initiation and Downward Growth

The results of this study show that the Grebe-IC shear zone system initiated as an oblique-reverse fault along a late Carboniferous boundary that defines the Paleozoic edge of SE Gondwana (Figures 2, 3b, and 11). Cretaceous deformation began at ~136 Ma shortly after a terminal phase (147–136 Ma) of magmatism in the eastern outboard arc (Figures 9 and 12a; Ringwood et al., 2021). This pulse produced a thermal and metamorphic front that penetrated into what is now NW Fiordland. Stitching dikes emplaced prior to ~136 Ma indicate that the outboard arc

was building continentward and must have been in contact with the Gondwana margin by ~146 Ma and probably long before this time (see also Schwartz et al., 2021). The oblique-reverse faulting (D_1) thus marks the initiation of a period (136–124 Ma) of intracontinental deformation when the outboard arc was underthrust to lower crustal depths beneath a thermally softened margin during oblique convergence (Figures 11 and 12a). Underthrusting of the Eastern Isotopic Domain (EID) below the Central Isotopic Domain (CID) (Figure 7) shows that this deformation was deep-seated (Schwartz et al., 2021).

A comparison of D_1 ages along the ~330 km length of the system suggests that deformation began at middle crustal (~20 km) depths. The oldest D_1 mylonites occur at the base of the mid-crustal block at Milford Sound (this study) and in the mid-crustal block south of Worsley Arm (Figure 9; Buriticá et al., 2019). From the mid-crust, the deformation propagated downward to the NW, reaching depths of ~55 km after ~129 Ma and the base of the lower crust by ~124 Ma. The arrival of the D_2 front below what is now southern George Sound by ~124 Ma (Figures 9, 11, and 12b) coincided in space and time with the initial magma flare-up that fed melts into the base of the GSSZ and SRSZ, forming the Western Worsley and Eastern McKerr plutons (Figure 12c). This magmatism was part of a new phase of continentward arc migration that began with the intrusion of the Separation Point Suite at ~129 Ma (Schwartz et al., 2017, 2021; Scott et al., 2009).

5.2.2. Reactivations

After its formation as an oblique-reverse fault, the Grebe-IC shear zone was reactivated by several episodes of transpression. Another style of reactivation involved the emplacement of small batches of magma and fluids into the shear zone without transpressional shearing. These latter reactivations occurred during periods of relative quiescence when most of the deformation within the margin was focused on structures located within the continental interior. One period of quiescence occurred at 124–121 Ma (D_3) when small magma batches, including the 123–120 Ma Puteketeke pluton (Buriticá et al., 2019; Ramezani & Tulloch, 2009), were emplaced into and near the Grebe-IC shear zone after the D_2 front had migrated west (Figure 10). This period was followed by a transpressional reactivation of its middle and lower crustal segments (20–55 km depth) at 120–115 (D_4). During D_5 (115–110 Ma), the lower crust below 35 km depth was deforming and began to propagate upward into the middle and upper crust (Figure 10). During this period of lower crustal flow, the mid- and upper crustal parts the system were either locked or deformation was occurring elsewhere away from the old Carboniferous boundaries. Other periods of fluid infiltration and fault reactivation occurred during the Cenozoic (Klepeis, Webb, Blatchford, Schwartz, et al., 2019, Klepeis, Webb, Blatchford, Jongens, et al., 2019).

5.2.3. Displacement History

The geometry of structures in the Grebe-IC shear zone system, and their evolution, provide us with the means to estimate the directions, amounts, and time-averaged rates of displacement for different intervals. For D_1, shear sense indicators and the L_1 lineation orientations indicate a NW-SE shortening direction with a component of sinistral strike-slip motion parallel to the Grebe-IC trace (Figure 9). Displacements for this phase (136–130 Ma) are poorly known but are likely <10 km given the short duration of the event and minor deflections of S_1 foliations (Figure 9). This estimate is similar to the ≤10 km of cumulative offset inferred for the Freshwater fault on Stewart Island (Allibone & Tulloch, 2008).

The orientation of the displacement vector ($\vec{F_d}$) during D_2 can be inferred using the trajectories of L_2 mineral stretching lineations drawn on the middle and lower crustal blocks in Figure 9. This use of the lineation orientations is justified by several means. First, shear sense indicators show that the D_2 vorticity normal section is consistently steep and strikes to the NW-SE parallel to the trend of most of the L_2 lineations in the lower crustal block (Figure 9). Second, variations in F_2 fold tightness record NW-SE shortening during D_2. Third, variations in the orientations of L_2 mineral lineations are most common in areas of F_2 folding. In the hinges of tight folds, for example, L_2 commonly plunges to the SW and NE, parallel to F_2 fold axes (Marcotte et al., 2005). In these zones, asymmetric kinematic indicators record NW-SE reverse displacements. These observations all suggest that the L_2 lineations track the direction of shortening as the outboard arc was underthrust beneath Gondwana over the 130–124 Ma interval.

A comparison of S_2 and L_2 structures in the lower and mid-crustal blocks shows that some lateral variation in the orientation of the displacement vector could have occurred along the margin (Figure 9, inset). L_2 is highly oblique to the trend of the shear zone boundary in the mid-crustal block west of Lake Te Anau and is less so

farther north in the lower crustal block (Figure 9). Other variations include an apparent increase in plunge angles with increasing strain, which was assessed qualitatively using F_2 fold tightness as a proxy for strain magnitude. Foliation planes (S_2) near Milford Sound also display a sinistral rotation in strike from SE to NW as finite strains increased, which we interpret to reflect a component of sinistral strike-slip motion (Figure 9).

Our ability to link both D_1 and D_2 to the oblique underthrusting of the outboard arc beneath Gondwana from SE to NW (Section 4.2.2), and the record of where these events began and ended, provides us with a means of estimating the magnitude of this displacement. Since D_1 records the initiation of the underthrusting at the Grebe-IC boundary and D_2 records its NW propagation to the GSSZ (Section 4.2.2), the distance between these two structures parallel to L_2 gives us a minimum distance for the underthrusting (Figure 9 inset). Near Milford Sound (lower crust), which has the most L_2 control points, this distance gives a minimum of ~30 km of horizontal shortening parallel to L_2 by ~124 Ma. Another estimate, made in the mid-crustal block near Lake Te Anau, gives a similar 30 km minimum (Figure 9, inset). This latter site preserves the full distance between the Grebe-IC and GSSZ. If, as may be the case near the southern part of the lake, the displacement vector initially pointed north, the displacements reached a maximum of 45 km. This estimate of 30–45 km of horizontal displacement in 14 m.y. (130–124 Ma) suggests a time-averaged slip rate of 2–3 mm yr^{-1} for D_2.

The orientation and magnitude of the D_2 displacement vector described above also allowed us to estimate the magnitude of D_2 strike-slip displacements within the Grebe-IC system. Between Milford Sound and Lake Te Anau, sinistral displacements range from a minimum of 24 km to a maximum of 34 km (Figure 9, inset). Vertical displacement during D_2 can be estimated using the difference in paleodepth between the mid-crustal block east of Milford Sound and the lower crustal block. This difference suggests that the outboard arc was underthrust from 20 km to at least 55 km depth between ~130 and ~124 Ma (Figures 11, 12a, and 12b). The dip of the underthrust surface is approximate, but conforms to a swath of SW-dipping mid-lower crustal reflectors inside the Median Batholith (Mortimer et al., 2002). Observations on Stewart Island suggest moderate (50°–70°) dips in the upper crust (Allibone & Tulloch, 2008; R. Turnbull et al., 2010). The orientation of the Carboniferous structures outside the shear zones (e.g., profile E-E', Figure S4 in Supporting Information S1) suggest similar SW dips, suggesting they once formed an imbricate system of late Paleozoic reverse faults.

Using structures that formed during D_4, Buriticá et al. (2019) showed that the mid-crustal portion of the Grebe-IC shear zone accommodated a minimum of 2%–3% shortening and up to 10 km of sinistral horizontal offset during the 122–117 Ma interval. This magnitude roughly matches our estimate of the amount of displacement accumulated in the lower crustal portion of the shear zone during D_4 and D_5 using the deflection of foliations into high-strain zones. These authors also suggested that at least 11–15 km of vertical displacements accumulated prior to emplacement of the 123–120 Ma Puteketeke pluton at 20–24 km depth.

5.3. George Sound Shear Zone System

5.3.1. Initiation and Upward Growth

The GSSZ system initiated when the D_2 deformation front, which began propagating into Gondwana at ~129 Ma, reached the base of the lower crust below George Sound at ~124 Ma (Figures 9 and 12c). At this time, two magmatic feeders moved magma into the roots of the system from deep melt reservoirs in the Western Isotopic domain (Klepeis et al., 2016; Schwartz et al., 2021). This initial pulse of magmatism emplaced the 124–121 Ma Western Worsley and Supper Cove plutons (Figure 10). In the former, hypersolidus flow spread magma laterally on either side of the shear zone, forming a mushroom-shaped pluton at 35–47 km depth (Figure 12c), while partial melting and granulite metamorphism softened the crust below it (N. Daczko et al., 2001; Hollis et al., 2003; Stowell et al., 2010; Tulloch et al., 2011).

The close relationship between magmatism and the onset of deformation in the GSSZ at ~124 Ma suggests that D_2, which tracked the underthrusting of the outboard arc beneath Gondwana, could have helped drive some melt segregation. However, this underthrusting did not ignite the Cretaceous flare-up because there is little evidence for contributions of the outboard arc (i.e., low $\delta^{18}O$ values) in melts that produced the WFO batholith (Decker et al., 2017; Ringwood et al., 2021; Schwartz et al., 2017, 2021). This contrasts with the models of Ducea (2001) and DeCelles et al. (2009), which emphasize crustal contributions from underthrust crust (see also Cecil et al., 2018).

By ~120 Ma, deformation inside the Western Worsley pluton formed a steep zone of lower crustal transpression up to 12 km wide (Figures 10 and 12d). No significant deformation is recorded in the mid-crust above the pluton prior to ~120 Ma, indicating that the lower and middle crust were decoupled briefly across the crystallizing pluton at 124–120 Ma. Below the Western Worsley pluton, a series of narrow shear zones reactivated steep D_2 structures, forming a wide curtain of deformation (Figure 12d). By ~118 Ma, the Misty, Western McKerr, and Malaspina plutons where emplaced below depths of ~25 km (Figures 7 and 13a). These plutons record the emplacement of ~70% of the lower crust in Fiordland within 3 m.y. (118–115 Ma) (Schwartz et al., 2017).

As the Misty pluton was emplaced, thin (1–2 km wide) high-strain zones propagated through it into the middle crust above ~25 km depth where the zone of deformation widens laterally above several flat detachments (Figures 5, 11, and 13a). By ~115 Ma, deformation below ~37 km had localized into 2–4 km-wide zones of amphibolite-facies mylonite inside the now solidified Western Worsley pluton. At the same time, high-strain zones that record hypersolidus flow formed inside the still partially molten Misty pluton in the middle crust while the West Arm Leucogranite intruded at 25–20 km depth (Figures 10 and 13b). These patterns show that at 115 Ma the younger, hotter, and partially molten Misty pluton must have been weaker than the older and fully crystallized Western Worsley pluton below it. Therefore the rheology of the GSSZ, which deformed both bodies, was different in each pluton. The changes in the relative strength of crustal layers as the Misty and Western Worsley plutons cooled and crystallized at different times is illustrated in Figures 11 and 13a, which emphasize the formation of detachments at the top and base of the pluton.

By ~110 Ma, both the Caswell fold-thrust belt and SAB thrust were well developed at 25–20 km depth as deformation spread laterally and vertically within the middle crust above a series of small detachments at and above the Misty pluton (Figures 11 and 13a). While this occurred, deformation localized into thin, mylonitic high-strain zones inside the Misty pluton, indicating that this pluton had solidified. In the upper crust, reverse faults (the Escarpment fault on Stewart Island) placed hot rocks over cool rocks at 105–100 Ma (Allibone & Tulloch, 2008). This vertical migration of deformation from 65–55 km to ~5 km depth over the 124–105 Ma interval implies a time-averaged vertical growth rate of ~3 mm yr^{-1}. The deflection of foliation traces into the GSSZ at Bligh Sound suggests small (<10 km) lateral displacements.

5.3.2. Magma-Deformation Interactions

Throughout the Late Cretaceous, arc magmatism influenced deformation patterns in the Median Batholith in a variety of ways. In both shear zone systems, deformation began shortly after plutons infiltrated these structures. Similar relationships have been observed in the Western Idaho shear zone (Giorgis et al., 2005) and the southern Sierra Nevada batholith (Saleeby et al., 2008). In the GSSZ, for example, deformation began near the base of the crust and subsequently migrated upwards into areas where plutons had intruded (Figures 12 and 13). This upward migration of high-strain zones that followed plutons as they were emplaced at successively shallower depths indicates that magmatism helped drive shear zone reactivation and growth.

The downward and continentward growth of the Grebe-IC shear zone also appears to have been influenced by the timing and spatial pattern of magmatism. By ~136 Ma, D_1 deformation had localized within this structure shortly following a period of magma infiltration. This magmatism was accompanied by high-grade metamorphism that penetrated far into the interior of Gondwana, effectively weakening a thick lower crustal layer (Figure 11; Blatchford et al., 2020; N. Daczko et al., 2001; Hollis et al., 2003; Klepeis et al., 2016; Schwartz et al., 2016; Stowell et al., 2010; Tulloch et al., 2011). Magmatism also migrated west, further weakening the continental interior and helping to create a lateral strength contrast between older, cooler, and stronger middle crust of the outboard arc and hot, weak lower crust of the Gondwana margin (Figure 11). This strength contrast across the Grebe-IC shear zone (Figure 11) appears to have helped promote the oblique underthrusting of the outboard arc beneath Gondwana and the downward growth of the system from a relatively cool middle crust into a hot, weak lower crust.

Other effects of magmatism on deformation patterns within the batholith can be attributed to rapid changes in the strength profile of the middle and lower crust as thick, tabular plutons intruded and then solidified. In the Western Worsley pluton, for example, the GSSZ narrowed from ~12 km wide to 1–2 km in only ~3 m.y. during D_4 (Figure 10). By ~115 Ma, this pluton had solidified and was strong relative to the younger, and still partially molten, Misty pluton next to it (Figure 11) (Section 4.3.3). By ~110 Ma, the Misty pluton had solidified and was strong relative to a hot, quartz- and mica-rich middle crust (Blatchford et al., 2020). These changes in the strength

of crustal layers (Figure 11) are recorded by mineral fabrics inside the plutons (described in Section 4.3.3), and by the emplacement of dikes with sharp, straight edges starting at ~108 Ma (*cf*., Blatchford et al., 2020; Klepeis et al., 2016; this study). One of the primary effects of these changes was that as high-strain zones (D_4 and D_5) propagated through the Misty pluton, detachments formed at its top where strength contrasts were most pronounced (Figure 11). This resulted in a three-fold increase in the width of the system as the deformation was spread across ~35 km-wide zone in the mid-crust (i.e., from western Caswell S. to SAB in Figure 10, see also Figures 5, 11, and 13). The lateral increase in fault spacing also was accompanied by increased displacement partitioning where the shortening and strike-slip components of transpression were accommodated on separate structures to varying degrees. The overall pattern allowed the rather small total displacements of <10 km in the GSSZ to be distributed across many more structures in the upper crust compared to the lower crust where all components of transpression were accommodated in one primary steep shear zone. This development highlights how the emplacement and solidification of thick tabular plutons in the lower crust influenced the growth, width, and degree of partitioning in the GSSZ.

Finally, we point out that, despite contrasts in the relative strength of layers, Fiordland's middle and lower crustal section remained relatively hot (650–800°C) during all six of the tectonic events defined here (Blatchford et al., 2020; N. Daczko et al., 2001; Hollis et al., 2003; Klepeis et al., 2016; Schwartz et al., 2016; Stowell et al., 2010; Tulloch et al., 2011; this study). This persistence of elevated lower crustal temperatures may help explain the long ~30 Ma duration of orogenesis within the batholith. Previous work in other hot orogens, many of them Proterozoic (Chardon et al., 2009; Spencer et al., 2021), suggest that elevated temperatures both prolong orogenesis and influence its overall style, a result that is supported by the Fiordland example.

5.4. The End of Subduction and the Onset of Extension

The six stages of tectonic activity we define show a change in the style of deformation and magmatism in the deep crust after ~124 Ma (Figures 9, 10, 12, and 13). D_1 and D_2 represent a period (136–124 Ma) of intense arc-perpendicular shortening as the outboard batholith was underthrust to lower crustal depths. However, by the end of the early stage of D_4 (120–118 Ma) (Figure 12d), this underthrusting had either slowed or stopped and the amount of arc-perpendicular shortening had decreased. Although both the Grebe-IC and the GSSZs show evidence of transpression, a comparison of both shows that the kinematics of deformation and its growth patterns changed during D_4 (Figures 12b and 12d). In particular, the magnitude of arc-normal shortening decreased after D_2. This transformation conforms to the predictions of Tulloch et al. (2011), Decker et al. (2017), and Schwartz et al. (2017), who suggested that changes in subduction zone geometry triggered major changes in the evolution of the arc after ~136 Ma. In particular, Decker et al. (2017) developed a model whereby a tear or ridge-trench collision formed a slab window and caused upwelling of the asthenospheric mantle by 118–114 Ma. In their interpretation, the upwelling melted the subcontinental lithospheric mantle and resulted in high-temperature metamorphism, partial melting, and high magma addition rates. The sequence of events we identified (D_1–D_6) support this view by suggesting that subduction was dominant from ~136 to ~124 Ma and had slowed or ended by ~115 Ma, and that contraction in the deep crust had ceased by ~110 Ma.

This sequence of events also is compatible with previous work showing when extension began within the Median Batholith. Klepeis et al. (2016) showed that lower crustal flow patterns had changed by ~114 Ma, as the Breaksea and Malaspina gneiss domes formed south of Doubtful Sound (Figure 10). These gneiss domes may record the beginning of lower-crustal thinning while subduction slowed and/or stopped. By 108–106 Ma, extension was widespread and had formed the lower crustal Doubtful Sound shear zone (106–97 Ma) (Figure 2; Klepeis et al., 2016; Schwartz et al., 2016) and the Paparoa metamorphic core complex in the middle crust (Schulte et al., 2014; Spell et al., 2000; Tulloch & Kimbrough, 1989). The Resolution Island shear zone formed next at 95–89 Ma, as the deformation migrated continentward (Klepeis et al., 2016).

6. Summary and Conclusions

Zealandia's Median Batholith records how two large transpressional shear zone systems initiated and grew through a thick section of continental arc crust during oblique convergence. The two systems show different growth patterns, contrasting relationships with respect to arc magmatism, and different crustal architectures with depth.

The Grebe-Indecision Creek shear zone system formed first at ~136 Ma by reactivating a boundary that once marked the late Carboniferous edge of Gondwana. In the upper crust (<15 km depth), the system is composed of discrete, moderately-dipping reverse faults that transition downward into a mesh-like network of steep, 1–2 km-wide, mylonitic shear zones in the middle crust (15–35 km depth). The mid-crustal mylonites form a ~10 km-wide zone of transpression that coalesces downward into a steep, 4 km-wide zone of inclined, amphibolite-facies transpression in the lower crust (35–55 km depth). The deformation initiated at or above ~20 km depth as an oblique-reverse fault that accommodated the partial subduction of an outboard part of the Median Batholith beneath Gondwana. This system was magma-poor after ~136 Ma, developing shortly after a terminal phase (147–136 Ma) of magmatism in the outboard arc. It then propagated downward at ~2–3 mm yr^{-1} reaching the base of the lower crust by ~124 Ma and accumulating at least 30–45 km of horizontal (arc-normal) shortening, ~35 km of (NW over SE) vertical displacements, and ≤10 km of lateral displacements from 136 to 124 Ma.

The GSSZ system nucleated at or near the base of the lower crust (~55 km depth) within another inherited, late Carboniferous boundary and propagated upward. This system incorporated a major flare-up in arc magmatism that began at ~124 Ma and peaked at 118–115 Ma when ~70% of the arc root was emplaced. By ~120 Ma, transpression had formed a steep, 12-km-wide shear zone inside a ~20 km-thick, partially molten, lower crustal pluton (the Western Worsley) that quickly (in ~3 m.y.) narrowed into a 1–2 km-wide zone of amphibolite-facies mylonite as the intrusion solidified. While other plutons intruded from 118 to 115 Ma, steep high-strain zones propagated upward across them at ~3 mm yr^{-1}, reaching mid-crustal depths (30–25 km) by ~115 Ma and the upper crust (<15 km) after ~110 Ma. When the high-strain zones entered the middle crust, the system widened by a factor of three as fold-thrust belts formed on either side of a steep, central shear zone. This growth pattern, which included the rapid formation and disappearance of detachments at the tops and bottoms of the solidifying plutons, generated faults located tens of km apart that were mechanically linked to a central zone of transpression in the deep crust. At its shallowest levels, the system is marked by narrow fault zones that offer no hint of the geometric complexity at depth.

These results show that the primary driver of strain localization in both shear zone systems at all depths was the reactivation of two steep, inherited boundaries after magma infiltrated their roots. The two systems each record multiple reactivations. Fluid and heat continued to move through the lithosphere along these boundaries between periods of fault movement, even after ~115 Ma when subduction had slowed or ended and after ~110 Ma when contraction ceased entirely. The intrusion of plutons whose physical properties changed over time was the primary cause of geometric complexity. Pluton solidification influenced shear zone width, increased vertical coupling between the lower and middle crust, promoted the formation of short-lived detachments, drove deformation out of a strengthening lower crust and into a weaker middle crust, and increased displacement partitioning. These interactions show how the inboard part of the Median Batholith was built from the bottom up as a result of synchronous magmatism and deformation. They also highlight how magmatism influences the way in which propagating shear zones interact with compositional and rheological boundaries in the crust.

Acknowledgments
Funding to support this work was provided by National Science Foundation (NSF) grants EAR-1119248 (Klepeis), EAR-1650219 (Miranda), EAR-1352021 (Schwartz). We thank Andrew Allibone for sharing field data and Andrew Tulloch, Nick Mortimer at GNS (Dunedin) and Gabriela Mora-Klepeis for many discussions and assistance. Hannah Blatchford, Griffin Moyer, Chris Eddy, Kendra Carty, Matthew Dietel, Brandon Page, and Emily Lincoln conducted field work and contributed discussions and analyses. Jesse Lee provided undergraduate research assistance. We thank the Department of Land Conservation Te Anau office for permission to visit and sample sites. We also thank Peter Kuiper of Cruise Te Anau and Seán Ellis and Maria Kuster of Pure Salt for logistical assistance.

Data Availability Statement

Physical samples are archived at the University of Vermont, California State University Northridge, and in the GNS Science collections. Sample metadata are archived online in the Petlab (https://pet.gns.cri.nz/pet/) database and the System for Earth Sample Registration http://www.geosamples.org. Metadata can be retrieved from these databases using the sample identifiers listed in the geochronology and geochemistry data tables posted on the Dryad online data repository at https://doi.org/10.5061/dryad.kh189326h (Klepeis et al., 2022).

References

Allibone, A. H., & Craw, D. (2016). Lithospheric controls on the metallogeny of basement rocks in southern and western New Zealand. In A. B. Christie (Ed.), *Mineral deposits of New Zealand: Exploration and research*. The Australasian Institute of Mining and Metallurgy. AUSIMM Monograph 31.

Allibone, A. H., Jongens, R., Scott, J. M., Tulloch, A. J., Turnbull, I. M., Cooper, A. F., et al. (2009). Plutonic rocks of the median batholith in eastern and central Fiordland, New Zealand: Field relations, geochemistry, correlation, and nomenclature. *New Zealand Journal of Geology and Geophysics*, *52*(2), 101–148. https://doi.org/10.1080/00288300909509882

Allibone, A. H., Jongens, R., Turnbull, I. M., Milan, L. A., Daczko, N. R., De Paoli, M. C., & Tulloch, A. J. (2009). Plutonic rocks of western Fiordland, New Zealand: Field relations, geochemistry, correlation, and nomenclature. *New Zealand Journal of Geology and Geophysics*, *52*(4), 379–415. https://doi.org/10.1080/00288306.2009.9518465

Allibone, A. H., MacKenzie, D., Turnbull, R., Tulloch, A., & Craw, D. (2016). Polymetallic mineralisation associated with Carboniferous I-type granitoids in central Stewart Island, New Zealand. *New Zealand Journal of Geology and Geophysics*, *59*(3), 436–456. https://doi.org/10.1080/00288306.2016.1174946

Allibone, A. H., MacKenzie, D. J., Turnbull, R., Tulloch, A. J., Craw, D., & Palin, M. (2016). Polymetallic mineralised veins in ferroan/A-type cretaceous leucogranite, Stewart Island, New Zealand. *New Zealand Journal of Geology and Geophysics*, *59*(3), 457–474. https://doi.org/10.1080/00288306.2016.1174947

Allibone, A. H., Milan, L. A., Daczko, N. R., & Turnbull, I. M. (2009). Granulite facies thermal aureoles and metastable amphibolite facies assemblages adjacent to the western Fiord-land orthogneiss in southwest Fiordland, New Zealand. *Journal of Metamorphic Geology*, *27*(5), 349–369. https://doi.org/10.1111/j.1525-1314.2009.00822.x

Allibone, A. H., & Tulloch, A. J. (2004). Geology of the plutonic basement rocks of Stewart Island, New Zealand. *New Zealand Journal of Geology and Geophysics*, *47*(2), 233–256. https://doi.org/10.1080/00288306.2004.9515051

Allibone, A. H., & Tulloch, A. J. (2008). Early cretaceous dextral transpressional deformation within the Median batholith, Stewart Island, New Zealand. *New Zealand Journal of Geology and Geophysics*, *51*(2), 115–134. https://doi.org/10.1080/00288300809509854

Anderson, I., Stowell, H. H., Schwartz, J. J., Klepeis, K. A., Bollen, E. M., & Miranda, E. A. (2019). Pressure, temperature, and timing of magma intrusion and metamorphism, George Sound New Zealand. In *Geological Society of America Abstracts with Programs* (Vol. 51). https://doi.org/10.1130/abs/2019AM-337312

Ault, A. K., Reiners, P. W., Evans, J. P., & Thomson, S. N. (2015). Linking hematite (U-Th)/He dating with the microtextural record of seismicity in the Wasatch fault damage zone, Utah, USA. *Geology*, *43*(9), 771–774. https://doi.org/10.1130/g36897.1

Betka, P. M., & Klepeis, K. A. (2013). Three-stage evolution of lower crustal gneiss domes at Breaksea entrance, Fiordland, New Zealand. *Tectonics*, *32*(5), 1084–1106. https://doi.org/10.1002/tect.20068

Bhattacharya, S., Kemp, A. I. S., & Collins, W. J. (2018). Response of zircon to melting and metamorphism in deep arc crust, Fiordland (New Zealand): Implications for zircon inheritance in cordilleran granites. *Contributions to Mineralogy and Petrology*, *173*(4), 28. https://doi.org/10.1007/s00410-018-1446-5

Black, L. P., Kamo, S. L., Allen, C. M., Davis, D. W., Aleinikoff, J. N., Valley, J. W., et al. (2004). Improved Pb-206/U-218 microprobe geochronology by the monitoring of a trace-element-related matrix effect; SHRIMP, ID-TIMS, ELA-ICP-MS and oxygen isotope documentation for a series of zircon standards. *Chemical Geology*, *205*(1–2), 115–140. https://doi.org/10.1016/j.chemgeo.2004.01.003

Blatchford, H. J., Klepeis, K. A., Schwartz, J. J., Jongens, R., Turnbull, R. E., Miranda, E. A., et al. (2020). Interplay of Cretaceous transpressional deformation and continental arc magmatism in a long-lived crustal boundary, central Fiordland, New Zealand. *Geosphere*, *16*(5), 125–1248. https://doi.org/10.1130/GES02251.1

Bolhar, R., Weaver, S. D., Palin, J. M., Cole, J. W., & Paterson, L. A. (2008). Systematics of zircon crystallisation in the Cretaceous Separation Point Suite, New Zealand, using U/Pb isotopes, REE and Ti geothermometry. *Contributions to Mineralogy and Petrology*, *156*(2), 133–160. https://doi.org/10.1007/s00410-007-0278-5

Brackman, A. J., & Schwartz, J. J. (2022). The formation of high-Sr/Y plutons in cordilleran-arc crust by crystal accumulation and melt loss. *Geosphere*, *18*, 1–24. https://doi.org/10.1130/GES02400.1

Bradshaw, J. Y. (1989). Origin and metamorphic history of an early cretaceous polybaric granulite terrain, Fiordland, southwest New Zealand. *Contributions to Mineralogy and Petrology*, *103*(3), 346–360. https://doi.org/10.1007/BF00402921

Bradshaw, J. Y. (1990). Geology of crystalline rocks of northern Fiordland; details of the granulite facies western Fiordland orthogneiss and associated rock units. *New Zealand Journal of Geology and Geophysics*, *33*(3), 465–484. https://doi.org/10.1080/00288306.1990.10425702

Bürgmann, R., & Dresen, G. (2008). Rheology of the lower crust and upper mantle: Evidence from rock mechanics, geodesy, and field observations. *Annual Review of Earth and Planetary Sciences*, *36*(1), 531–567. https://doi.org/10.1146/annurev.earth.36.031207.124326

Buriticá, L. F., Schwartz, J. J., Klepeis, K. A., Miranda, E. A., Tulloch, A. J., Coble, M. A., & Kylander-Clark, A. R. C. (2019). Temporal and spatial variations in magmatism and transpression in a Cretaceous arc, Median batholith, Fiordland, New Zealand. *Lithosphere*, *11*(5), 652–682. https://doi.org/10.1130/L1073.1

Caine, J. S., Evans, J. P., & Forster, C. B. (1996). Fault zone architecture and permeability structure. *Geology*, *24*(11), 1025–1028. https://doi.org/10.1130/0091-7613(1996)024<1025:FZAAPS>2.3.CO;2

Calzolari, G., Rossetti, F., Ault, A. K., Lucci, F., Olivetti, V., & Nozaem, R. (2018). Hematite (U-Th)/He thermochronometry constrains strike-slip faulting on the Kuh-e-Faghan fault, central Iran. *Tectonophysics*, *728–729*, 41–54. https://doi.org/10.1016/j.tecto.2018.01.023

Carty, K., Schwartz, J. J., Wiesenfeld, J., Klepeis, K. A., Stowell, H. H., Tulloch, A., & Barnes, C. G. (2021). The generation of arc andesites and dacites in the lower crust of a cordilleran arc, Fiordland, New Zealand. *Journal of Petrology*, *62*(9), egab043. https://doi.org/10.1093/petrology/egab043

Cecil, M. R., Rusmore, M. E., Gehrels, G. E., Woodsworth, G. J., Stowell, H. H., Yokelson, I. N., et al. (2018). Along-strike variation in the magmatic tempo of the Coast Mountains batholith, British Columbia, and implications for processes controlling episodicity in arcs. *Geochemistry, Geophysics, Geosystems*, *19*(11), 4274–4289. https://doi.org/10.1029/2018GC007874

Chapman, T., Clarke, G. L., & Daczko, N. R. (2016). Crustal differentiation in a thickened arc—Evaluating depth dependences. *Journal of Petrology*, *57*(3), 595–620. https://doi.org/10.1093/petrology/egw022

Chapman, T., Clarke, G. L., Daczko, N. R., Piazolo, S., & Rajkumar, A. (2015). Orthopyroxene–omphacite- and garnet–omphacite-bearing magmatic assemblages, Breaksea orthogneiss, New Zealand: Oxidation state controlled by high-P oxide fractionation. *Lithos*, *216–217*, 1–16. https://doi.org/10.1016/j.lithos.2014.11.019

Chardon, D., Gapais, D., & Cagnard, F. (2009). Flow of ultra-hot orogens: A view from the Precambrian, clues for the Phanerozoic. *Tectonophysics*, *477*(3–4), 105–118. https://doi.org/10.1016/j.tecto.2009.03.008

Chatzaras, V., Tikoff, B., Newman, J., Withers, A. C., & Drury, M. R. (2015). Mantle strength of the San Andreas fault system and the role of mantle-crust feedbacks. *Geology*, *43*(10), 891–894. https://doi.org/10.1130/g36752.1

Clarke, G. L., Daczko, N. R., Klepeis, K. A., & Rushmer, T. (2005). Roles for fluid and/or melt advection in forming high-P mafic migmatites, Fiordland, New Zealand. *Journal of Metamorphic Geology*, *23*(7), 557–567. https://doi.org/10.1111/j.1525-1314.2005.00594.x

Clarke, G. L., Daczko, N. R., & Miescher, D. (2013). Identifying relic igneous garnet and clinopyroxene in eclogite and granulite, Breaksea orthogneiss, New Zealand. *Journal of Petrology*, *54*(9), 1921–1938. https://doi.org/10.1093/petrology/egt036

Clarke, G. L., Klepeis, K. A., & Daczko, N. R. (2000). Cretaceous high-P granulites at Milford sound, New Zealand: Metamorphic history and emplacement in a convergent margin setting. *Journal of Metamorphic Geology*, *18*(4), 359–374. https://doi.org/10.1046/j.1525-1314.2000.00259.x

Coble, M. A., Vazquez, J., Barth, A. P., Wooden, J., Burns, D., Kylander-Clark, A., et al. (2018). Trace element characterization of MAD-559 zircon reference material for ion microprobe analysis. *Geostandards and Geoanalytical Research*, *42*(4), 481–497. https://doi.org/10.1111/ggr.12238

Condit, C. B., & Mahan, K. H. (2018). Fracturing, fluid flow, and shear zone development: Relationship between chemical and mechanical processes in proterozoic mafic dikes from southwestern Montana, USA. *Journal of Metamorphic Geology*, *36*(2), 195–223. https://doi.org/10.1111/jmg.12289

Cyprych, D., Piazolo, S., & Almqvist, B. S. G. (2017). Seismic anisotropy from compositional banding in granulites from the deep magmatic arc of Fiordland, New Zealand. *Earth and Planetary Science Letters*, *477*, 156–167. https://doi.org/10.1016/j.epsl.2017.08.017

Daczko, N., Clarke, G. L., & Klepeis, K. A. (2001). The transformation of two-pyroxene-amphibole granulite to garnet granulite; simultaneous melting and fracturing of the lower crust, Fiordland, New Zealand. *Journal of Metamorphic Geology*, *9*(5), 547–560. https://doi.org/10.1046/j.0263-4929.2001.00328.x

Daczko, N., Klepeis, K. A., & Clarke, G. L. (2002a). Kyanite-paragonite-bearing assemblages, northern Fiordland, New Zealand: Rapid cooling of the lower crustal root to a Cretaceous magmatic arc. *Journal of Metamorphic Geology*, *20*, 887–902. https://doi.org/10.1046/j.1525-1314.2002.00421.x

Daczko, N., Klepeis, K. A., & Clarke, G. L. (2002b). Thermomechanical evolution of the crust during convergence and deep crustal pluton emplacement in the western province of Fiordland, New Zealand. *Tectonics*, *21*(4), 1–18. https://doi.org/10.1029/2001TC001282

Daczko, N. R., Klepeis, K. A., & Clarke, G. L. (2001). Evidence of early cretaceous collisional-style orogenesis in northern Fiordland, New Zealand and its effects on the evolution of the lower crust. *Journal of Structural Geology*, *23*(4), 693–713. https://doi.org/10.1016/S0191-8141(00)00130-9

Daczko, N. R., Milan, L. A., & Halpin, J. A. (2009). Metastable persistence of pelitic metamorphic assemblages at the root of a cretaceous magmatic arc—Fiordland, New Zealand. *Journal of Metamorphic Geology*, *27*(3), 233–247. https://doi.org/10.1111/j.1525-1314.2009.00815.x

Daczko, N. R., Stevenson, J. A., Clarke, G. L., & Klepeis, K. A. (2002c). Successive hydration and dehydration of high-P mafic granofels involving clinopyroxene-kyanite symplectites, Mt. Daniel, Fiordland, New Zealand. *Journal of Metamorphic Geology*, *20*, 669–682. https://doi.org/10.1046/j.1525-1314.2002.00397.x

DeCelles, P. G., Ducea, M. N., Kapp, P., & Zandt, G. (2009). Cyclicity in cordilleran orogenic systems. *Nature Geoscience*, *2*(4), 251–257. https://doi.org/10.1038/ngeo469

Decker, M., Schwartz, J. J., Stowell, H. H., Klepeis, K. A., Tulloch, A. J., Kitajima, K., et al. (2017). Slab-triggered arc flare-up in the cretaceous Median Batholith and the growth of lower arc crust, Fiordland, New Zealand. *Journal of Petrology*, *58*(6), 1145–1171. https://doi.org/10.1093/petrology/egx049

De Paoli, M. C., Clarke, C. L., Klepeis, K. A., Allibone, A. H., & Turnbull, I. M. (2009). The eclogite-granulite transition; mafic and intermediate assemblages at Breaksea sound, New Zealand. *Journal of Petrology*, *50*(12), 2307–2343. https://doi.org/10.1093/petrology/egp078

De Paoli, M. C., Clarke, G. L., & Daczko, N. R. (2012). Mineral equilibria modeling of the granulite-eclogite transition: Effects of whole-rock composition on metamorphic facies type-assemblages. *Journal of Petrology*, *53*, 949–970. https://doi.org/10.1093/petrology/egs004

Díaz-Azpiroz, M., Fernández, C., & Czeck, D. M. (2019). Are we studying deformed rocks in the right sections? Best practices in the kinematic analysis of 3D deformation zones. *Journal of Structural Geology*, *25*, 218–225. https://doi.org/10.1016/j.jsg.2018.03.005

Ducea, M. N. (2001). The California Arc: Thick granitic batholiths, eclogitic residues, lithospheric-scale thrusting, and magmatic flare-ups. *Geological Society of America Today*, *11*, 4–10. https://doi.org/10.1130/1052-5173(2001)011<0004:TCATGB>2.0.CO;2

Ferry, J. M., & Watson, E. B. (2007). New thermodynamic models and revised calibrations for the Ti-in-zircon and Zr-in-rutile thermometers. *Contributions to Mineralogy and Petrology*, *154*(4), 429–437. https://doi.org/10.1007/s00410-007-0201-0

Ford, H. A., Fischer, K. M., & Lekic, V. (2014). Localized shear in the deep lithosphere beneath the San Andreas fault system. *Geology*, *42*(4), 295–298. https://doi.org/10.1130/g35128.1

Fossen, H., & Cavalcante, G. C. G. (2017). Shear zones—A review. *Earth-Science Reviews*, *171*, 434–455. https://doi.org/10.1016/j.earscirev.2017.05.002

Gaina, C., Muller, D. R., Royer, J. Y., Stock, J., Hardebeck, J., & Symonds, P. (1998). The tectonic history of the Tasman sea: A puzzle with 13 pieces. *Journal of Geophysical Research*, *103*(B6), 12413–12433. https://doi.org/10.1029/98JB00386

Gale, J. F. W., Laubach, S. E., Olson, J. E., Eichhubl, P., & Fall, A. (2014). Natural fractures in shale: A review and new observations. *American Association of Petroleum Bulletin*, *98*(11), 2165–2216. https://doi.org/10.1306/08121413151

Gardner, R., Piazolo, S., Evans, L., & Daczko, N. (2017). Patterns of strain localization in heterogeneous, polycrystalline rocks—A numerical perspective. *Earth and Planetary Science Letters*, *463*, 253–265. https://doi.org/10.1016/j.epsl.2017.01.039

Gibson, G. M., & Ireland, T. R. (1995). Granulite formation during continental extension in Fiordland, New Zealand. *Nature*, *375*(6531), 479–482. https://doi.org/10.1038/375479a0

Gibson, G. M., McDougall, I., & Ireland, T. R. (1988). Age constraints on metamorphism and the development of a metamorphic core complex in Fiordland, southern New Zealand. *Geology*, *16*(5), 405–408. https://doi.org/10.1130/0091-7613(1988)016<0405:ACOMAT>2.3.CO;2

Giorgis, S., Tikoff, B., & McClelland, W. (2005). Missing Idaho arc: Transpressional modification of the $^{87}Sr/^{86}Sr$ transition on the western edge of the Idaho batholith. *Geology*, *33*(6), 469–472. https://doi.org/10.1130/G20911.1

Hacker, B. R., Kelemen, P. B., & Behn, M. D. (2015). Continental lower crust. *Annual Reviews of Earth and Planetary Science*, *43*(1), 6.1–6.39. https://doi.org/10.1146/annurev-earth-050212-124117

Haines, S., Lynch, E., Mulch, A., Valley, J. W., & Pluijm, B. V. D. (2016). Meteoric fluid infiltration in crustal-scale normal fault systems as indicated by $d^{18}O$ and $d^{2}H$ geochemistry and $^{40}Ar/^{39}Ar$ dating of neoformed clays in brittle fault rocks. *Lithosphere*, *8*(6), 587–600. https://doi.org/10.1130/L483.1

Hayden, L. A., Watson, E. B., & Wark, D. A. (2008). A thermobarometer for sphene (titanite). *Contributions to Mineralogy and Petrology*, *155*(4), 529–540. https://doi.org/10.1007/s00410-007-0256-y

Hollis, J. A., Clarke, G. L., Klepeis, K. A., Daczko, N. R., & Ireland, T. R. (2003). Geochronology and geochemistry of high-pressure granulites of the Arthur River complex, Fiordland, New Zealand: Cretaceous magmatism and metamorphism on the palaeo–Pacific margin. *Journal of Metamorphic Geology*, *21*(3), 299–313. https://doi.org/10.1046/j.15251314.2003.00443.x

Hollis, J. A., Clarke, G. L., Klepeis, K. A., Daczko, N. R., & Ireland, T. R. (2004). The regional significance of Cretaceous magmatism and metamorphism in Fiordland, New Zealand, from U-Pb zircon geochronology. *Journal of Metamorphic Geology*, *22*(7), 607–627. https://doi.org/10.1111/j.1525-1314.2004.00537.x

Houlié, N., & Stern, T. (2012). A comparison of GPS solutions for strain and SKS fast directions: Implications for modes of shear in the mantle of a plate boundary zone. *Earth and Planetary Science Letters*, *345–348*, 117–125. https://doi.org/10.1016/j.epsl.2012.06.029

Huber, C., Bachmann, O., & Dufek, J. (2011). Thermo-mechanical reactivation of locked crystal mushes: Melting-induced internal fracturing and assimilation processes in magmas. *Earth and Planetary Science Letters*, *304*(3–4), 443–454. https://doi.org/10.1016/j.epsl.2011.02.02

Huntington, K. W., & Klepeis, K. A. (2018). *Challenges and opportunities for research in tectonics: Understanding deformation and the processes that link Earth systems, from geologic time to human time*. A community vision document submitted to the U.S. National Science Foundation. University of Washington, 84 p. https://doi.org/10.6069/H52R3PQ5

Kimbrough, D. L., Tulloch, A. J., Coombs, D. S., Landis, C. A., Johnston, M. R., & Mattinson, J. M. (1994). Uranium lead zircon ages from the Median tectonic Zone, New Zealand. *New Zealand Journal of Geology and Geophysics*, *37*(4), 393–419. https://doi.org/10.1080/00288306.1994.9514630

King, D. S., Klepeis, K. A., Goldstein, A. G., Gehrels, G. E., & Clarke, G. L. (2008). The initiation and evolution of the transpressional Straight River shear zone, central Fiordland, New Zealand. *Journal of Structural Geology*, *30*(4), 410–430. https://doi.org/10.1016/j.jsg.2007.12.004

Klein, B. Z., & Jagoutz, O. (2021). Construction of a trans-crustal magma system: Building the bear valley intrusive suite, southern Sierra Nevada, California. *Earth and Planetary Science Letters*, *553*, 116624. https://doi.org/10.1016/j.epsl.2020.116624

Klepeis, K. A., Clarke, G. L., Gehrels, G., & Vervoort, J. (2004). Processes controlling vertical coupling and decoupling between the upper and lower crust of orogens: Results from Fiordland, New Zealand. *Journal of Structural Geology*, *26*(4), 765–791. https://doi.org/10.1016/j.jsg.2003.08.012

Klepeis, K. A., King, D., De Paoli, M., Clarke, G. L., & Gehrels, G. (2007). Interaction of strong lower and weak middle crust during lithospheric extension in Western New Zealand. *Tectonics*, *26*(4), TC4017. https://doi.org/10.1029/2006TC002003

Klepeis, K. A., & King, D. S. (2009). Evolution of the middle and lower crust during the transition from contraction to extension in Fiordland, New Zealand. In A. W. Snoke & R. B. Miller (Eds.), *Crustal cross sections from the western North American Cordillera and elsewhere: Implications for tectonic and petrologic processes* (Vol. 456, pp. 243–265). Geological Society of America Bulletin. https://doi.org/10.1130/2009.2456(09)

Klepeis, K. A., Schwartz, J., Stowell, H., & Tulloch, A. (2016). Gneiss domes, vertical and horizontal mass transfer, and the initiation of extension in the hot lower-crustal root of a continental arc, Fiordland, New Zealand. *Lithosphere*, *8*(2), 116–140. https://doi.org/10.1130/L490.1

Klepeis, K. A., Schwartz, J. J., Miranda, E., Lindquist, P., Jongens, R., Turnbull, R., & Stowell, H. (2022). Initiation and growth of transpressional shear zones through continental lithosphere, southwest New Zealand. Dryad, [Data set]. https://doi.org/10.5061/dryad.kh189326h

Klepeis, K. A., Webb, L., Blatchford, H., Schwartz, J. J., Jongens, R., Turnbull, R., & Stowell, H. H. (2019). Deep slab collision during miocene subduction causes uplift along crustal-scale reverse faults in Fiordland, New Zealand. *Geological Society of America Today*, *29*(9), 4–10. https://doi.org/10.1130/GSATG399A.1

Klepeis, K. A., Webb, L. E., Blatchford, H. J., Jongens, R., Turnbull, R. E., & Schwartz, J. J. (2019). The age and origin of Miocene-Pliocene fault reactivations in the upper plate of an incipient subduction zone, Puysegur Margin, New Zealand. *Tectonics*, *38*(8), 3237–3260. https://doi.org/10.1029/2019TC005674

Kruckenberg, S. C., Whitney, D. L., Teyssier, C., Fanning, C. M., & Dunlap, W. J. (2008). Paleocene-Eocene migmatite crystallization, extension, and exhumation in the hinterland of the northern Cordillera: Okanogan dome. *The Geological Society of America Bulletin*, *120*(7–8), 912–929. https://doi.org/10.1130/b26153.1

Kula, J. L., Tulloch, A. J., Spell, T. L., & Wells, M. L. (2007). Two-stage rifting of Zealandia-Australia-Antarctica: Evidence from $^{40}Ar/^{39}Ar$ thermochronometry of the Sisters shear zone, Stewart Island, New Zealand. *Geology*, *5*, 411–414. https://doi.org/10.1130/G23432A.1

Kylander-Clark, A. R. C., Hacker, B. R., & Cottle, J. M. (2013). Laser-ablation split-stream ICP petrochronology. *Chemical Geology*, *345*, 99–112. https://doi.org/10.1016/j.chemgeo.2013.02.019

Mantle, G. W., & Collins, W. J. (2008). Quantifying crustal thickness variations in evolving orogens: Correlation between arc basalt composition and Moho depth. *Geology*, *36*(1), 87–90. https://doi.org/10.1130/G24095A.1

Marcotte, S. B., Klepeis, K. A., Clarke, G. L., Gehrels, G., & Hollis, J. A. (2005). Intra-arc transpression in the lower crust and its relationship to magmatism in a Mesozoic magmatic arc. *Tectonophysics*, *407*(3–4), 135–163. https://doi.org/10.1016/j.tecto.2005.07.007

Mattinson, J. M. (2010). Analysis of the relative decay constants of 235U and 238U by multi-step CA-TIMS measurements of closed-system natural zircon samples. *Chemical Geology*, *275*(3–4), 186–198. https://doi.org/10.1016/j.chemgeo.2010.05.007

McCoy-West, J., Mortimer, N., & Ireland, T. R. (2014). U-Pb geochronology of Permian plutonic rocks, Longwood range, New Zealand: Implications for median batholith–Brook Street terrane relations. *New Zealand Journal of Geology and Geophysics*, *57*(1), 65–85. https://doi.org/10.1080/00288306.2013.869235

McDermott, R. G., Ault, A. K., & Caine, J. S. (2021). Dating fault damage along the eastern Denali fault zone with hematite (U-Th)/He thermochronometry. *Earth and Planetary Science Letters*, *563*, 116872. https://doi.org/10.1016/j.epsl.2021.116872

McGinn, C., Miranda, E. M., & Hufford, L. J. (2020). The effects of quartz Dauphiné twinning on strain localization in a mid-crustal shear zone. *Journal of Structural Geology*, *134*, 103980. https://doi.org/10.1016/j.jsg.2020.103980

Milan, L. A., Daczko, N. R., & Clarke, G. L. (2017). Cordillera Zealandia: A Mesozoic arc flare-up on the palaeo-Pacific Gondwana margin. *Scientific Reports*, *7*(1), 261. https://doi.org/10.1038/s41598-017-00347-w

Milan, L. A., Daczko, N. R., Clarke, G. L., & Allibone, A. H. (2016). Complexity of in-situ zircon U- Pb-Hf isotope systematics during arc magma genesis at the roots of a Cretaceous arc, Fiordland, New Zealand. *Lithos*, *264*, 296–314. https://doi.org/10.1016/j.lithos.2016.08.023

Miranda, E. A., & Klepeis, K. A. (2016). The interplay and effects of deformation and crystallized melt on the rheology of the lower continental crust, Fiordland, New Zealand. *Journal of Structural Geology*, *93*, 91–105. https://doi.org/10.1016/j.jsg.2016.09.007

Montési, L. G. J. (2013). Fabric development as the key for forming ductile shear zones and enabling plate tectonics. *Journal of Structural Geology*, *50*, 254–266. https://doi.org/10.1016/j.jsg.2012.12.011

Montési, L. G. J., & Hirth, G. (2003). Grain size evolution and the rheology of ductile shear zones: From laboratory experiments to postseismic creep. *Earth and Planetary Science Letters*, *211*(1–2), 97–110. https://doi.org/10.1016/S0012-821X(03)00196-1

Morozov, I. B., Smithson, S. B., Chen, J., & Hollister, L. S. (2001). Generation of new continental crust and terrane accretion in southeastern Alaska and western British Columbia: Constraints from P- and S- wave wide-angle data (ACCRETE). *Tectonophysics*, *341*(1–4), 49–67. https://doi.org/10.1016/S0040-1951(01)00190-1

Mortimer, N. (2004). New Zealand's geological foundations. *Gondwana Research*, *7*(1), 61–272. https://doi.org/10.1016/S1342-937X(05)70324-5

Mortimer, N., Campbell, H. J., Tulloch, A. J., King, P. K., Stagpoole, V. M., Wood, R. A., et al. (2017). Zealandia: Earth's hidden continent. *Geological Society of America Today*, *27*(3), 27–35. https://doi.org/10.1130/GSATG321A.1

Mortimer, N., Davey, F. J., Melhuish, A., Yu, J., & Godfrey, N. J. (2002). Geological interpretation of a deep seismic reflection profile across the eastern province and Median batholith, New Zealand: Crustal architecture of an extended Phanerozoic convergent orogeny. *New Zealand Journal of Geology and Geophysics*, *45*(3), 349–363. https://doi.org/10.1080/00288306.2002.9514978

Mortimer, N., Gans, P., Calvert, A., & Walker, N. W. (1999). Geology and thermochronometry of the East edge of the Median batholith (median tectonic zone): A new perspective on Permian to cretaceous crustal growth of New Zealand. *Island Arc*, *8*(3), 404–425. https://doi.org/10.1046/j.1440-1738.1999.00249.x

Mortimer, N., Tuoch, A. J., Spark, R. N., Walker, N. W., Ladley, E., Allibone, A., & Kimbrough, D. L. (1999). Overview of the Median batholith, New Zealand: A new interpretation of the geology of the Median tectonic zone and adjacent rocks. *Journal of African Earth Sciences*, *29*(1), 257–268. https://doi.org/10.1016/S0899-5362(99)00095-0

Moyer, G. A., Lee, J., Eddy, C., Miranda, E. A., Schwartz, J. J., Jongens, R., & Klepeis, K. (2018). Strain accommodation and 3D kinematics of transpressional flow within the lower crust of a Cretaceous magmatic arc in Fiordland, New Zealand. *Geological Society of America Abstracts with Programs*, *50*(6), 322805. https://doi.org/10.1130/abs/2018AM-322805

Muir, R. J., Ireland, T. R., Weaver, S. D., Bradshaw, J. D., Evans, J. A., Eby, G. N., & Shelley, D. (1998). Geochronology and geochemistry of a Mesozoic magmatic arc system, Fiordland, New Zealand. *Journal of the Geological Society London*, *155*(6), 1037–1053. https://doi.org/10.1144/gsjgs.155.6.1037

Negrini, M., Smith, S. A. F., Scott, J. M., & Tarling, M. S. (2018). Microstructural and rheological evolution of calcite mylonites during shear zone thinning: Constraints from the Mount Irene shear zone, Fiordland, New Zealand. *Journal of Structural Geology*, *106*, 86–102. https://doi.org/10.1016/j.jsg.2017.11.013

Norris, R. J., & Toy, V. G. (2014). Continental transforms: A view from the Alpine fault. *Journal of Structural Geology*, *4*, 3–31. https://doi.org/10.1016/j.jsg.2014.03.003

Oliver, G. J. H. (1990). An exposed cross-section of continental crust, Doubtful Sound, Fiordland, New Zealand: Geophysical and geological setting. In D. M. F. Fountain & M. H. Salisbury (Eds.), *Exposed cross-sections of the continental crust*, *NATO ASI ser., ser. C, 317* (pp. 43–69). Kluwer Academy.

Oliver, G. J. H., & Coggon, J. H. (1979). Crustal structure of Fiordland, New Zealand. *Tectonophysics*, *54*(3–4), 253–292. https://doi.org/10.1016/0040-1951(79)90371-8

Oncken, O., Asch, G., Haberland, C., Metchie, J., Sobolev, S., Stiller, M., et al. (2003). Seismic imaging of a convergent continental margin and plateau in the central Andes (Andean Continental Research Project 1996 (ANCORP'96)). *Journal of Geophysical Research*, *108*(B7). https://doi.org/10.1029/2002JB001771

Oriolo, S., Wemmer, K., Oyhantçabal, P., Fossen, H., Schulz, B., & Siegesmund, S. (2018). Geochronology of shear zones – A review. *Earth-Science Reviews*, *185*, 665–683. https://doi.org/10.1016/j.earscirev.2018.07.007

Orlandini, O. F., & Mahan, K. H. (2020). Rheological evolution of a pseudotachylyte-bearing deep crustal shear zone in the western Canadian shield. *Journal of Structural Geology*, *141*, 104188. https://doi.org/10.1016/j.jsg.2020.104188

Platt, J. P., & Behr, W. M. (2011). Lithospheric shear zones as constant stress experiments. *Geology*, *39*(2), 127–130. https://doi.org/10.1130/G31561.1

Rai, S. S., Priestley, K., Gaur, V. K., Mitra, S., Singh, M. P., & Searle, M. (2006). Configuration of the Indian Moho beneath the NW Himalaya and Ladakh. *Geophysical Research Letters*, *33*(15), L15308. https://doi.org/10.1029/2006GL026076

Ramezani, J., & Tulloch, A. J. (2009). TIMS U-Pb geochronology of southern and eastern Fiordland. In *Techfile report: QMP Fiordland/59, GNS Science*. Institute of Geological and Nuclear Sciences Ltd. https://doi.org/10.21420/G2CC7Z

Regan, S., Williams, M., Leslie, S., Mahan, K., Jercinovic, M., Holland, M., & Gibson, D. (2014). The Cora Lake shear zone, Athabasca granulite terrane, an intraplate response to far-field orogenic processes during the amalgamation of Laurentia. *Canadian Journal of Earth Sciences*, *51*(9), 877–901. https://doi.org/10.1139/cjes-2014-0015

Rey, P., Mondy, L., Duclaux, G., Teyssier, C., Whitney, D., Bocher, M., & Prigent, C. (2017). The origin of contractional structures in extensional gneiss domes. *Geology*, *45*(6), 263–266. https://doi.org/10.1130/g39229y.1

Ring, U., Bernet, M., & Tulloch, A. (2015). Kinematic, finite strain and vorticity analysis of the Sisters shear zone, Stewart Island, New Zealand. *Journal of Structural Geology*, *73*, 114–129. https://doi.org/10.1016/j.jsg.2015.02.004

Ringwood, M. F., Schwartz, J. J., Turnbull, R. E., & Tulloch, A. J. (2021). Phanerozoic record of mantle-dominated arc magmatic surges in the Zealandia Cordillera. *Geology*, *49*(10), 1230–1234. https://doi.org/10.1130/G48916.1

Rowe, C. D., & Griffith, W. A. (2015). Do faults preserve a record of seismic slip: A second opinion. *Journal of Structural Geology*, *78*, 1–26. https://doi.org/10.1016/j.jsg.2015.06.006

Saleeby, J. B., Ducea, M. N., Busby, C. J., Nadin, E. S., & Wetmore, P. H. (2008). Chronology of pluton emplacement and regional deformation in the southern Sierra Nevada batholith, California. *Geological Society of America Special Papers*, *438*, 397–427.

Sassier, C., Leloup, P. H., Rubatto, D., Galland, O., Yue, Y., & Lin, D. (2009). Direct measurement of strain rates in ductile shear zones: A new method based on syntectonic dikes. *Journal of Geophysical Research*, *114*(B1), B01406. https://doi.org/10.1029/2008jb005597

Savage, M. K., Duclos, M., & Marson-Pidgeon, K. (2007). Seismic anisotropy in South Island, New Zealand. In D. Okaya, T. Stern, & F. Davey (Eds.), *A continental plate boundary: Tectonics at South Island, New Zealand*, *Geophysical monograph series* (Vol. 75, pp. 95–114). American Geophysical Union. https://doi.org/10.1029/175gm06

Schulte, D. O., Ring, U., Thomson, S. N., Glodny, J., & Carrad, H. (2014). Two-stage development of the Paparoa metamorphic core complex, west coast, South Island, New Zealand: Hot continental extension precedes sea-floor spreading by ~25 m.y. *Lithosphere*, *6*(3), 177–194. https://doi.org/10.1130/L348.1

Schwartz, J. J., Andico, S., Turnbull, R., Klepeis, K. A., Tulloch, A., Kitajima, K., & Valley, J. W. (2021). Stable and transient isotopic trends in the crustal evolution of Zealandia Cordillera. *American Mineralogist*, *106*(9), 1369–1387. https://doi.org/10.2138/am-2021-7626

Schwartz, J. J., Klepeis, K. A., Sadorski, J. F., Stowell, H. H., Tulloch, A. J., & Coble, M. A. (2017). The tempo of continental arc construction in the Mesozoic Median Batholith, Fiordland, New Zealand. *Lithosphere*, *9*(3), 343–365. https://doi.org/10.1130/L610.1

Schwartz, J. J., Stowell, H. H., Klepeis, K. A., Zamora, C., Tulloch, A. J., Kylander-Clark, A. R. C., et al. (2016). Thermochronology of extensional orogenic collapse in the deep crust, Fiordland, New Zealand. *Geosphere*, *12*(3), 647–677. https://doi.org/10.1130/GES1232.1

Scott, J. M., Borcovsky, D. A., Palin, J. M., & Toy, V. G. (2014). Localisation of deformation in the thermal contrast at a granite batholith margin, New Zealand. *Journal of Structural Geology*, *64*, 149–163. https://doi.org/10.1016/j.jsg.2013.07.013

Scott, J. M., & Cooper, A. F. (2006). Early Cretaceous extensional exhumation of the lower crust of a magmatic arc: Evidence from the Mount Irene shear zone, Fiordland, New Zealand. *Tectonics*, *25*(3), TC3018. https://doi.org/10.1029/2005TC001890

Scott, J. M., Cooper, A. F., Palin, J. M., Tulloch, A. J., Kula, J., Jongens, R., et al. (2009). Tracking the influence of a continental margin on growth of a magmatic arc, Fiordland, New Zealand, using thermobarometry, thermochronology, and zircon U-Pb and Hf isotopes. *Tectonics*, *28*(6), TC6007. https://doi.org/10.1029/2009TC002489

Scott, J. M., Cooper, A. F., Tulloch, A. J., & Spell, T. L. (2011). Crustal thickening of the Early Cretaceous paleo-Pacific Gondwana margin. *Gondwana Research*, *20*(2–3), 380–394. https://doi.org/10.1016/j.gr.2010.10.008

Scott, J. M., & Palin, J. M. (2008). LA-ICP-MS U-Pb zircon ages from Mesozoic plutonic rocks in eastern Fiordland, New Zealand. *New Zealand Journal of Geology and Geophysics*, *51*(2), 105–113. https://doi.org/10.1080/00288300809509853

Spell, T. L., McDougall, I., & Tulloch, A. J. (2000). Thermochronologic constraints on the breakup of the Pacific Gondwana margin: The Paparoa metamorphic core complex, South Island, New Zealand. *Tectonics*, *19*(3), 433–451. https://doi.org/10.1029/1999TC900046

Spencer, C. J., Mitchell, R. N., & Brown, M. (2021). Enigmatic mid-Proterozoic orogens: Hot, thin, and low. *Geophysical Research Letters*, *48*(16), e2021GL093312. https://doi.org/10.1029/2021GL093312

Stacey, J. S., & Kramers, J. D. (1975). Approximation of terrestrial lead isotope evolution by a two stage model. *Earth and Planetary Science Letters*, *26*(2), 207–221. https://doi.org/10.1016/0012-821X(75)90088-6

Stowell, H., Odom Parker, K., Gatewood, M., Tulloch, A., & Koenig, A. (2014). Temporal links between pluton emplacement, garnet granulite metamorphism, partial melting and extensional collapse in the lower crust of a Cretaceous magmatic arc, Fiordland, New Zealand. *Journal of Metamorphic Geology*, *32*(2), 51–175. https://doi.org/10.1111/jmg.12064

Stowell, H., Schwartz, J., Bollen, E., Tulloch, A., Ramezani, J., & Klepeis, K. (2021). Timescales and rates of intrusive and metamorphic processes determined from zircon and garnet in migmatitic granulite, Fiordland, New Zealand. *American Mineralogist*, *107*(6), 1116–1132. https://doi.org/10.2138/am-2022-7967

Stowell, H. H., Schwartz, J. J., Klepeis, K. A., Hout, C., Tulloch, A. J., & Koenig, A. (2017). Sm-Nd garnet ages for granulite and eclogite in the Breaksea Orthogneiss and widespread granulite facies metamorphism of the lower crust, Fiordland magmatic arc, New Zealand. *Lithosphere*, *9*(6), 953–975. https://doi.org/10.1130/L662.1

Stowell, H. H., Tulloch, A., Zuluaga, C. A., & Koenig, A. (2010). Timing and duration of garnet granulite metamorphism in magmatic arc crust, Fiordland, New Zealand. *Chemical Geology*, *273*(1–2), 91–110. https://doi.org/10.1016/j.chemgeo.2010.02.015

Stuart, C. A., Piazolo, & S., & Daczko, N. R. (2016). Mass transfer in the lower crust: Evidence for incipient melt assisted flow along grain boundaries in the deep arc granulites of Fiordland, New Zealand. *Geochemistry, Geophysics, Geosystems*, *17*(9), 3733–3753. https://doi.org/10.1002/2015GC006236

Sutherland, R. (1999). Basement geology and tectonic development of the greater New Zealand region: An interpretation from regional magnetic data. *Tectonophysics*, *308*(3), 341–362. https://doi.org/10.1016/S0040-1951(99)00108-0

Tera, F., & Wasserburg, G. J. (1972). U-Th-Pb systematics in three Apollo 14 basalts and the problem of initial Pb in lunar rocks. *Earth and Planetary Science Letters*, *14*(3), 281–304. https://doi.org/10.1016/0012-821X(72)90128-8

Thatcher, W., & Pollitz, F. F. (2008). Temporal evolution of continental lithospheric strength in actively deforming regions. *Geological Society of America Today*, *18*, 4. https://doi.org/10.1130/gsat01804-5a.1

Tikoff, B., Blenkinsop, T., Kruckenberg, S. C., Morgan, S., Newman, J., & Wojtal, S. (2013). A perspective on the emergence of modern structural geology: Celebrating the feedbacks between historical-based and process-based approaches. In M. E. Bickford (Ed.), *The web of geological sciences: Advances, impacts, and interactions* (Vol. 500, pp. 65–119). Geological Society of America Special Paper. https://doi.org/10.1130/2013.2500(03

Titus, S. J., Medaris, L. G., Wang, H. F., & Tikoff, B. (2007). Continuation of the San Andreas fault system into the upper mantle: Evidence from spinel peridotite xenoliths in the Coyote Lake basalt, central California. *Tectonophysics*, *429*(1–2), 1–20. https://doi.org/10.1016/j.tecto.2006.07.004

Tulloch, A. J., Ireland, T. R., Kimbrough, D. L., Griffin, W. L., & Ramezani, J. (2011). Autochthonous inheritance of zircon through Cretaceous partial melting of Carboniferous plutons: The Arthur River Complex, Fiordland, New Zealand. *Contributions to Mineralogy and Petrology*, *161*(3), 401–421. https://doi.org/10.1007/s00410-010-0539-6

Tulloch, A. J., & Kimbrough, D. L. (1989). The Paparoa metamorphic core complex, New Zealand; Cretaceous extension associated with fragmentation of the Pacific margin of Gondwana. *Tectonics*, *8*(6), 1217–1235. https://doi.org/10.1029/TC008i006p01217

Tulloch, A. J., & Kimbrough, D. L. (2003). Paired plutonic belts in convergent margins and the development of high Sr/Y magmatism: Peninsular ranges batholith of Baja-California and median batholith of New Zealand. In S. E. Johnson, S. R. Paterson, J. M. Fletcher, G. H. Girty, D. L. Kimbrough, & A. Martín-Barajas (Eds.), *Tectonic evolution of northwestern México and the southwestern USA* (Vol. 374, pp. 275–295). Geological Society of America Special Paper.

Tulloch, A. J., Mortimer, N., Ireland, T. R., Waight, T. E., Maas, R., Palin, J. M., et al. (2019). Reconnaissance basement geology and tectonics of South Zealandia. *Tectonics*, *38*(2), 516–551. https://doi.org/10.1029/2018TC005116

Tulloch, A. J., Ramezani, J., Kimbrough, D. L., Faure, K., & Allibone, A. H. (2009). U-Pb geochronology of mid-Paleozoic plutonism in western New Zealand: Implications for S-type granite generation and growth of the east Gondwana margin. *The Geological Society of America Bulletin*, *121*(9/10), 1236–1261. https://doi.org/10.1130/B26272.1

Tulloch, A. J., Ramezani, J., Mortimer, N., Mortensen, J., van den Bogaard, P., & Maas, R. (2009). Cretaceous felsic volcanism in New Zealand and Lord Howe Rise (Zealandia) as a precursor to final Gondwana breakup. In U. Ring & B. Wernicke (Eds.), *Extending a continent: Architecture, rheology and heat budget* (Vol. 321, pp. 89–118). Geological Society of London Special Publication.

Turnbull, I. M., Allibone, A. H., & Jongens, R. (2010). Geology of the Fiordland area: Institute of Geological and Nuclear Sciences, Lower Hutt, scale 1:250 000, sheet 17, 97 p. text.

Turnbull, R., Weaver, S., Tulloch, A., Cole, J., Handler, M., & Ireland, T. (2010). Field and geochemical constraints on mafic-felsic interactions, and processes in high-level arc magma chambers: An example from the Halfmoon pluton, New Zealand. *Journal of Petrology*, *51*(7), 1477–1505. https://doi.org/10.1093/petrology/egq026

Turnbull, R. E., Schwartz, J. J., Fiorentini, M. L., Jongens, J., Evans, N. J., Ludwig, T., et al. (2021). A hidden Rodinian lithospheric keel beneath Zealandia, Earth's newly recognized continent. *Geology*, *49*(8), 1009–1014. https://doi.org/10.1130/G48711.1

van der Meer, Q. H. A., Waight, T. E., Tulloch, A. J., Whitehouse, M. J., & Andersen, T. (2018). Magmatic evolution during the Cretaceous transition from subduction to continental break-up of the Eastern Gondwana margin (New Zealand) documented by in-situ zircon O-Hf isotopes and bulk-rock Sr-Nd isotopes. *Journal of Petrology*, *59*(5), 849–880. https://doi.org/10.1093/petrology/egy047

Vermeesch, P. (2018). IsoplotR: A free and open toolbox for geochronology. *Geoscience Frontiers*, *9*(5), 1479–1493. https://doi.org/10.1016/j.gsf.2018.04.001

Webber, J. R., Klepeis, K. A., Webb, L. E., Cembrano, J., Morata, D., Mora-Klepeis, G., & Arancibia, G. (2015). Deformation and magma transport in a crystallizing plutonic complex, Coastal Batholith, central Chile. *Geosphere*, *11*(5), 1401–1426. https://doi.org/10.1130/GES01107.1

Williams, R. T., Goodwin, L. B., Sharp, W. D., & Mozley, P. S. (2017). Reading a 400, 000-year record of earthquake frequency for an intraplate fault. *Proceedings of the National Academy of Sciences of the United States of America*, *114*(19), 4893–4898. https://doi.org/10.1073/pnas.1617945114

Yoshinobu, A. S., Wolak, J. M., Paterson, S. R., Pignotta, G. S., & Anderson, H. S. (2009). Determining relative magma and host rock xenolith rheology during magmatic fabric formation in plutons: Examples from the middle and upper crust. *Geosphere*, *5*(3), 270–285. https://doi.org/10.1130/GES00191.1

References From the Supporting Information

Cherniak, D. J. (2006). Zr diffusion in titanite. *Contributions to Mineralogy and Petrology*, *152*(5), 639–647. https://doi.org/10.1007/s00410-006-0133-0

Spencer, K. J., Hacker, B. R., Kylander-Clark, A. R. C., Andersen, T. B., Cottle, J. M., Stearns, M. A., et al. (2013). Campaign-style titanite U-Pb dating by laser-ablation ICP: Implications for crustal flow, phase transformations and titanite closure. *Chemical Geology*, *341*, 84–101. https://doi.org/10.1016/j.chemgeo.2012.11.012

Stearns, M. A., Hacker, B. R., Ratschbacher, L., Rutte, D., & Kylander-Clark, A. R. C. (2015). Titanite petrochronology of the Pamir gneiss domes: Implications for mid-deep crust exhumation and titanite closure to Pb and Zr diffusion. *Tectonics*, *34*(4), 784–802. https://doi.org/10.1002/2014TC003774